



National Library  
of Canada

Bibliothèque nationale  
du Canada

Acquisitions and  
Bibliographic Services Branch

Direction des acquisitions et  
des services bibliographiques

395 Wellington Street  
Ottawa, Ontario  
K1A 0N4

395, rue Wellington  
Ottawa (Ontario)  
K1A 0N4

*Your file - Votre référence*

*Our file - Notre référence*

## NOTICE

**The quality of this microform is heavily dependent upon the quality of the original thesis submitted for microfilming. Every effort has been made to ensure the highest quality of reproduction possible.**

**If pages are missing, contact the university which granted the degree.**

**Some pages may have indistinct print especially if the original pages were typed with a poor typewriter ribbon or if the university sent us an inferior photocopy.**

**Reproduction in full or in part of this microform is governed by the Canadian Copyright Act, R.S.C. 1970, c. C-30, and subsequent amendments.**

## AVIS

**La qualité de cette microforme dépend grandement de la qualité de la thèse soumise au microfilmage. Nous avons tout fait pour assurer une qualité supérieure de reproduction.**

**S'il manque des pages, veuillez communiquer avec l'université qui a conféré le grade.**

**La qualité d'impression de certaines pages peut laisser à désirer, surtout si les pages originales ont été dactylographiées à l'aide d'un ruban usé ou si l'université nous a fait parvenir une photocopie de qualité inférieure.**

**La reproduction, même partielle, de cette microforme est soumise à la Loi canadienne sur le droit d'auteur, SRC 1970, c. C-30, et ses amendements subséquents.**

UNIVERSITY OF ALBERTA

A COMPACT, MULTICHANNEL, PHASE-LOCKED, CARBON DIOXIDE LASER  
SYSTEM

by

EUGENE FRANCIS YELDEN

A THESIS

SUBMITTED TO THE FACULTY OF GRADUATE STUDIES AND RESEARCH  
IN PARTIAL FULFILMENT OF THE REQUIREMENTS FOR THE DEGREE  
OF DOCTOR OF PHILOSOPHY

DEPARTMENT OF ELECTRICAL ENGINEERING

EDMONTON, ALBERTA

FALL, 1992



National Library  
of Canada

Bibliothèque nationale  
du Canada

Canadian Theses Service Service des thèses canadiennes

Ottawa, Canada  
K1A 0N4

The author has granted an irrevocable non-exclusive licence allowing the National Library of Canada to reproduce, loan, distribute or sell copies of his/her thesis by any means and in any form or format, making this thesis available to interested persons.

The author retains ownership of the copyright in his/her thesis. Neither the thesis nor substantial extracts from it may be printed or otherwise reproduced without his/her permission.

L'auteur a accordé une licence irrévocable et non exclusive permettant à la Bibliothèque nationale du Canada de reproduire, prêter, distribuer ou vendre des copies de sa thèse de quelque manière et sous quelque forme que ce soit pour mettre des exemplaires de cette thèse à la disposition des personnes intéressées.

L'auteur conserve la propriété du droit d'auteur qui protège sa thèse. Ni la thèse ni des extraits substantiels de celle-ci ne doivent être imprimés ou autrement reproduits sans son autorisation.

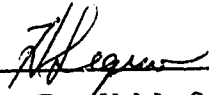
ISBN 0-315-77220-4

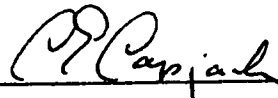
Canada

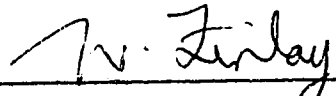


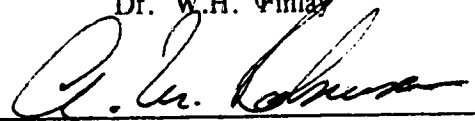
THE UNIVERSITY OF ALBERTA  
FACULTY OF GRADUATE STUDIES AND RESEARCH

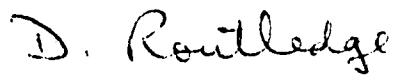
The undersigned certify that they have read, and recommend to the Faculty of Graduate Studies and Research, for acceptance, a thesis entitled A COMPACT, MULTICHANNEL, PHASE-LOCKED, CARBON DIOXIDE LASER SYSTEM submitted by EUGENE FRANCIS YELDEN in partial fulfilment of the requirements for the degree of DOCTOR OF PHILOSOPHY.


  
\_\_\_\_\_  
Dr. H.J.J. Seguin, Co-Supervisor

  
\_\_\_\_\_  
Dr. C.E. Capjack, Co-Supervisor

  
\_\_\_\_\_  
Dr. W.H. Finlay

  
\_\_\_\_\_  
Dr. A.M. Robinson

  
\_\_\_\_\_  
Dr. D. Routledge

  
\_\_\_\_\_  
Dr. A.J. Alcock, External Examiner

Date May 29/92

*Dedication*

*To my family and friends, for all of their love and encouragement.*

## Abstract

The carbon dioxide laser has become an increasingly important tool in research and industry. Consequently, it has been desirable to produce more powerful, yet compact and efficient laser systems. Recently, two methods have emerged as forerunners in the achievement of this goal. These methods are: an extended-area electrode scaling approach, as applied to RF-excited, diffusion-cooled laser devices; and coherent phase-locking of multiple gain channels in an extended laser array.

The purpose of this investigation was to examine the feasibility of incorporating the above two concepts into a single device. Initial experiments demonstrated that a stable  $\alpha$ -type gas discharge could indeed be simultaneously established within all the channels of a multichannel gain system. A subsequent analysis of the gain and saturation intensity parameters indicated that lasing operation was possible with this device.

An extensive series of optical extraction studies were performed employing several different resonator designs. These configurations included a conventional unstable resonator and a unique toric unstable resonator. Toric resonators were found to possess the advantages of a conventional resonator, plus the ability to extract the output beam from the centerline of the laser system. Furthermore, it was discovered that the size of the output coupling aperture in the toric systems had a profound influence on the output characteristics of the device. Parameters examined for each of the resonators included output power, near-field and far-field behaviour, alignment sensitivity and polarization properties.

The phase-locking characteristics of the system were also explored. Phase-locking levels as high as 91 % were measured for the conventional resonator when an injection seed beam was fed into the central region of the resonator. With no injected beam, self-phase-locking levels as high as 62 % were also determined between the individual channels. The mechanism for this locking was identified to be the independent lasing of the central inter-electrode region, plus the converging wave properties of the unstable resonators. These two attributes acted as the core oscillator region, which then supplied the surrounding gain channels with a common, fundamental optical mode.

Finally, laser cutting of mild steel was performed to document the usefulness of the device in a typical materials processing application. Cutting speeds comparable to currently available commercial systems were achieved, with the added benefit of the ability to cut at the same process speed, irrespective of the direction. This latter feature resulted from the unique polarization state of the output beam.



### Acknowledgement

The research outlined in this thesis would not have been possible without the help of many people. It is with pleasure that I am able to express my gratitude here.

I would especially like to thank my supervisors, Dr. C.E. Capjack and Dr. H.J.J. Seguin. I am very grateful for their guidance, confidence and encouragement over the last several years.

Many thanks also go to the members of the laser research group for their assistance. Dr. S.K. Nikumb is thanked for his many insightful suggestions regarding this investigation. Thanks go to Mr. H. Reshef for his expertise fabricating the numerous mirrors used for this study, as well as his assistance in performing some of the experiments. Mr. H. Dixel is thanked for the excellent talent that he supplied in the machine shop. Mr. D. Presakarchuk and Mr. C.V. Sellathamby are thanked for their help with the RF power supply and the image analysis studies, respectively. In addition, Mr. J. Strohschein, Mr. S. Scott and Mr. D. Akitt are thanked for their interest in this project and their countless discussions, which have been thoroughly enjoyable.

The author also gratefully acknowledges the financial support of the Province of Alberta, the Natural Sciences and Engineering Research Council of Canada and the University of Alberta.

Table of Contents

Chapter	Page
1. INTRODUCTION .....	1
1.1 Historical Development of the Carbon Dioxide Laser .....	2
1.2 Physical Principles of the Carbon Dioxide Laser Process .....	4
1.3 Gas Discharge Excitation Methods .....	7
1.3.1 RF Glow Discharges .....	8
1.3.2 General Description of an RF Excited Discharge .....	8
1.3.3 Alpha and Gamma RF Discharges .....	12
1.3.4 RF Discharge Variation with Pressure and Frequency .....	17
1.4 Large-Area Electrode Scaling Concepts .....	21
1.5 Multibeam and Phase-Locked Laser Devices .....	21
1.5.1 Multibeam Laser Systems .....	23
1.5.2 Phase-Locking and Beam Combining Techniques .....	25
1.6 Scope of this Research .....	28
2. SYSTEM DESIGN .....	29
2.1 Vacuum and Gas Inlet System .....	29
2.2 Electrode Design .....	30
2.3 Endplate Design .....	32
2.4 Outer Tube .....	34
2.5 RF Power Supply and Impedance Matching Network .....	34
3. GAIN AND SATURATION INTENSITY MEASUREMENTS .....	39
3.1 Theory and Experimental Technique .....	39
3.2 Gain Measurement Results .....	44
3.3 Saturation Intensity Measurements .....	53
4. OPTICAL EXTRACTION SYSTEMS .....	59
4.1 Optical Resonator Background .....	59
4.2 Resonator Design .....	62

4.3	Resonator Parameter Characterization Techniques .....	68
4.4	Resonator Output Characteristics .....	70
4.4.1	Toric Non-Confocal Resonator .....	71
4.4.2	Toric Confocal Resonator .....	90
4.4.3	Conventional Confocal Resonator .....	98
4.4.4	Conventional Non-Confocal Resonator .....	105
4.5	Resonator Performance Comparison .....	107
4.6	Central Inter-electrode Region Experiments .....	113
4.7	Optical Resonator Summary .....	115
5.	PHASE-LOCKING STUDIES .....	116
5.1	Introduction to Phase-Locking .....	116
5.2	Phase-Locking Experiments .....	119
5.2.1	Injection Phase-Locking .....	119
5.2.2	Self-Phase-Locking .....	123
5.2.3	Far-Field Experiments .....	128
5.3	Analysis of the Phase-Locking Results .....	128
6.	SHEET METAL CUTTING EXPERIMENTS .....	132
6.1	Introduction to Laser Materials Processing .....	132
6.2	Experimental Apparatus and Techniques .....	133
6.3	Cutting Performance and Discussion .....	135
7.	CONCLUSIONS AND PROPOSALS FOR FUTURE RESEARCH .....	139
7.1	Summary of this Investigation .....	139
7.2	Proposals for Future Research .....	141
	REFERENCES .....	144

<u>Table</u>	<u>Page</u>
4.1 Design Specifications for the Optical Resonator Systems .....	66
4.2 Focal Spot Size Variation with Resonator Type .....	108
4.3 Summary of Various Resonator Properties .....	110

<u>Figure</u>	<u>Page</u>
1.1 CO <sub>2</sub> Laser Gas Flow Geometries .....	3
1.2 Energy Level Diagram of the CO <sub>2</sub> :N <sub>2</sub> :He Laser .....	5
1.3 Typical Luminosity from an RF Glow Discharge .....	9
1.4 Parameter Distribution of an RF Glow Discharge .....	10
1.5 Ionization in an RF Glow Discharge .....	13
1.6 $\alpha$ and $\gamma$ Forms of RF Discharges. Parts (a) and (c) correspond to an $\alpha$ -type discharge, whereas (b) and (d) are for a $\gamma$ -type .....	14
1.7 Typical V-I Characteristic Curve of an RF Discharge .....	16
1.8 Variation of the Sheath Width With Frequency .....	19
1.9 Two Possible Large-Area Electrode Discharge Geometries .....	22
1.10 Two Possible Multibeam Laser System Configurations .....	24
2.1 Photograph of the Electrode and Endplate Detail .....	31
2.2 Schematic Diagram of the System Design .....	33
2.3 Cutaway View of the Complete Discharge Apparatus .....	35
2.4 Photograph of the Assembled Discharge Structure .....	36
3.1 Block Diagram of the Gain and Saturation Intensity Measurement Apparatus .....	43
3.2 Variation of the Gain Coefficient with the Total Gas Pressure .....	46
3.3 Variation of the Gain Coefficient with the RF Input Power .....	47
3.4 Variation of the Gain Coefficient with the CO <sub>2</sub> Partial Pressure .....	48
3.5 Variation of the Gain Coefficient with Nitrogen Partial Pressure .....	49
3.6 Variation of the Gain Coefficient with Helium Partial Pressure .....	51
3.7 Variation of the Gain in the Central Inter-electrode Region as a Function of Pressure .....	52
3.8 Saturation Intensity for a 12.5 Torr Gas Pressure .....	54
3.9 Saturation Intensity for a 17.5 Torr Gas Pressure .....	55
3.10 Variation of the Saturation Intensity with the Total Gas Pressure .....	56

Figure	Page
3.11 Gain Coefficient - Saturation Intensity Product Variation with Pressure .....	57
4.1 Resonator Stability Diagram .....	61
4.2 Conventional Unstable Resonator Schematic .....	63
4.3 Toric Unstable Resonator Schematic .....	67
4.4 Near-field Beam Pattern for a Toric Non-Confocal Resonator with $M = 1.16$ and a 3.18 cm Aperture .....	72
4.5 Near-field Beam Pattern for a Toric Non-Confocal Resonator with $M = 1.16$ and a 1.27 cm Aperture .....	73
4.6 3-D Near-field Intensity Profile for a Toric Non-Confocal Resonator with $M = 1.16$ and a 3.18 cm Aperture .....	74
4.7 3-D Near-field Intensity Profile for a Toric Non-Confocal Resonator with $M = 1.16$ and a 1.27 cm Aperture .....	75
4.8 2-D Near-field Intensity Profile for a Toric Non-Confocal Resonator with $M = 1.16$ and a 3.18 cm Aperture .....	76
4.9 2-D Near-field Intensity Profile for a Toric Non-Confocal Resonator with $M = 1.16$ and a 1.27 cm Aperture .....	77
4.10 Typical Far-field Burn Pattern in Perspex for a Toric Non-Confocal Resonator with $M = 1.16$ and a 3.18 cm Aperture .....	79
4.11 Variation of $1/e^2$ Focal Spot Size with Aperture Size for a Toric Non-Confocal Resonator with $M = 1.16$ .....	80
4.12 Variation of Output Power with Aperture Size for a Toric Non-Confocal Resonator with $M = 1.12$ .....	82
4.13 Variation of Output Power with Aperture Size for a Toric Non-Confocal Resonator with $M = 1.16$ .....	83
4.14 Variation of Output Power with Aperture Size for a Toric Non-Confocal Resonator with $M = 1.20$ .....	84
4.15 Variation of Output Power with Magnification for a Toric Non-Confocal Resonator .....	87
4.16 Schematic Representation of the Output Beam Polarization for the Toric Non-Confocal Resonator with a 3.18 cm Aperture .....	89
4.17 Near-field Beam Pattern for a Toric Confocal Resonator with $M = 1.16$ and a 1.78 cm Aperture .....	91
4.18 3-D Near-field Intensity Profile for a Toric Confocal Resonator with $M = 1.16$ and a 1.78 cm Aperture .....	92

Figure	Page
4.19 2-D Near-field Intensity Profile for a Toric Confocal Resonator with $M = 1.16$ and a 1.78 cm Aperture .....	93
4.20 Variation of the $1/e^2$ Focal Spot Size with the Aperture Size for a Toric Confocal Resonator with $M = 1.16$ .....	95
4.21 Variation of Output Power with Aperture Size for a Toric Confocal Resonator with $M = 1.16$ .....	96
4.22 Schematic Representation of the Output Beam Polarization State for a Toric Confocal Resonator with a 2.16 cm Aperture .....	97
4.23 Near-field Beam Pattern for a Conventional Confocal Resonator with $M = 1.16$ and an 8.64 cm Output Mirror Diameter .....	99
4.24 3-D Near-field Intensity Profile for a Conventional Confocal Resonator with $M = 1.16$ and an 8.64 cm Output Mirror Diameter .....	100
4.25 2-D Near-field Intensity Profile for a Conventional Confocal Resonator with $M = 1.16$ and an 8.64 cm Output Mirror Diameter .....	101
4.26 Typical Far-field Burn Pattern in Perspex for a Conventional Confocal Resonator with $M = 1.16$ and an 8.64 cm Output Mirror Diameter .....	102
4.27 Variation of the $1/e^2$ Focal Spot Size with the Output Mirror Diameter for a Conventional Confocal Resonator with $M = 1.16$ .....	103
4.28 Variation of the Output Power with the Output Mirror Diameter for a Conventional Confocal Resonator with $M = 1.16$ .....	104
4.29 Variation of the Output Power with the Output Mirror Diameter for a Conventional Non-Confocal Resonator with $M = 1.16$ .....	106
5.1 Block Diagram of the Experimental Arrangement Used for the Phase-Locking Measurements .....	120
5.2 Intensity Profile of a Single Beam .....	122
5.3 Photograph of a Typical Interference Fringe Pattern .....	124
5.4 Typical Intensity Profile of the Observed Interference Fringes With an Externally Injected Beam .....	125
5.5 Typical Intensity Profile of the Observed Interference Fringes Without an Externally Injected Beam .....	126
5.6 Typical Intensity Profile for Two Overlapping Output Beams With the Central Interelectrode Region Blocked .....	127
6.1 Block Diagram of the Laser Cutting Apparatus .....	134

Figure	Page
6.2 Variation in the Maximum Cutting Speed for Different Thicknesses of Mild Steel .....	137



## List of Symbols

<u>Symbol</u>	<u>Definition</u>
$a_i$	physical radius of resonator mirror
A	area of the electrode face; area of the probe laser beam; element of the ABCD matrix
AC	alternating current
c	speed of light
C	capacitance
CC	conventional confocal resonator
CNC	conventional non-confocal resonator
d	diameter of discharge tube; electrode gap separation; optical path length difference
D	element of the ABCD matrix
DC	direct current
e	electron; electronic charge
E	electric field amplitude
E/N	reduced electric field
f	frequency
FWHM	full width at half maximum
$f$	pulse repetition frequency
$f/\#$	speed of focusing lens
$g_i$	characteristic resonator parameter
I	intensity of the laser beam
$I_{\text{sat}}$	saturation intensity
k	rate coefficient for reaction
$k_B$	Boltzmann's constant

K.E.	kinetic energy
L	discharge length; optical resonator mirror separation
m	mass of the CO <sub>2</sub> molecule; half trace of the ABCD matrix
m <sub>e</sub>	electron mass
M	resonator magnification
M <sub>i</sub>	resonator mirror
MOPA	master oscillator-power amplifier
N	number of elements in a laser array; total gas number density
P	laser output power; total gas pressure
R	discharge resistance
R <sub>i</sub>	resonator mirror radius of curvature
RF	radio frequency
S	optical resonator sensitivity to misalignment
T	gas temperature
TC	toric confocal resonator
TEM	transverse electric and magnetic
TNC	toric non-confocal resonator
v	thermal molecular speed
V	Visibility function; gas flow velocity; voltage across the discharge; gas volume
x	electron oscillation amplitude; discharge sheath thickness
z	axial length coordinate
α	Townsend's first ionization coefficient; gain coefficient
α <sub>0</sub>	small signal gain coefficient
γ	Townsend's second ionization coefficient
δ	ideal geometrical output coupling fraction
δ*	calculated output coupling fraction
ΔP	change in gas pressure

$\Delta t$	time interval
$\Delta \nu_D$	Doppler broadened linewidth
$\Delta \nu_H$	homogeneously broadened linewidth
$\epsilon_0$	permittivity of free space
$\lambda$	mean free path length; transition wavelength of optical output
$\nu$	electron collision frequency
$\nu_i$	frequency of electromagnetic wave
$\rho$	mass density of the laser gas
$\tau$	pulse width
$\phi$	optical phase difference
$\psi_i$	fractional content of component $i$ of the gas mixture
$\omega$	angular frequency of the applied electric field

## CHAPTER 1

### INTRODUCTION

Since its introduction by Patel over 25 years ago<sup>1,2</sup>, the carbon dioxide laser has become a very important research and industrial tool. Low power CO<sub>2</sub> lasers have proven to be successful in micromachining, microsoldering, and in many specialized surgical applications.<sup>3,4</sup> Lasers in the 250 W to 1 kW range are used for marking, scribing, cloth cutting and thin metal processes.<sup>5</sup> Those with powers around 1-5 kW are commonly used for isotope separation<sup>6</sup>, cutting, welding, cladding, and heat treating of various metals.<sup>7-9</sup> Finally, very high power lasers, with output powers ranging from 20 to 45 kW, or more<sup>10,11</sup>, have been developed for cutting and welding of thick metal components.

As the number of CO<sub>2</sub> laser applications has grown, so has the need for more compact, efficient, reliable and powerful devices.<sup>12-15</sup> In order to achieve an increased output power, and still maintain a compact device package, several investigations have focused on radio-frequency-excited laser arrays and large-area electrode systems.<sup>16-18</sup> The judicious adaptation of some of these concepts has led to more practical, compact and reliable laser systems. These devices avoid some of the inherent pitfalls of the previous generations, such as complicated gas transport, electrical excitation and optical designs.

This study focuses on the development of a compact carbon dioxide laser system. This structure combines both the extended-area electrode scaling concept and the multichannel phase-locked array approach into a single device.

This chapter will briefly deal with the historical development of the CO<sub>2</sub> laser. This is followed by a section on the physical principles of CO<sub>2</sub> laser operation. Various gas discharge excitation methods, focussing primarily on radio frequency techniques are presented next. The approaches to large-area electrode scaling and multibeam phase-locked arrays are then outlined. Finally, the motivation, the general ambit of, and the aims of this thesis are presented.

### 1.1 Historical Development of the Carbon Dioxide Laser

The first CO<sub>2</sub> lasers were simple axial discharge tubes as shown in Figure 1.1(a). These devices were totally sealed tubes, or had a very slow axial gas flow.<sup>19</sup> In these units, the waste heat, (approximately 80 % of the input energy), was removed by simple diffusion to the outer walls. An increase of 50 % in the output power was reported by Moeller and Rigden<sup>20</sup> through the introduction of forced air cooling on the outer walls of the discharge tube. Patel *et al.*<sup>21</sup>, and Bridges and Patel<sup>22</sup>, extended the cooling concept to the use of flowing water, and even to the lowering of the outer tube wall temperature to 213 K. The latter action produced a 200-300 % increase in the output power, which was measured to be 4.5 watts.

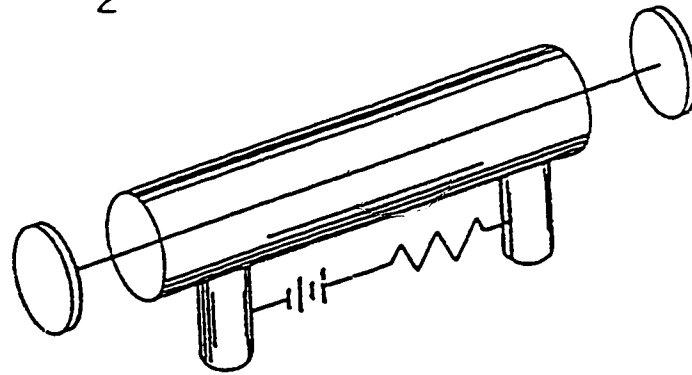
More recently, DeMaria<sup>19</sup> has shown that the maximum attainable output power per unit volume from a diffusion-cooled laser is proportional to:

$$P \propto \frac{\rho \lambda v}{d^2} \quad (1.1)$$

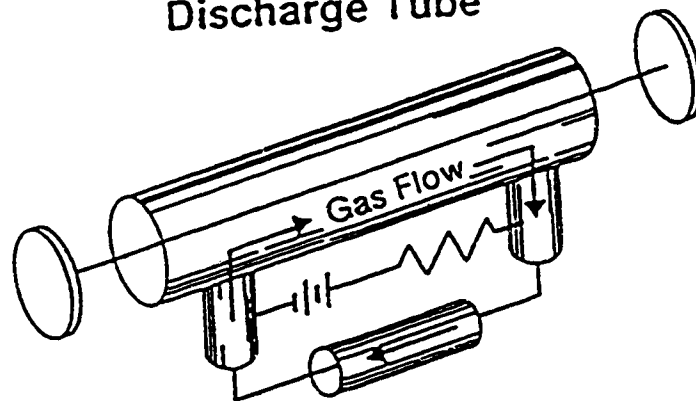
where  $\rho$  is the gas density,  $v$  is the thermal molecular speed,  $\lambda$  is the mean free path of the CO<sub>2</sub> molecules in the gas mixture, and  $d$  is the discharge tube diameter. Since the mean free path is inversely proportional to the gas density, and therefore inversely proportional to the pressure, the effect of increasing pressure is counterbalanced by a decrease in the mean free path; hence no improvement is obtained. Similarly, increasing the tube diameter is of no advantage since the power per unit volume decreases at the same rate at which the volume is increasing. Therefore, the output power per unit length of a diffusion-cooled laser is virtually a constant, at about 70-80 W/m.<sup>23</sup> Because of this fact, some researchers have scaled the discharge tube lengths up to 67 meters and thereby have achieved output powers of a few kilowatts.<sup>24</sup>

The next major improvement in the CO<sub>2</sub> laser was the advent of high speed convective gas cooling.<sup>25</sup> In these systems, provision is made to flow gas axially down the discharge tube, as shown in Figure 1.1(b). In this manner, hot gas is completely removed from the discharge region and consequently the output power becomes a direct function of the gas flow velocity. Tiffany *et al.*<sup>26</sup> have shown that the output power density under these conditions is given by:

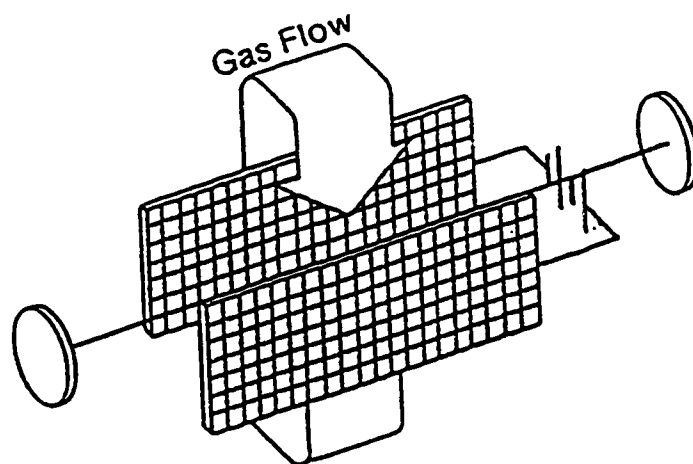
## CO<sub>2</sub> Laser Gas Flow Systems



Discharge Tube



Axial Flow



Transverse Flow

Figure 1.1 CO<sub>2</sub> Laser Gas Flow Geometries

$$P \propto \frac{\rho V}{L} \quad (1.2)$$

where  $L$  is the discharge length in the direction of gas flow,  $V$  is the gas flow velocity, and  $\rho$  is the mass density. In order to transport the gas at a sufficiently high velocity through the typically narrow discharge tube, high static pressure Roots-type blowers are required. This type of blower is a costly and complicated addition to the system. In spite of this limitation, systems of a few kilowatts have been produced.<sup>27</sup>

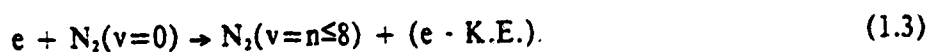
A further innovation was made with the introduction of the transverse-flow-gas-transport concept by Tiffany *et al.*<sup>26</sup> This system, depicted in Figure 1.1(c), features the direction of gas flow, the excitation field, and the optic axis all mutually perpendicular to each other. In this arrangement, the required flow velocity is greatly reduced. As such, the transverse-flow-geometry is now commonly used for the construction of CO<sub>2</sub> lasers with output power levels above about 5 kW.<sup>28</sup>

## 1.2 Physical Principles of the Carbon Dioxide Laser Process

This section will briefly discuss the vibrational energy structure of the CO<sub>2</sub> molecule, methods of exciting the upper CO<sub>2</sub> laser level and then collisional relaxation processes of the lower laser level.

The energy level diagram for a CO<sub>2</sub> laser is shown in Figure 1.2.<sup>29</sup> As can be seen, the CO<sub>2</sub> laser is a 4-level laser system with lasing possible at both 10.6  $\mu\text{m}$  and 9.4  $\mu\text{m}$ . The 10.6  $\mu\text{m}$  laser transition is between the asymmetric stretch (00<sup>0</sup>1) and the symmetric stretch (10<sup>0</sup>0) vibrational levels, while the 9.4  $\mu\text{m}$  transition is from the asymmetric stretch (00<sup>0</sup>1) to the bending (02<sup>0</sup>0) vibrational level. The lower laser levels are depopulated by collisional relaxation to the ground state (00<sup>0</sup>0), through the (01<sup>1</sup>0) bending vibrational level.

Excitation of the upper laser level (00<sup>0</sup>1) is achieved by one of two processes.<sup>29</sup> First, there is resonant energy transfer from the excited nitrogen molecules, which is represented by:



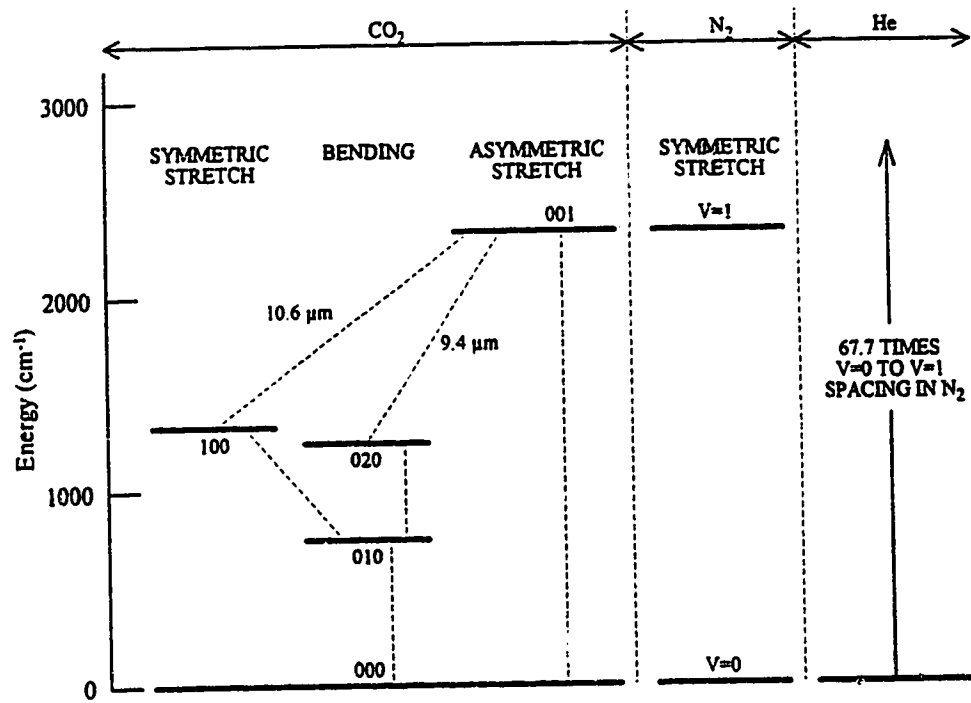
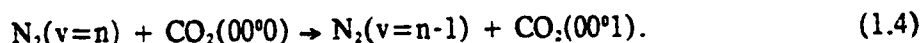


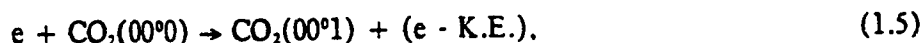
Figure 1.2 Energy Level Diagram of the  $\text{CO}_2$ : $\text{N}_2$ :He Laser



followed by:

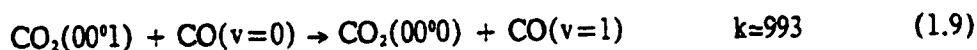
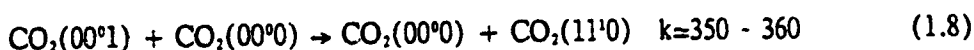
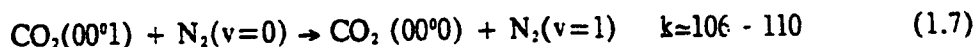


The second method stems from direct-electron impact of the  $\text{CO}_2$  molecules in the ground state:



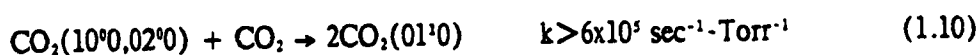
where K.E. is the kinetic energy in equations (1.3) and (1.5).

Collisional relaxation phenomena for the upper laser level, which compete directly with stimulated emission, are given by Witteman<sup>3</sup> and Cherrington.<sup>30</sup> These mechanisms and their associated rate coefficients, at a temperature of 300 K are:

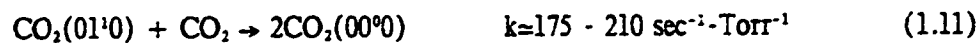


In a typical  $\text{CO}_2$  laser gas mixture, nitrogen and helium account for about 80% of the gas mix. Since nitrogen and helium have relatively low rate coefficients<sup>30</sup>, there is poor relaxation of the upper laser level. Carbon dioxide and carbon monoxide have higher rate coefficients<sup>30</sup> however, the coefficients are mixture-weighted and these two gases usually account for only about 20% of a typical laser gas mixture.

The collisional relaxation of the lower laser level is a two-part process. The first step is a very fast vibrational relaxation from the  $(10^0)$  or  $(02^0)$  state to the  $(01^0)$  state:



The second step is a somewhat slower process from the (01<sup>1</sup>0) level to the ground state, (00<sup>0</sup>0). These processes are given by:



The final process, which is expressed by equation (1.13), is the fastest of the three, and is one of the primary reasons for the addition of helium to a CO<sub>2</sub> laser gas mixture. The other reason is the fact that helium helps in cooling the discharge gas since it has a thermal conductivity about six times that of CO<sub>2</sub> and N<sub>2</sub>.<sup>3</sup> This helps to increase the heat transfer between the discharge and the outer walls of the system.

Collisional relaxation processes are strong functions of the gas temperature. This is because the (01<sup>1</sup>0) vibrational level is very close to the ground state and hence, increased temperature will induce more molecules to make the transition from the (00<sup>0</sup>0) level to the (01<sup>1</sup>0) level. This in turn reduces the depopulation rate of the lower laser level. In addition, the collisional relaxation rate of the upper laser level (00<sup>0</sup>1) increases with increasing temperature and consequently, the population of the upper laser level decreases.<sup>3</sup> The first effect is known as "thermal bottlenecking", and results in a reduced population inversion and concomitant drop in the output power of the laser.

### 1.3 Gas Discharge Excitation Methods

There are two basic methods of exciting a gas laser: direct current (DC) discharges and alternating current (AC) discharges. The AC discharge method may be further subdivided into: (i) AC, with frequencies between about 5,000 - 100,000 Hz, (ii) radio frequency (RF) discharges with  $f \approx 1 \text{ MHz} - 500 \text{ MHz}$ ; and microwave excited discharges with  $f \approx 1 \text{ GHz}$  and

higher. Furthermore, there have been several laser systems constructed with a combination of two or more excitation methods. For instance: ultraviolet preionization with DC excitation<sup>31-35</sup> and RF preionization with DC excitation.<sup>36-39</sup> Only the RF-excited discharges will be discussed herein.

### 1.3.1 RF Glow Discharges

The use of radio frequency fields to excite laser discharges has been known since the advent of the gas discharge laser.<sup>1,2</sup> However, initial reliability concerns and less than adequate coupling configurations impeded rapid development.<sup>39</sup> More recently, however, this particular excitation technique has witnessed considerable renewed interest, and has been the focus of numerous experimental<sup>40-56</sup> and theoretical investigations.<sup>57-65</sup> This has been especially true with respect to narrow-gap and waveguide lasers. Several researchers have realized the advantages of RF over DC excited discharges, some of which are:<sup>39,44,45</sup> lower voltages required to strike and maintain a discharge, a positive discharge impedance which eliminates the need for ballast resistors, a uniform discharge which can extend over large parallel electrodes, and the possibility of non-metallic electrodes which increases the device operational lifetime. A general description of an RF discharge follows in the next section.

### 1.3.2 General Description of an RF Excited Discharge

A typical RF discharge, and its associated parameter distribution, are shown in Figures 1.3 and 1.4, respectively.<sup>66</sup> Essentially, the fundamental discharge phenomena are identical for both RF and DC systems, with any differences being caused by the temporal interaction of the oscillation frequency, collision frequency, etc.

The specific sequence of processes that occur in an RF discharge are as follows. When the electric field is first applied any electrons that are present in the gas from external sources, such as cosmic radiation, are accelerated. As the polarity of the applied field changes, the force on the electrons also changes, and thereby causes oscillatory motion. The electrons undergo several collisions with other particles per oscillation cycle, and hence, transfer energy

Due to copyright restrictions this figure could not be reproduced herein. The figure is a photograph of the luminous intensity typically found in an RF-excited discharge. The original figure may be found in: D. He, C.J. Baker and D.R. Hall, "*Discharge striations in rf excited waveguide lasers*", J. Appl. Phys., 55, 4120, (1984).

Due to copyright restrictions this figure could not be reproduced herein. The figure shows the typical distribution of the space-charge, electric field and charged particle concentration within an RF-excited discharge. The original figure may be found in: D. He, C.J. Baker and D.R. Hall, "*Discharge striations in rf excited waveguide lasers*", J. Appl. Phys., 55, 4120, (1984).

from the RF electric field to the gas. With many collisions per cycle, some electrons acquire sufficient energy to ionize molecules upon collision. This aspect is the basis of volume ionization. Of course, the familiar electron loss processes, such as attachment, detachment and recombination, are still in effect. Consequently, it is the balance between these processes that determines the specific discharge properties.

Following the analysis by Hall and Hill<sup>67</sup>, it is reasonable to consider only the electron motion in an RF field. This is because the mass of the ions is much greater than that of the electrons. The amplitude of the electron oscillation is therefore given by:<sup>67</sup>

$$x = \frac{eE}{m_e \nu \omega} \quad (1.14)$$

where  $e$ ,  $E$ ,  $m_e$ ,  $\nu$  and  $\omega$  are the electronic charge, electric field amplitude, electron mass, electron collision frequency and angular frequency of the applied field, respectively. In a region far removed from any boundaries, the electrons oscillate according to equation (1.14), and the ions are essentially stationary. In this region, charge neutrality exists and there is therefore no space-charge concentration, and hence no internal electric fields.

If, however, a boundary is present, such as an electrode wall, the parameters are changed. In the region near the electrode, at least within one electron oscillation amplitude, there is a high probability of electron loss to the electrode.<sup>67</sup> This results in the creation of a thin region of positive charge that is close and parallel to the electrode surface. The polarity of this resulting internal DC field is such that it attracts electrons away from the electrode. However, the ions are accelerated toward it, with the possibility of the secondary emission of an electron. This secondary emission can have a serious, adverse effect on the discharge, as will be discussed shortly.

The above discussion essentially describes the appearance of the discharge as shown in Figures 1.3 and 1.4. As expected, the discharge is symmetrical about the plane through the center of the volume and parallel to the electrodes. Adjacent to each electrode is a thin dark region, followed by a peak in the luminous intensity which corresponds to the point at which the excited species decay in the gas. The space between these two bright peaks is the positive

column which exhibits a somewhat lower luminous intensity. The reduction in intensity is consistent with the fact that the electrons are less energetic the farther they move away from the positive ion space-charge zone.

As mentioned at the beginning of this section, most of the differences, and consequently the advantages, of RF excitation are due to the fast periodic variation of the applied voltage. As determined by Hugel<sup>68</sup>, the electron distribution function, electron energy, and hence the rate constants, are determined by the instantaneous value of the electric field strength. Thus, the situation for the ionization mechanism in an RF discharge is shown in Figure 1.5.<sup>68</sup> Due to the strong dependence of the ionization coefficient,  $k_i$ , on the reduced electric field strength,  $E/N$  (electric field intensity/total neutral particle concentration), ionization takes place only during short time intervals around the maxima of the field strength. Such a plasma is recombination-dominated<sup>43</sup> and has a nearly constant electron density. As was shown by Wiegand<sup>69</sup>, a recombination-dominated discharge is the most stable form of gas discharge possible. This is further enhanced by the fact that the maintenance of a self-sustained RF discharge requires a considerably smaller value of electric field strength than does a DC discharge. A lower electric field strength means that the dissociative attachment process is less prevalent, and hence, the discharge becomes even more recombination-dominated.

### 1.3.3 Alpha and Gamma RF Discharges

There are two distinctly different types of stable RF discharges that may occur, as first observed by Levitskii.<sup>70</sup> The two different types have been referred to as the alpha ( $\alpha$ ) and the gamma ( $\gamma$ ) type discharge after Townsend's first and second ionization coefficients, respectively. The  $\alpha$ -discharge is a low current discharge that is dominated by volume ionization as the electron production mechanism. By contrast, the  $\gamma$ -discharge is a high current discharge where the electron production is mainly confined to the plasma/electrode boundary region. Figure 1.6<sup>71</sup> shows both types of discharge and the associated luminosity of each. Both photographs are on the same scale and parts (a) and (c) are of the  $\alpha$ -discharge.

Due to copyright restrictions this figure could not be reproduced herein. The figure shows the ionization process within an RF-excited glow discharge. The original figure may be found in: H.E. Hugel, "*RF excitation of high power CO<sub>2</sub> lasers*", High Power Lasers and Their Industrial Applications (1986), D. Schuocker, editor, Proc. SPIE 650, 2, (1986).



Due to copyright restrictions this figure could not be reproduced herein. The figure shows the typical luminous intensity for the  $\alpha$ - and  $\gamma$ -types of RF-excited discharge. The original figure may be found in: P. Vidaud, S.M.A. Durrani and D.R. Hall, "*Alpha and gamma RF capacitative discharges in  $N_2$  at intermediate pressures*", J. Phys. D: Appl. Phys., 21, 57, (1988).

Figure 1.6  $\alpha$  and  $\gamma$  Forms of RF Discharges. Parts (a) and (c) correspond to an  $\alpha$ -type discharge, whereas (b) and (d) are for a  $\gamma$ -type

whereas parts (b) and (d) are of the  $\gamma$ -discharge.

Clearly, there is a large difference in the physical appearance of the two types of discharge. When an RF field is applied to the center of the electrode, breakdown occurs, and a low current  $\alpha$ -discharge results. An increase in the RF power will cause the discharge to spread along the electrodes and occupy the entire available volume. A further power increase will result in an increased current and a corresponding increase in the luminous intensity, as has been documented by He *et al.*<sup>66</sup> Finally, however, a critical power level is reached and the discharge suddenly collapses toward the center of the electrodes forming a  $\gamma$ -discharge.

A typical voltage-current characteristic curve is shown in Figure 1.7.<sup>67</sup> Region "AB" corresponds to the  $\alpha$ -discharge slowly filling the electrode face to occupy the available volume. Region "BC" indicates the range in which the discharge is useful for laser excitation. Note especially the positive resistance of the discharge, and therefore, no need for external ballast resistors. Point "C" indicates the transition from an  $\alpha$ - to a  $\gamma$ -discharge.

Durrani<sup>45</sup> has conducted an extensive study of the  $\alpha$ - to  $\gamma$ -transition in both pure molecular gases and carbon dioxide laser gas mixtures. It was found that the lower power density  $\alpha$ -discharge is characterized by relatively lower conducting and positively charged sheaths near each electrode boundary, and has a relatively low current density that is sustained by volume ionization. On the other hand, the  $\gamma$ -discharge has a high current density, relatively high displacement and conducting currents, thin electrode boundary sheaths and is sustained by wall ionization. It has been postulated that the transition from an  $\alpha$ - to a  $\gamma$ -discharge may be a result of neutralization of the  $\alpha$ -discharge positive ion sheaths by electrons produced by secondary emission from the electrodes, which increases with increasing power. This increased emission leads to a natural increase in the conductivity of the sheath, and is a form of positive feedback which rapidly leads to the collapse of the discharge into the  $\gamma$ -regime. Durrani<sup>45</sup> found that for a typical 1:1:3 = CO<sub>2</sub>:N<sub>2</sub>:He laser gas mixture, at a constant pressure, the power density required to establish the  $\gamma$ -discharge rose from 3.49 W/cm<sup>2</sup> at 15.5 MHz to 6.8 W/cm<sup>2</sup> at 25.5 MHz. It was further determined that the RF transition voltage and power density both increase with either increasing electrode gap

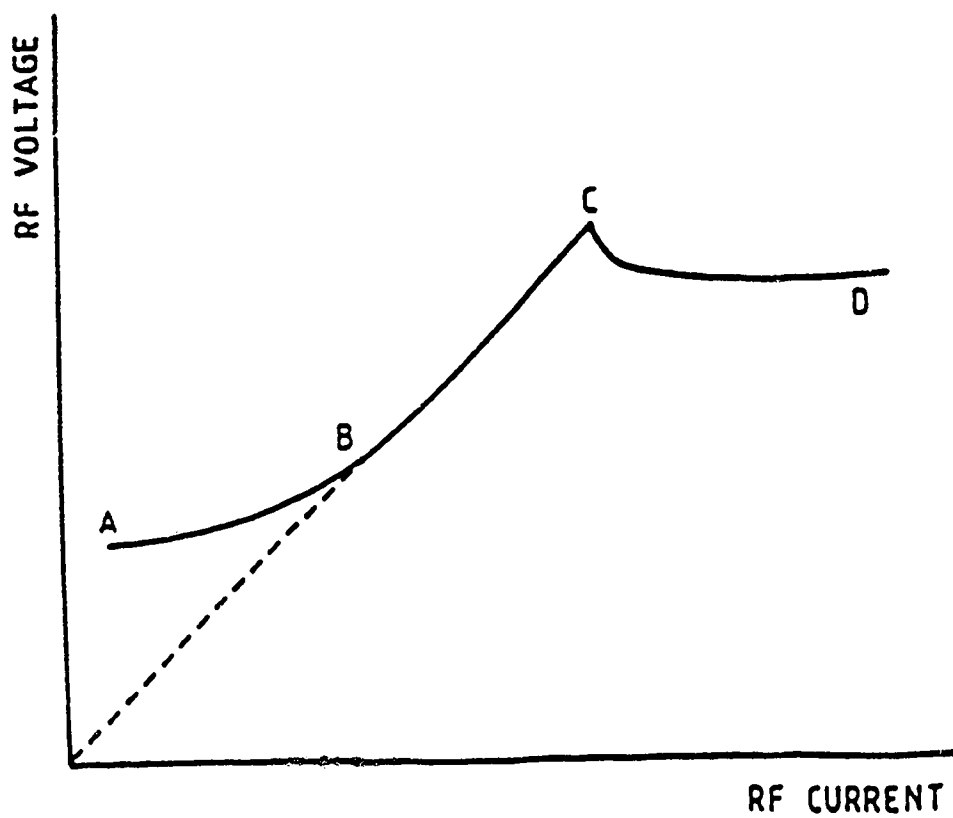


Figure 1.7 Typical V-I Characteristic Curve of an RF Discharge

separation or increasing gas pressure. Traditionally, only the  $\alpha$ -type of discharge is used for laser excitation due to the constricted nature of the  $\gamma$ -type of discharge.

#### 1.3.4 RF Discharge Variation with Pressure and Frequency

As briefly alluded to in the previous section, the variation of the frequency of the excitation field may have a pronounced influence on the gas discharge parameters. For this reason, some of the more salient features of this variation will be presented. Several researchers have conducted extensive experimental investigations of the effects of pressure and frequency variations on discharge properties.<sup>39,45,72</sup> These studies have included the effects of pressure and frequency on: discharge power loading, laser output power and efficiency, discharge resistance and the striation or sheath regions.

The effect of pressure and frequency variations on the discharge power loading is quite dramatic. In general, it was found that operation at higher frequencies and pressures allowed for higher power loading, which should translate into higher laser output power. The higher frequency resulted in a reduced sheath capacitance which in turn results in higher currents and charge densities. Higher gas pressures could be maintained as a result of a narrow electrode gap, which in turn leads to a reduced gas temperature due to the nature of the diffusion-cooling process.

Laser output power and device efficiency were found to follow similar trends. The maximum laser output power at a constant power loading is found to occur at lower values of excitation frequency and gas pressure as the electrode separation distance increases. Furthermore, it was found that the optimum excitation frequency falls off significantly at larger electrode separations. For larger gaps, the output laser power was determined to be a very strong function of the gas pressure at low values of frequency, but is influenced to a lesser extent at higher frequency ranges. Slight shifts in the frequency away from the optimum value are found to drastically reduce the available output power. For example, a  $\pm 10\%$  frequency shift resulted in a  $\pm 20\%$  power reduction.<sup>45</sup> In contrast, for narrow gap electrode structures, output power fluctuations are more pronounced at higher values of the

excitation frequency.<sup>72</sup>

In general, it is found that the advantages of operating at a larger electrode separation, where the optimum pressure and frequency are lower, will be offset by the rising neutral gas temperature due to the increased gap size, and the increasing tendency for the  $\alpha$ - to  $\gamma$ -discharge transition to occur. Therefore, a narrower gap structure, with a correspondingly higher frequency excitation, appears to be a more promising strategy. However, gap sizes smaller than  $\approx 1$  mm cause additional problems due to increased optical losses from coupling the optical energy into the interelectrode region, as well as difficulties in maintaining a spatially uniform discharge at a sufficiently high frequency.<sup>53</sup>

The variation of discharge sheath regions has also been studied.<sup>45,72</sup> These regions are important since they reflect a strong variation in electron energy and density within the discharge. This variation may have a detrimental affect on the production of a uniform gain distribution and on good transverse mode control. These regions have also been termed "striations", and only the discharge volume between them is useful for power extraction.

Equation (1.14) gives the approximate sheath thickness:

$$x = \frac{eE}{m_e \nu \omega} \quad (1.14)$$

which is the same as the amplitude of the electron oscillation. As is clear, the thickness of the sheaths varies inversely with frequency, and the results of He and Hall<sup>72</sup> confirm this. As is shown in Figure 1.8, an increase in the excitation frequency results in the sheaths moving closer to the electrode walls. A similar, but less pronounced, effect is observed when the gas pressure is increased.<sup>45</sup> This is due to the pressure dependence of the electron collision frequency,  $\nu$ . Returning to Figure 1.8, a further noteworthy feature is that the total area under the 133 MHz curve is  $\approx 12$  % lower than that under the 84 MHz curve. The reason for this phenomenon is that visible emission originates from high energy electrons, and hence, the 133 MHz discharge is "cooler" and more efficient in terms of vibrational excitation.

From the above discussion, it could naively be assumed that the higher the excitation frequency, the better the laser performance. However, this is not the situation, with the

Due to copyright restrictions this figure could not be reproduced herein. The figure shows the variation of the sheath thickness with the excitation frequency. The original figure may be found in: D. He and D.R. Hall, "*Frequency dependence in RF discharge excited waveguide CO<sub>2</sub> lasers*", IEEE J. Quantum Electron., QE-20, 509, (1984).

reason following from the fact that the discharge resistance decreases with increasing frequency.<sup>72</sup> If too high a frequency is selected, the reduced resistance results in a reduced voltage across the discharge,  $V \propto \sqrt{R}$ , and a stable discharge can only be maintained at a lower pressure. This lower pressure results in a reduced molecular density, and subsequently, an increased  $E/N$  which is now no longer at its optimum value.

There is also a lower bound on the excitation frequency which is determined by the electrode separation distance,  $d$ .<sup>44</sup> For any useful laser discharge region to be formed,

$$d - 2x > 0 \quad (1.15)$$

where  $x$  is the sheath thickness or electron oscillation amplitude as determined previously. If the oscillation amplitude is too large, or similarly, if the frequency is too low, any electrons generated by gaseous ionization will be swept out of the discharge and collected by the electrodes on one half of the RF cycle. Without question, this is not a desirable situation for efficient laser excitation.

Finally, it has been shown that by writing an expression for the electron energy distribution for a sinusoidally varying electric field, the AC electric field may be written as an effective DC field by the relation:<sup>67</sup>

$$E^2(\text{AC}) = E^2(\text{DC})[1 + \omega^2/\nu^2] \quad (1.16)$$

where  $\nu$  is the electron collision frequency and  $\omega$  is the angular frequency of the applied electric field. For cases in which  $\nu \gg \omega$ , equation (1.16) reduces to the DC case and therefore, the excitation rates and other transport properties derived for a steady-state field may be used with the RF field.

To summarize, it has become apparent that there is an optimum excitation frequency and gas pressure for the efficient extraction of laser power from an RF driven system. This optimum value will depend strongly on the particular device geometry and other factors such as the electrode gap separation and gas cooling capabilities.

#### 1.4 Large-Area Electrode Scaling Concepts

Traditionally, the output power of diffusion-cooled lasers has been limited, primarily by gas heating effects, to approximately 75 W/m.<sup>19</sup> Consequently, increasing the cavity length was the only approach to achieve higher output power levels. However, recent advances with the large-area or slab discharge techniques take advantage of the fact that transverse RF discharges, cooled by diffusion to metallic electrodes, may exhibit a useful power loading dependence that scales with the discharge area, not length.

The concept of the large-area electrode discharge, in which the conventional square bore waveguide geometry is abandoned in favour of large aspect ratio (electrode height/electrode separation) discharge volumes, was first proposed and demonstrated by Crocker and Wills<sup>36</sup> in an annular discharge structure. Similarly, a device with a rectangular geometry was first operated by Gabai *et al.*<sup>73</sup> Two possible configurations for the large-area electrode geometry are shown in Figure 1.9.

Since the introduction of this scaling concept, several investigations have been undertaken to characterize these structures.<sup>17,18,44,53,74,81</sup> These experiments have achieved a very high level of specific power extraction per unit area of the discharge. Values of between 14 to 20 kW/m<sup>2</sup> of output power are now common<sup>53,76,77</sup>, and specifically, an output power of 240 W was obtained from a 38 cm long device.<sup>77</sup> In addition, reports of output powers at the kilowatt level from  $\approx$  60 cm of discharge length have appeared.<sup>53,81</sup> Clearly, this type of electrode geometry would seem to provide an appropriate avenue from which to pursue a compact, and yet high power laser design.

#### 1.5 Multibeam and Phase-Locked Laser Devices

The previous section described efforts to increase the output power of laser devices through the concept of large-area electrode scaling. However, there is also another method that looks promising for boosting laser output powers. Concurrently, much effort has been expended in the investigation of multibeam, phase-locked laser arrays. This is particularly true for CO<sub>2</sub>, waveguide and diode laser arrays. The multichannel concept is also proving valuable



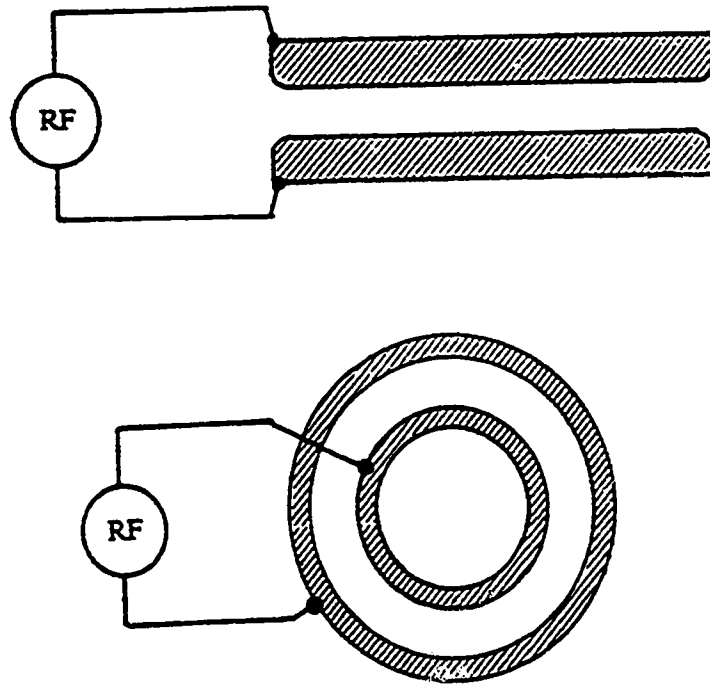


Figure 1.9 Two Possible Large-Area Electrode Discharge Geometries

in the construction of gravitational wave antennas<sup>82</sup> and multiple mirror telescope phased arrays.<sup>83</sup>

This section will discuss the multibeam array concept. Following this introduction, a description of various methods by which multibeam systems may be optically phase-locked will be presented.

### 1.5.1 Multibeam Laser Systems

The multibeam concept, in which two or more laser tubes or channels are operated in parallel and share a common optical resonator, was first proposed by Crancon and Lavarini<sup>84</sup> in the early 1970's. The first experimental investigations were reported by Kozlov *et al.*<sup>85</sup>, which described a system with a variable number of channels, from 7 to 39, and a maximum output power level of  $\approx 3$  kW. Since this first demonstration, multichannel devices have been examined extensively.<sup>40,86-94</sup> Several innovative designs have been evaluated, including systems with over 100 separate channels<sup>92</sup>, and output powers in the 10 kW range.<sup>91</sup>

Figure 1.10 depicts two possible configurations for a multibeam laser system. As mentioned previously, the structure consists of several separate discharge channels which are operated in parallel and share a common optical resonator. The advantages that may be realized from such multichannel systems are twofold. First, since the output power of a normal diffusion-cooled laser scales only as the discharge length, and not the discharge diameter, several small diameter tubes can be fitted in place of one larger tube. It is also known that the gain experienced by the optical radiation is inversely proportional to the tube diameter.<sup>95</sup> Therefore, the effect of replacing one large discharge tube by multiple smaller ones is to increase the laser output power in direct proportion to  $N$ , the number of tubes in the array.<sup>96</sup> This property in itself is a great benefit to laser design, especially to laser materials processing applications that require high power levels but not necessarily high beam intensities, such as the cutting of thin materials or surface treating.<sup>69</sup>

The second advantage to multibeam systems is realized when all of the individual lasers in the array operate in a coherent phase-locked manner. When this situation is

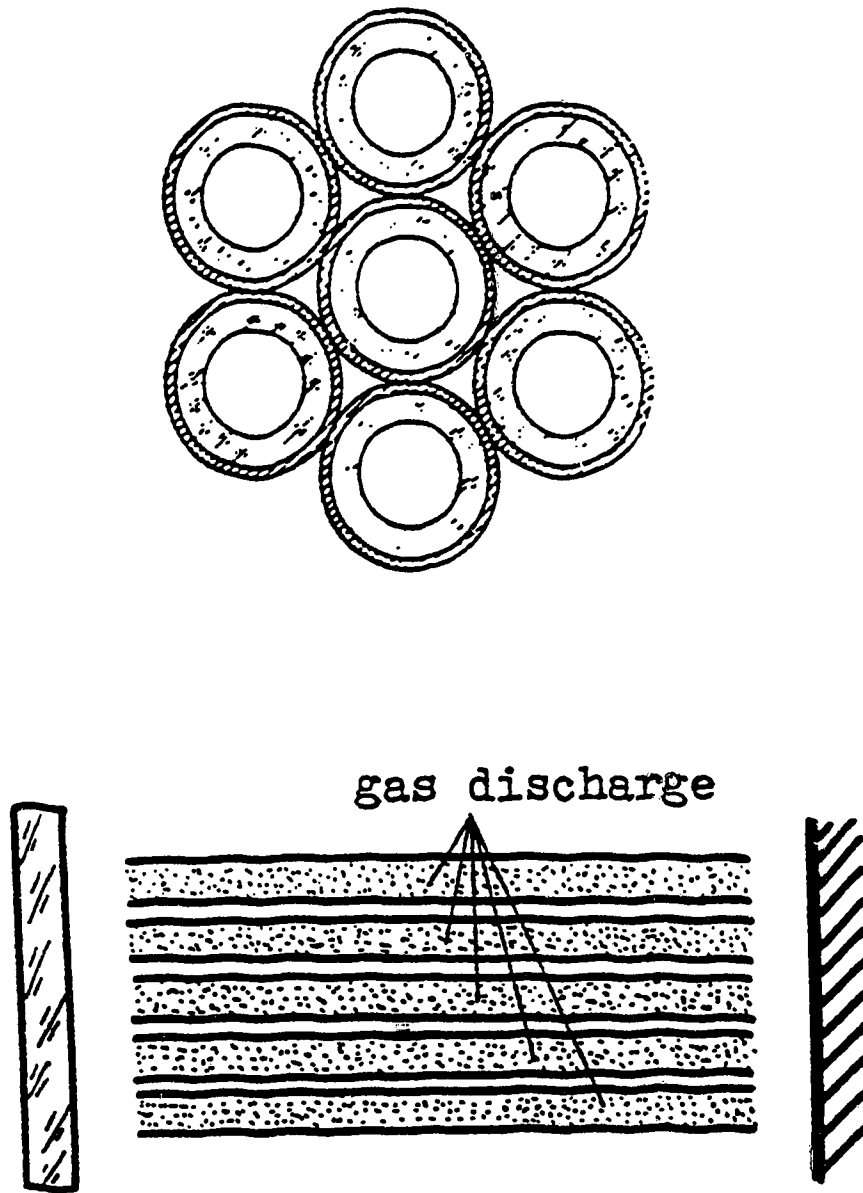


Figure 1.10 Two Possible Multibeam Laser System Configurations

achieved, the maximum intensity of the radiation at the focal spot increases in proportion to  $N^2$ .<sup>96</sup> This now allows these devices to be particularly useful in materials processing applications such as deep-penetration welding and cutting that require very high output power densities.<sup>8,9</sup> The various methods and approaches to beam combining and phase-locking will be addressed in the following section.

### 1.5.2 Phase-Locking and Beam Combining Techniques

The frequency or phase-locking of two or more oscillators has occurred in a variety of disciplines, including electrical engineering, physics and the biological sciences.<sup>97</sup> Perhaps the earliest known recorded observation of frequency locking was made by Christiaan Huygens, when he wrote in 1665:<sup>97</sup>

Being obliged to stay in my room for several days and also occupied in making observations on my two newly made clocks, I have noticed a remarkable effect which no one could have ever thought of. It is that these two clocks hanging next to one another separated by one or two feet keep an agreement so exact that the pendulums invariably oscillate together without variation. After admiring this for a while, I finally figured out that it occurs through a kind of sympathy: mixing up the swings of the pendulums, I have found that within a half hour they always return to consonance and remain so constantly afterwards as long as I let them go. I then separated them, hanging one at the end of the room and the other fifteen feet away, and noticed that in a day there was five seconds difference between them. Consequently, their earlier agreement must in my opinion have been caused by an imperceptible agitation of the air produced by the motion of the pendulums. The clocks are always shut in their boxes, each weighing a total of less than 100 pounds. When in consonance, the pendulums do not oscillate parallel to one another, but instead they approach and separate in opposite directions.

Huygens later found that the actual coupling mechanism was a small vibration transmitted through the wall, and not the movement of air that he had suspected.

The application of phase-locking to lasers was first proposed by Basov *et al.*<sup>98</sup>, and subsequently re-examined by several other investigators<sup>99-101</sup>, including the classic treatment by Spencer and Lamb.<sup>102</sup> Phase-locking was first achieved experimentally by Stover and Steier<sup>103</sup> by injecting the beam from one HeNe laser directly into another similar device.

Since this first demonstration, numerous techniques have been devised to phase-lock multiple laser devices together. All of these methods may be collected into three broad categories<sup>104-105</sup>, which will be briefly outlined below.

One method of achieving frequency or phase-locking of a laser array is that of adaptive optics.<sup>106-109</sup> With this approach, the output from each channel in the array is sampled, and then compared to a reference signal. This comparison then generates a control signal, which will drive a piezoelectric transducer mounted on the back of each cavity mirror, such that it will correct for any frequency discrepancies. Despite the complexities of incorporating adaptive optical systems in some laser arrays, this method does produce satisfactory results.

The second technique that may be implemented to establish phase-locking is based on the method of injecting a standard reference laser signal into all of the lasers in the array. This process encompasses both the injection-locked and the master oscillator plus power amplifier (MOPA) approaches. These two procedures are very similar, but they do have subtle differences.<sup>105</sup> The injection-locking concept utilizes a common, low power source, which is introduced into a narrow region of the rest of the array. This injected signal is used to provide a common influence for each of the other devices to be seeded from. An important feature of this scheme is the fact that each of the individual lasers in the array would lase independently if the injecting source was not present. The MOPA technique is similar, except that the injected beam from the master oscillator now has a power level comparable to that of each of the individual gain regions, and the reference beam is usually introduced over the full aperture of the region, rather than a small portion of it. Furthermore, the separate gain regions of a MOPA that form the power amplifier section will not usually lase independently of the master oscillator.

As with the other phase-locking concepts, numerous investigations have been undertaken with injection-locked and MOPA devices.<sup>110-125</sup> Most of these results have been quite encouraging, demonstrating near 100% phase-locking for both single- and multi-spectral line laser devices.<sup>114,115</sup> In addition, it was shown that by a judicious selection of the laser cavity parameters and injecting scheme, an output-to-injected power ratio of close to 10<sup>4</sup> could be achieved.<sup>119</sup> However, the one drawback to this technique may be the very stringent alignment tolerances of the optical resonator, which may approach  $\lambda/30$  or more.<sup>112</sup>

The third and final technique to attain phase-locking is based on the introduction of some form of optical coupling between the lasers in the array. In this manner, some mechanism for optical communication must exist amongst the multiple laser resonators. There are four principal methods by which this communication may take place.

Phase-locking may be achieved by intercavity spatial filtering of the optical radiation, or by the Talbot effect, which is a slight variation of the spatial filtering process.<sup>126-134</sup> Nonlinear optical coupling methods, such as phase conjugation, are also suitable procedures.<sup>135-144</sup> The third concept involves the use of what has become known as "leaky waveguides", in which a portion of the dividing structure between adjacent lasers in the array is removed to allow the coupling to occur.<sup>40,94,145-148</sup> The final coupling technique is that of mode matched coupling, in which a portion of the center of the resonator mode is shared by two or more resonators.<sup>149-160</sup> A slight variation on this is termed adjoint or converging wave coupling, where a portion of the output from one device is fed back into another device and vice versa.<sup>161-164</sup> This method is very useful in that it allows for the graceful degradation of the system. Should one of the lasers fail to operate, there will still be output from the rest of the system. Unfortunately, coupled resonator optical systems can easily become very complicated as the number of individual devices increases.<sup>105</sup> Of course, nothing precludes combining any of the above described approaches to achieve the desired phase-locking result.

An interesting parameter that is associated with the optical coupling methods is that of locking range. The locking range is the amount by which the cavity lengths of the coupled resonators can vary and still have substantial phase-locking occur. Typical locking ranges are about  $\lambda/10$ .<sup>105</sup> In general, it is found that as the amount of coupling between the cavities is increased, the locking range is also broadened, as well as the percentage of phase-locking.<sup>149</sup> At coupling values beyond about 50 %, the separate cavities begin to act as one "super-cavity", and most of the individuality of the lasers in the array is lost.<sup>155</sup>

### 1.6 Scope of this Research

The motivation for this investigation is to explore the feasibility of integrating the large-area electrode scaling concept with the multibeam, phase-locking techniques. To pursue this, a gas discharge structure has been constructed that contains eight, large aspect ratio electrodes (approximately 8:1) arranged in a radial array. Preliminary discharge experiments, including small signal gain and saturation intensity measurements, indicated that this geometry is well suited for use as a laser device. Subsequently, several optical resonators were implemented on the system, including an unusual toric resonator design in which the output beams are extracted from the centerline of the electrode structure. Various parameters were characterized with each optical system, including: the output power, focal spot size, near-field intensity profile, polarization and alignment sensitivity measurements. This was followed by a study of the phase-locking ability of the separate channels. It was determined that by the judicious choice of an optical resonator, all eight of the system channels could be partially phase-locked via optical coupling in the central region of the discharge structure. Finally, as a demonstration of the system's performance ability, laser cutting of sheet metal was carried out.

## CHAPTER 2

### SYSTEM DESIGN

Initial experiments for this study were conducted by using both a single pair, and a complete set of eight, large-area electrodes that were placed in a perspex vacuum chamber. A one kilowatt RF power supply, operating at a fixed frequency of 27.5 MHz, was used to excite the discharge. A series of discharge experiments, featuring power loading levels, small signal gain and saturation intensity measurements, indicated that this multi-gain channel discharge structure was a viable concept.<sup>165</sup> It was also determined that the 1 kW power supply was incapable of adequately driving the complete set of eight discharge channels at pressures much above 30 Torr. In particular, either the discharge would not occupy the whole length of the channel, or it would extinguish altogether. Consequently, a larger RF power supply was required to provide sufficient excitation to the entire electrode assembly.

This chapter describes the design of the multichannel discharge structure. There are essentially seven components to the overall system: the vacuum pump and the inlet gas system, the electrodes, the endplates, the outer tube, the RF power supply, the impedance matching network, and the optical system. Since the various optical systems investigated comprise a major portion of this thesis, they will be described in a separate chapter. The remainder of the device components are addressed individually below.

#### 2.1 Vacuum and Gas Inlet System

The vacuum and gas handling systems were kept as simple as possible. An array of gas flow meters was used to admit the CO<sub>2</sub>/N<sub>2</sub>/He gas mixture. Separate gas lines for each constituent were chosen to provide flexibility in the working gas mixture and pressure during the experiments.

The vacuum chamber was evacuated, prior to gas backfilling, with an Edwards Model E2M40 vacuum pump, which had a nominal pumping speed of 44000 litres/hr. Typical pumpdown time from atmospheric pressure to  $\approx$  50 mTorr was approximately 5 minutes. The



lowest pressure attained, after sustained pumping (to allow the various materials to outgas) was 8 mTorr.

It is well known that gas contamination due to vacuum leaks can greatly affect the discharge parameters.<sup>166-171</sup> This is especially true in the case of molecular oxygen. For this reason, good vacuum integrity is a requirement. The leak rate of the vacuum system was determined by first evacuating the system, sealing it off, and then observing the pressure rise with time. The leak rate is given by the expression:

$$\text{leak rate} = V \frac{\Delta P}{\Delta t} \quad (2.1)$$

where V is the system gas volume (75.5 ℓ) and ΔP and Δt are the changes in pressure and time, respectively. Starting from a base pressure of 8 mTorr, the system pressure was observed to rise to 218 mTorr in 8 hours. This corresponds to a leak rate of 2 ℓ-Torr/hr. Therefore, over a typical experimental running time of one hour, the pressure rise due to gas leaks is ≈ 26 mTorr, which proved to be insignificant compared to the normal operating pressure of ≈ 15 Torr.

## 2.2 Electrode Design

The electrode design that is presently being used is shown in Figure 2.1. There are a total of eight electrodes. Four serve as cathodes and four as anodes on each half cycle of RF voltage. Each set of four electrodes was connected to a common supporting endplate. These two structures were then mounted together, in an interdigital manner, such that each electrode face was flanked by an electrode of opposite polarity. When RF power was applied to this interdigital structure, independent discharge volumes and concomitant gain regions were created within the eight narrow gap slots separating the electrodes. The electrode gap was 5 mm. Each electrode was 4 cm x 3.5 cm x 50 cm and was fabricated of aluminium. The electrodes have subsequently been nickel coated using an electroless nickel deposition process. This was done to prevent the formation of an oxide coating on the electrodes, known to occur



with aluminium, which effectively confines the gas discharge.<sup>172</sup> In the initial design, the edges of all the electrodes were rounded off because it was feared that arcs caused by high field strengths might occur across the central region of the discharge structure. Indeed the fact that the tips of the electrodes were relatively far apart prevented the discharge from forming in the center of the volume. All the electrodes have two 64 mm internal passages running the entire length. This feature permitted cooling water to flow through one electrode and then return to the endplate through the other electrode.

As shown in Figure 2.1, and schematically in Figure 2.2, each electrode is electrically connected to only one endplate, the other end being insulated with ceramic alignment pins and ceramic spacers. On the end of the electrode with the electrical connection, two small stainless steel alignment pins were inserted into both the endplate and the electrode, so as to keep a constant 5 mm gap between all eight of the pie shaped electrode elements. Small Delrin tubes provide an internal water connection between each water passage and endplate. This tube is double O-ring sealed on each end to prevent any water leakage into the discharge volume.

### 2.3 Endplate Design

The endplates are also shown in Figure 2.1 and schematically in Figure 2.2. Each endplate was made of aluminium and was 3.2 cm thick. The plate consisted of two sections: an inner section which was connected directly to the electrodes; and an outer ring, which slips over the inner section to collect the cooling water. This outer collection ring is visible in Figure 2.2.

The inner endplate provided support for each electrode as well as the electrical and water cooling connections. Eight 6 mm wide by 41 mm deep slots were milled into each endplate to permit optical output coupling with the mirrors placed on the back side. The endplates had provision on their periphery for inlet and outlet cooling water flow.

The outer endplate slips over the inner endplate and was held in place by a series of O-ring seals. A metal ring was placed on the discharge side of the endplates, such that it overlapped both the inner and outer portions, and thereby served as an additional electrical

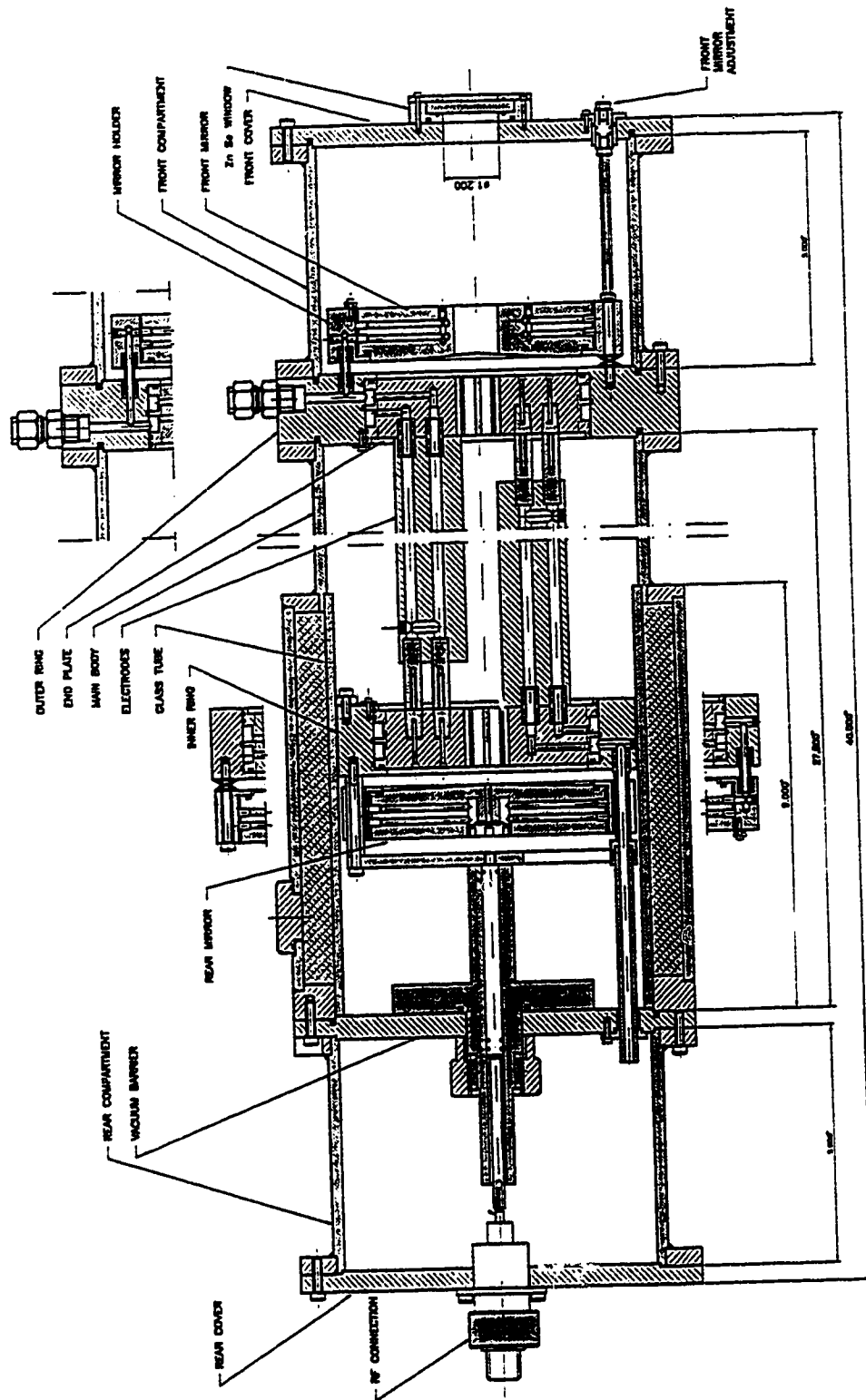


Figure 2.2 Schematic Diagram of the System Design

connection between them.

The endplate that was connected to ground was bolted directly to a flange on the main outer tube. The other endplate, which was connected directly to the RF coaxial cable, was of a smaller diameter to allow the entire assembly to fit inside a glass insulating tube, which in turn sat tight inside the main outer tube. This glass insulation was required to prevent the formation of arcs between the electrically "hot" endplate and the grounded outer tube. The back of the smaller endplate contained a series of connections for the electrical spider, which in turn was plugged directly into the RF coaxial cable. Both of the outer endplates also had provisions to attach the mirror mounts and water cooling channels for the optical systems.

#### **2.4 Outer Tube**

The main outer tube, 19.3 cm in diameter and 65 cm long, was made of aluminium to provide good RF interference shielding. Short extensions were fitted to both ends of the main vacuum enclosure to provide room for the resonator mirrors, output couplers and RF drive connector.

The entire laser head was mounted onto a movable bench containing the vacuum and gas handling system. Figure 2.3 shows a cutaway view of the complete system and Figure 2.4 is a photograph of the assembled discharge apparatus.

#### **2.5 RF Power Supply and Impedance Matching Network**

The RF power supply employed for the project was a Henry Radio, model 10000D. The supply was a linear power amplifier capable of delivering 10 kW of continuous output power at a frequency of 40.68 MHz. The unit was also designed to provide 20 kW on a 50% duty cycle. The output impedance was 50 ohms.

The power supply consisted of five main sections. First, a crystal-controlled oscillator unit, which operated at a fixed frequency of 40.68 MHz. If desired, an external oscillator may have been connected to the supply to permit operation between 40 and 50 MHz. The second and third stages were both solid state amplifiers that boost the original signal to 20 and 100

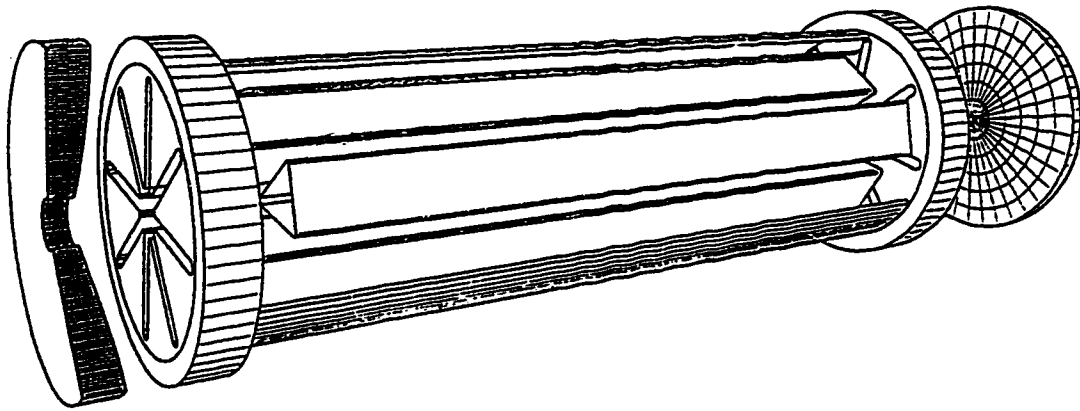
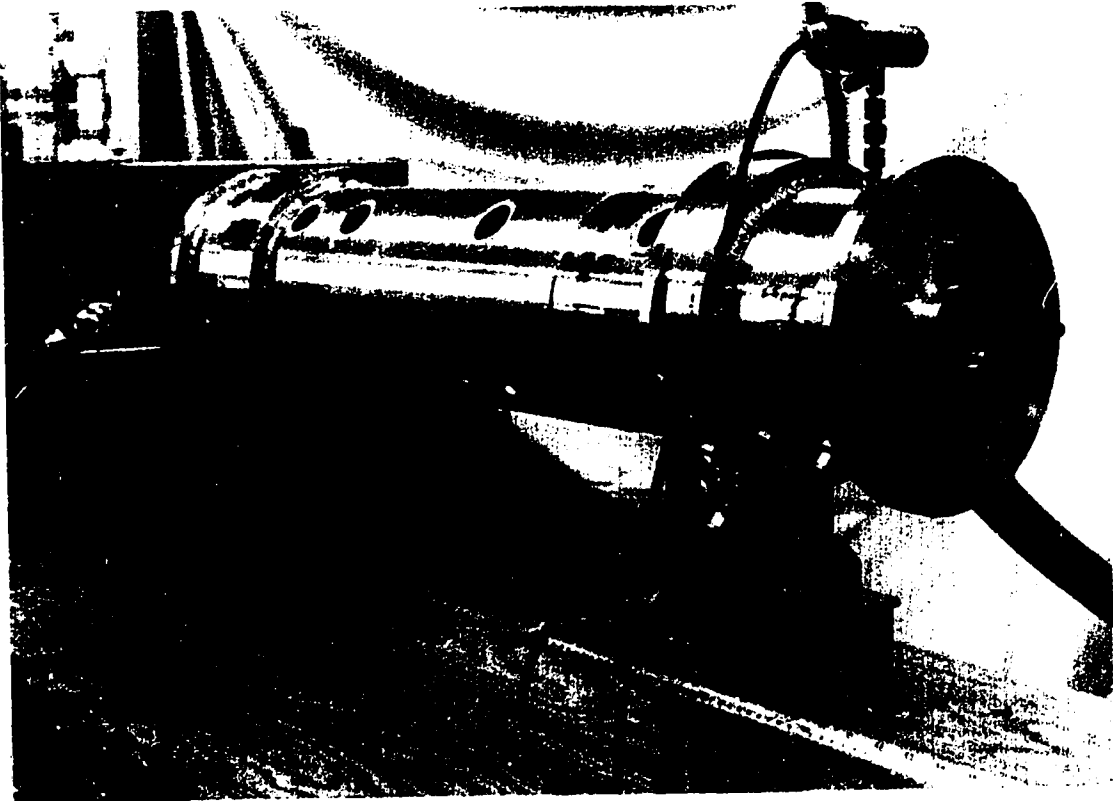


Figure 2.3 Cutaway View of the Complete Discharge Apparatus



**Figure 2.4 Photograph of the Assembled Discharge Structure**

W, respectively. The fourth and fifth stages were both based on ceramic/metal triode tubes, and amplify the output to a maximum of 500 and 10000 W, respectively.

The supply also had built-in forward and reflected power meters. In addition an overload protection circuit disengaged the amplifier if the reflected power increased above 1500 W.

Since the generator's impedance was  $50 \Omega$ , it was necessary to use a matching network to efficiently drive the laser head. The matching unit currently in use employed a Pi network consisting of a variable inductor connected between two variable capacitors. The unit was capable of matching load impedances over a broad range. One further component in the matching process was a set of parallel resonant inductors placed across each electrode gap. The rationale for these inductors is outlined below.

As mentioned at the beginning of this chapter, it was found that the discharge tended to concentrate at the end of the electrodes closest to the RF feed point. This feature is a common problem encountered with all RF-excited waveguide lasers.<sup>173-176</sup> Experience has demonstrated that there are two solutions to this problem. One is to increase the number of RF feed points to the system. In fact, the most uniform discharges have been obtained with only two RF connections, one at each end of the electrodes.<sup>174</sup> Due to the radial design of the present system, multiple feed points were not a viable option.

The second solution to this dilemma is the introduction of parallel, resonating inductors across each of the inter-electrode regions. These inductors also form part of the impedance matching network by helping to convert the laser head impedance into a pure resistance. The longitudinal voltage variation along each electrode depends on both the excitation frequency and the electrode length.<sup>67</sup> For the system under consideration herein, to maintain a voltage variation of  $\approx 5\%$  with 50 cm long electrodes at a frequency of 40.68 MHz, required the addition of only one inductor per inter-electrode region.

The value for these inductors was calculated in the following manner. Since it was desirable to balance the structure capacitance, a value of the inductor was chosen to make the dischargeless structure resonant at the operating frequency.<sup>18</sup> Consequently, the Pi matching



network need only balance the discharge impedance. By treating each slot as a parallel plate capacitor, the capacitance is given by:<sup>177</sup>

$$C = \frac{\epsilon_0 A}{d} \quad (2.2)$$

where  $C$  is the capacitance,  $\epsilon_0$  is the permittivity of free space ( $8.85 \times 10^{-12}$  F/m),  $A$  is the area of the electrodes and  $d$  is the electrode gap separation. The values of area and gap size are  $180 \text{ cm}^2$  and  $5 \text{ mm}$ , respectively, implying a capacitance of  $\approx 32 \text{ pF}$ . Therefore, to resonate at  $40.68 \text{ MHz}$ , an inductor value of  $480 \text{ nH}$  was required. These inductors were fabricated from 16 gauge copper wire and placed across each inter-electrode region midway down the electrode length.

The addition of these inductors allowed for a uniform  $\alpha$ -type discharge to be initiated in all eight of the inter-electrode regions. Various gas mixtures, including 1:1:8, 2:8:20 and 1:1:3 ( $\text{CO}_2:\text{N}_2:\text{He}$ ), at pressures of up to 35 Torr and input RF power levels of 7000 watts have been successfully operated.

In conclusion, uniform gas discharges could be operated simultaneously in all eight of the discharge regions over a wide range of pressures, gas mixtures and input power levels. System performance was sufficiently reliable to allow a detailed examination of its discharge properties and optical extraction characteristics. These aspects are described in the following chapters.

## CHAPTER 3

### GAIN AND SATURATION INTENSITY MEASUREMENTS

The previous chapter documented that it was possible to establish a stable gas discharge in all of the inter-electrode regions over a varying range of gas pressures, mixtures and input power levels. The next logical step was therefore to evaluate the ability of this discharge to amplify optical radiation. Two of the best indicators of lasing potential are gain and saturation intensity.<sup>178-180</sup> Both of these quantities were evaluated for this multichannel gas discharge structure under a variety of operational conditions.

#### 3.1 Theory and Experimental Technique

The theory and techniques of gain and saturation intensity measurements are well established.<sup>181-185</sup> The methods used herein will closely follow those of previous researchers.<sup>186-187</sup> An important factor in any study of gain and saturation parameters is the laser output lineshape. This is especially true in the case of saturation intensity. More specifically, the appropriate expressions for determining the gain and saturation intensity depend on whether the lineshape is dominated by homogeneous or inhomogeneous broadening mechanisms.

The primary homogeneous contribution arises from collisional broadening terms, whereas Doppler broadening effects manifest themselves as inhomogeneous broadening terms. Abrams<sup>188</sup> has shown that the homogeneously broadened linewidth is expressed by the relation:

$$\Delta\nu_H = 7.58(\psi_{CO_2} + 0.73\psi_{N_2} + 0.64\psi_{He})P(300/T)^{1/2} \text{ MHz} \quad (3.1)$$

where  $\Delta\nu_H$  is the linewidth (FWHM),  $\psi_i$  is the fractional content of component  $i$  of the gas mixture,  $P$  is the total gas pressure in Torr and  $T$  is the gas temperature in Kelvins. For a typical 1:1:3 = CO<sub>2</sub>:N<sub>2</sub>:He gas mixture at a total pressure of 15 Torr and 300 K, the

collisionally broadened linewidth is calculated to be 138 MHz.

Similarly, Yariv has derived an expression for the inhomogeneously broadened linewidth, due primarily to Doppler broadening effects. This expression is given by:<sup>189</sup>

$$\Delta\nu_D = \frac{2c}{\lambda} \left[ \frac{2k_B T \ln 2}{mc^2} \right]^{1/2} \quad (3.2)$$

where  $\Delta\nu_D$  is the linewidth,  $c$  is the speed of light,  $\lambda$  is the transition wavelength,  $k_B$  is Boltzmann's constant and  $m$  is the mass of the  $\text{CO}_2$  molecule. For a typical gas mixture used herein, this expression yields a Doppler broadened linewidth of  $\approx 53$  MHz.

Finally, Hansen<sup>190</sup> has presented an analysis of the combined effects of both broadening mechanisms. This analysis is considerably more complex than analyzing either homogeneous or Doppler broadening effects separately. This study indicates that including both homogeneous and inhomogeneous broadening terms is not necessary, and that the combined linewidth is only 7 % larger than that of a homogeneous broadening treatment alone. In addition, numerous experiments have been performed at still lower pressures, at which the effects of Doppler broadening should be more pronounced, with satisfactory results being obtained using only homogeneously broadened linewidth expressions.<sup>191-192</sup> For the above reasons, the additional computational complexity of including both collisional and Doppler broadening effects is not warranted. Thus, only a homogeneous analysis will be assumed for this work.

The amplification of a probe laser beam that is passed through the gain medium is given by:<sup>29</sup>

$$I_{\text{on}} = I_{\text{off}} e^{\alpha L} \quad (3.3)$$

where  $I_{\text{on}}$ ,  $I_{\text{off}}$ ,  $\alpha$  and  $L$  are the intensity of the probe beam when the discharge is on and off, the gain coefficient and the total gain length, respectively. For these experiments, the total double pass gain length is 90 cm. Since both the reference and amplified beams may be

arranged to pass through the same window and reflected off the same mirrors, the effects of these elements cancel out in the above equation. Therefore, the gain coefficient is easily calculated from:

$$\alpha = \frac{1}{L} \ln \left[ \frac{I_{\text{on}}}{I_{\text{off}}} \right] \quad (3.4)$$

The saturation intensity is defined as the point at which the excitation of the upper laser level is exactly balanced by the losses from that level.<sup>189</sup> For a homogeneously broadened medium, gain saturation is given by the solution to the equation:<sup>191</sup>

$$\frac{dI}{dz} = \frac{\alpha_0 I}{1 + (I/I_{\text{sat}})} \quad (3.5)$$

where  $I$  is the intensity of the probe beam,  $I_{\text{sat}}$  is the saturation intensity,  $\alpha_0$  is the small signal gain coefficient and  $z$  is the axial length coordinate. Integration of equation (3.5) yields:

$$\ln \left[ \frac{I_{\text{on}}}{I_{\text{off}}} \right] = - \left[ \frac{I_{\text{on}} - I_{\text{off}}}{I_{\text{sat}}} \right] + \alpha_0 L \quad (3.6)$$

with all the terms being previously defined. Examination of this equation reveals that a plot of  $\ln(I_{\text{on}}/I_{\text{off}})$  versus  $(I_{\text{on}} - I_{\text{off}})$  will yield a straight line of slope  $-1/I_{\text{sat}}$ , and with a  $y$ -intercept equal to the true small signal gain coefficient times the total gain length.

Equation (3.6) is based on the assumption that thermal equilibrium has been established between the various vibrational levels of the molecular gases. It has been shown that the process with the largest time constant is the resonant energy transfer from excited  $N_2$  to the upper  $CO_2$  laser level, having a rate constant of  $k \approx 1.9 \times 10^4 \text{ Torr}^{-1} \cdot \text{sec}^{-1}$ .<sup>19</sup> Since the laser that will be used to produce the probe beam is pulsed, care must be exercised to ensure that thermal equilibrium will be established. The lowest pressure of  $CO_2$  that will be used in

any of the experiments is 1 Torr, and therefore a time constant of  $\approx 50 \mu\text{sec}$  is typical for one of these mixtures. In order to ensure equilibrium, a probe laser pulse of at least 5 time constants will be used.

The physical apparatus used to perform the experiments is shown schematically in Figure 3.1. A low power RF  $\text{CO}_2$  waveguide laser, operating at  $10.6 \mu\text{m}$ , was used to provide the probe beam. This laser had the advantage of an external power modulation control box, which allowed the output pulse width, frequency and power to be continuously varied. In light of the thermal equilibrium requirements discussed above, an output pulse width of  $280 \mu\text{sec}$  at a repetition frequency of 500 Hz was chosen for the experiments reported herein. These parameters, combined with an average beam diameter of 2.34 mm, allows the intensity of the probe beam to be calculated from the relation:<sup>193</sup>

$$I(\text{W}/\text{cm}^2) = \frac{P_{av}(\text{W})}{A\tau f} \quad (3.7)$$

where  $I$ ,  $P_{av}$ ,  $A$ ,  $\tau$  and  $f$  are the intensity of the beam, average power of the beam (in watts), area of the probe beam, pulse width and pulse repetition frequency, respectively. Using the previously given parameters, the intensity of the beam is given as:

$$I(\text{W}/\text{cm}^2) = 161 P_{av}(\text{W}) \quad (3.8)$$

The probe beam was passed through a variable attenuator and into the discharge region. It was then reflected from an adjustable aluminium alloy mirror to make a second pass through the gain medium, and finally directed into a power meter by an adjustable turning mirror. A helium-neon laser was mounted colinearly with the probe beam to facilitate alignment.

The variable beam attenuator was added as a provision to adjust the probe laser power without actually making any adjustments to the laser itself. In this manner, the probe laser can reach its equilibrium operating point and be left untouched. The attenuator was

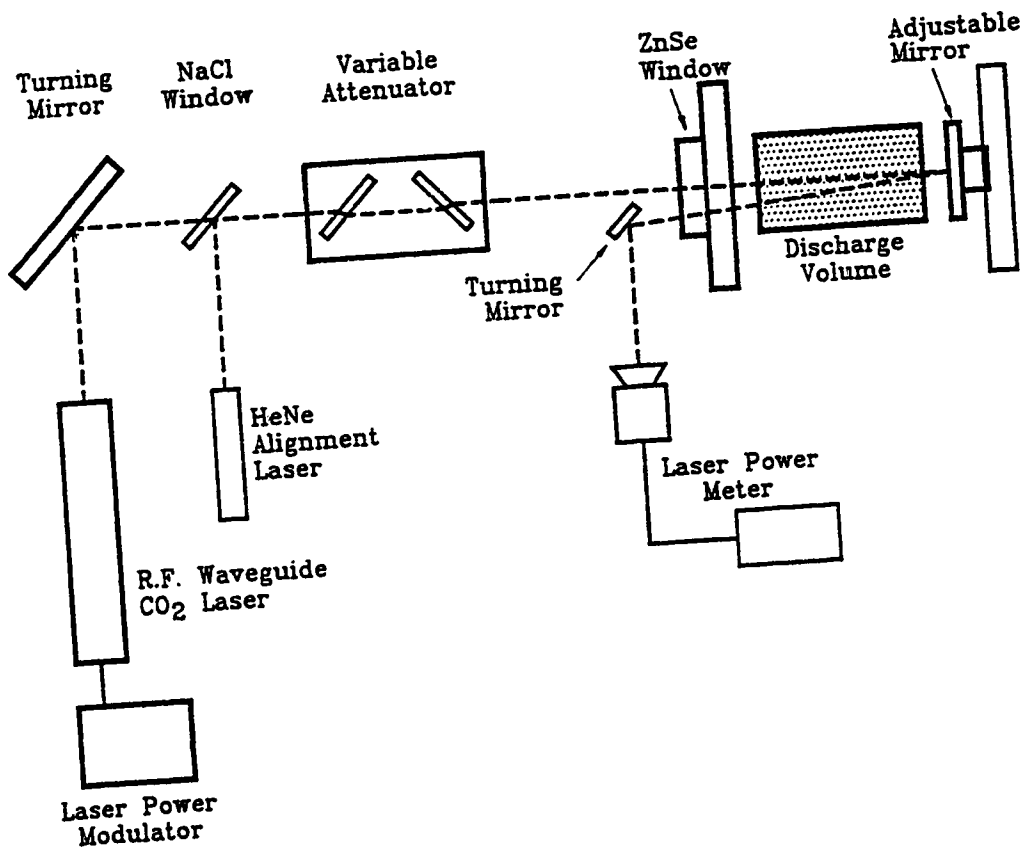


Figure 3.1 Block Diagram of the Gain and Saturation Intensity Measurement Apparatus

developed previously in our laboratory and is based on the principle of reflection and transmission of light through a dielectric medium. It is well known that the transmission properties of a dielectric vary with the angle of incidence of the incoming optical radiation.<sup>194</sup> Therefore, by introducing a dielectric plate in the beam path (NaCl in this case) a continuously variable transmitted power is achieved by a simple rotation of the dielectric plate. A second plate, of equal thickness and rotating in a direction opposite to that of the first, is introduced to correct for the displacement of the light beam. In this fashion, the probe beam power or intensity may be continuously adjusted from near zero to its maximum, by the simple rotation of the attenuator plates.

### 3.2 Gain Measurement Results

Based on the methods and discussion of the previous section, a series of gain measurements were undertaken under various discharge operating conditions. One of the foremost questions to be addressed is that of the gain in the different discharge regions of the system. In other words, is the gain coefficient the same in the different channels of the structure?

To answer this, the gain was measured in a number of different channels. A constant gas mixture of 1:1:3 = CO<sub>2</sub>:N<sub>2</sub>:He at 13 Torr at an input power level of 2 kW was used for these tests. The probe beam was aligned to pass down the center of each tested channel and return through the same channel after reflecting from the adjustable back mirror. Due to the symmetry of the structure, only four different channels were actually probed. The four channels chosen were the top and bottom vertical slots, a horizontal slot and one of the channels oriented at a 45° angle to both the vertical and horizontal axes. It was felt that these channels would provide a good representation of the entire system. Additionally, they would give an indication of any non-uniformities in the gain which, for example, may be caused by convection of hot gas between the slots. The gain coefficient in each of the channels described above, and its associated standard deviation, was found to be:  $0.645 \pm 0.014$  %/cm,  $0.645 \pm 0.041$  %/cm,  $0.695 \pm 0.088$  %/cm and  $0.623 \pm 0.074$  %/cm, respectively. Thus, it was found

that within the accuracy of the measurements, the gain in each of the different discharge regions was the same.

The variation of the gain coefficient with the total gas pressure, at a constant input power of 2 kW and a constant 1:1:3 = CO<sub>2</sub>:N<sub>2</sub>:He gas mixture, is shown in Figure 3.2. The gain is seen to exhibit a fairly broad maximum around 15 Torr. The trend of this curve, and the value of gain coefficient, are similar to other investigations.<sup>180</sup> The gradual roll-off of the gain with increased pressure is usually explained as being due to the increased collisional de-excitation of the upper laser level with increasing pressure.

The effect of the RF input power on the gain is shown in Figure 3.3. These measurements were performed at a constant gas pressure and mixture ratio. As can be seen, the gain increases with increasing power until about 2 kW and then begins to fall off. This effect is well known and is due to the fact that increasing the input power beyond a certain point raises the gas temperature, with a concomitant reduction of the population inversion and the gain coefficient.<sup>195</sup>

Experiments were also performed to evaluate the effect of each of the gas constituents on the gain coefficient. These results are depicted in Figures 3.4 to 3.6. In all of these cases, the two gas components that were not varied were held constant at values of 3, 3, or 9 Torr for CO<sub>2</sub>, N<sub>2</sub>, and He, respectively. The input power level was also kept constant at 2 kW.

Figure 3.4 shows the effect of varying the CO<sub>2</sub> partial pressure. The gain is seen to increase as the partial pressure is increased until a maximum value is reached near 4 Torr. As anticipated, there is no gain detectable when there is no CO<sub>2</sub> present in the gas mixture. The decrease in gain above  $\approx$  4 Torr is the result of the increased amount of power transferred to the excitation of the bending and stretching modes of CO<sub>2</sub>. This is opposed to vibrationally exciting the nitrogen, with a subsequent CO<sub>2</sub> upper laser level excitation.<sup>196</sup>

Nitrogen variation, as shown in Figure 3.5, exhibits a similar but broader gain curve, with gain increasing with partial pressure up to a peak at  $\approx$  4 Torr. The gain with no nitrogen present is found to be roughly one half of the maximum value. This finding is consistent with the enhanced efficiency of upper laser level excitation through collisions with vibrationally



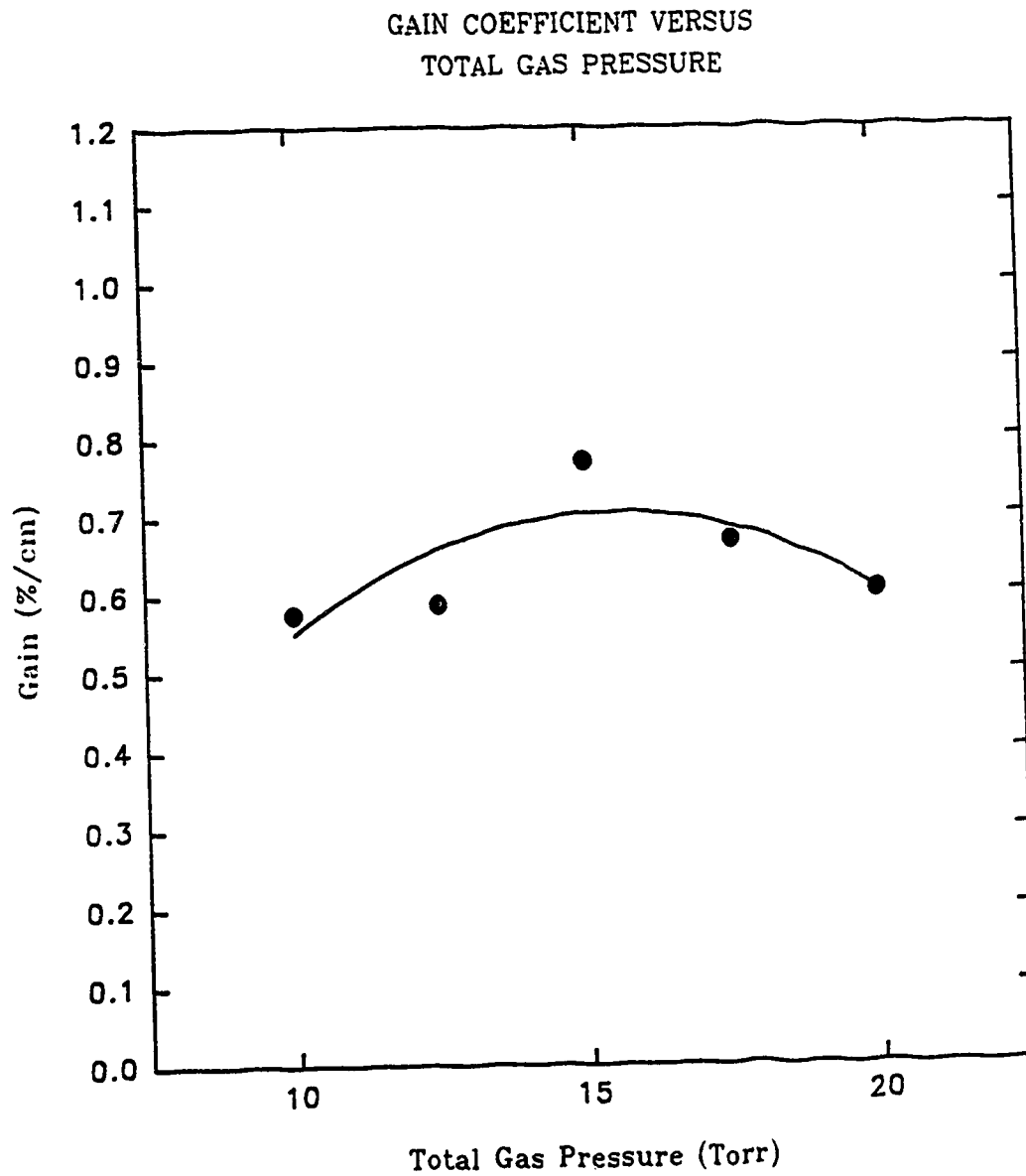


Figure 3.2 Variation of the Gain Coefficient with the Total Gas Pressure

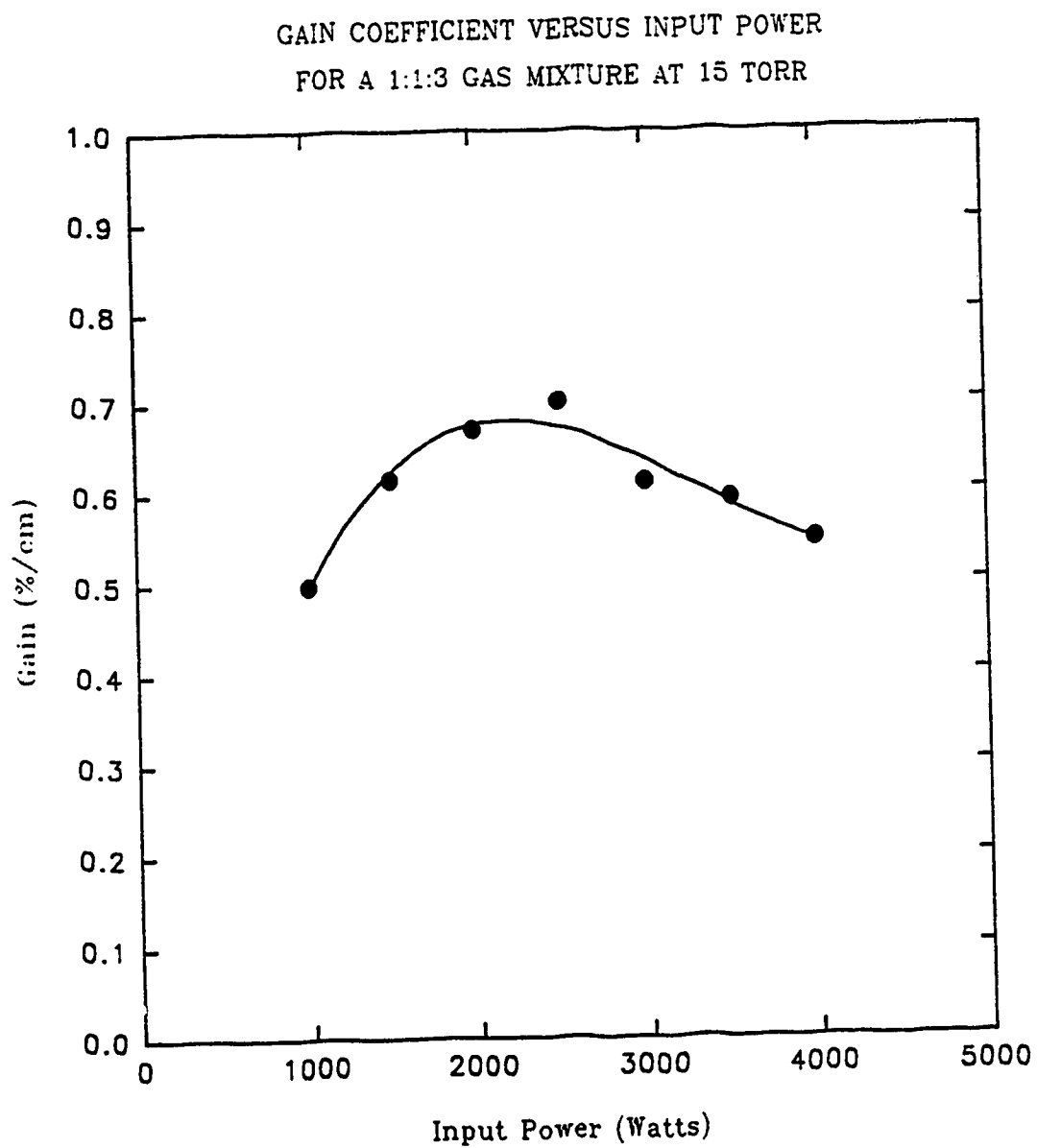


Figure 3.3 Variation of the Gain Coefficient with the RF Input Power

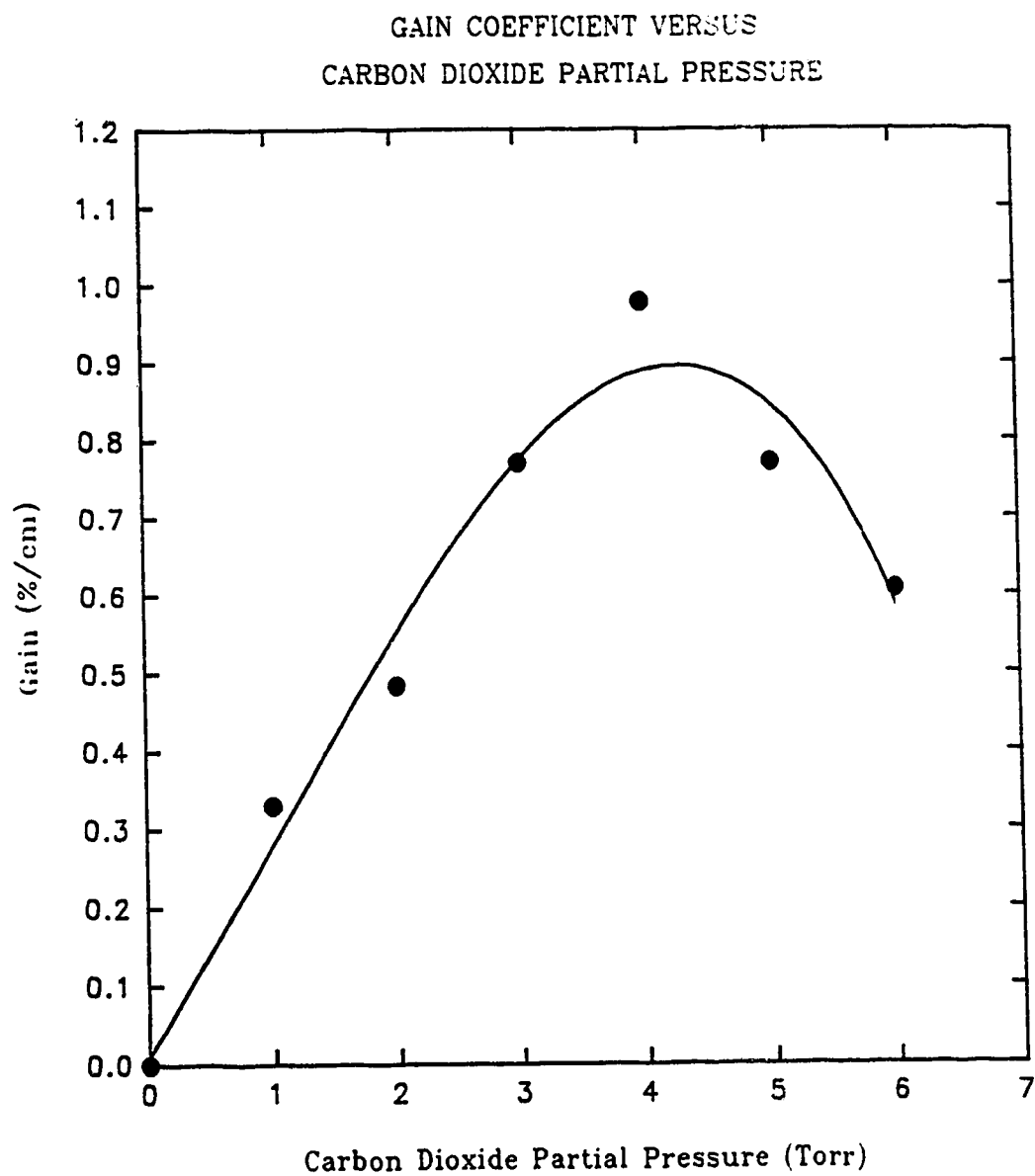


Figure 3.4 Variation of the Gain Coefficient with the CO<sub>2</sub> Partial Pressure

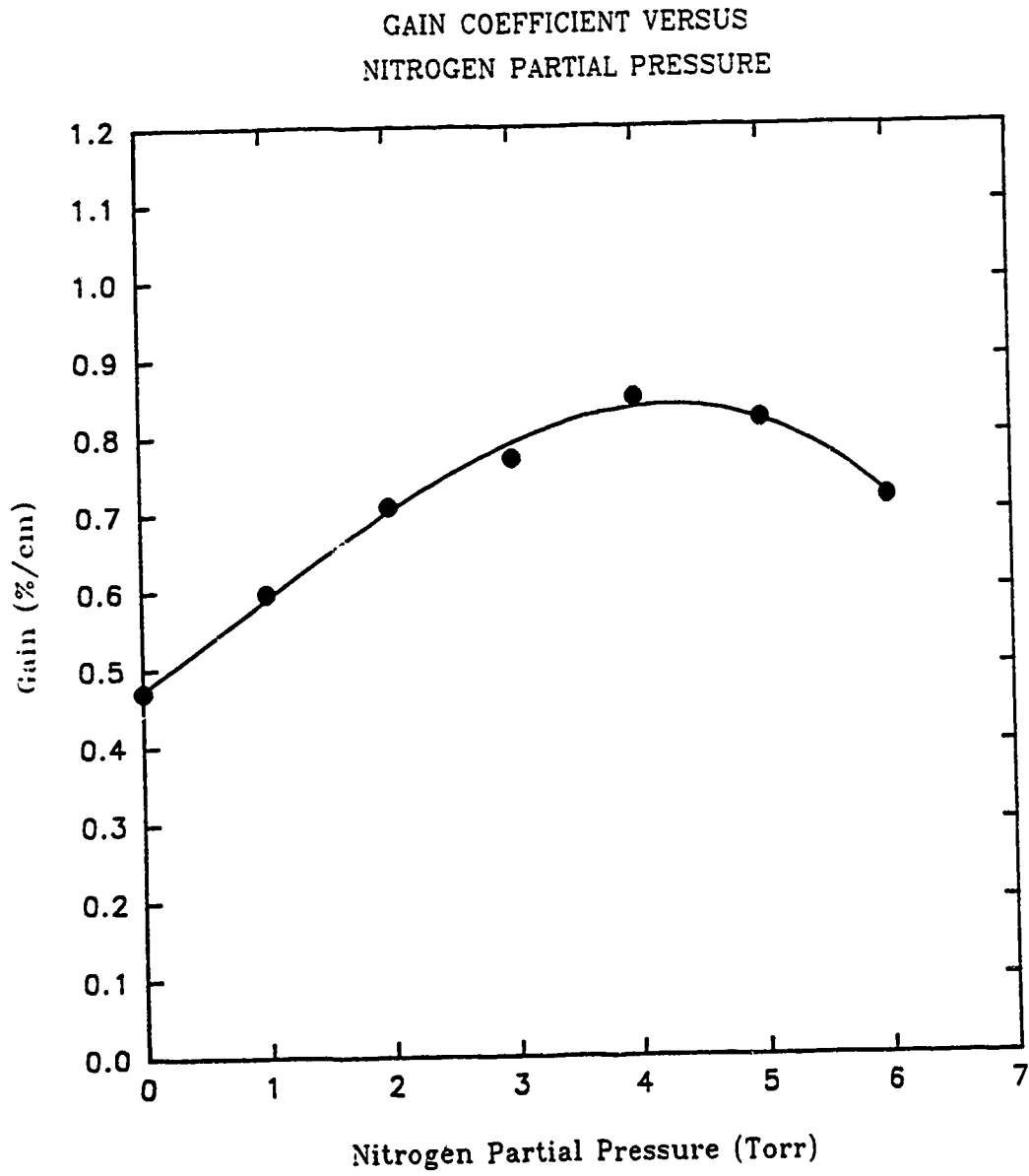


Figure 3.5 Variation of the Gain Coefficient with Nitrogen Partial Pressure

excited nitrogen molecules, even with the addition of small amounts of nitrogen.<sup>19</sup>

Over the range of pressures investigated herein, there is essentially no variation of the gain coefficient with helium partial pressure, as is shown in Figure 3.6. This phenomenon is explained by Lowke *et al.*<sup>196</sup>, and is essentially that the variation of helium pressure has no significant impact on the excitation efficiency of the discharge. It does, however, influence the de-population of the lower laser levels and hence the population inversion. It would appear that, for the device in consideration here, an amount of helium at least equal to the amount of CO<sub>2</sub> and N<sub>2</sub> in the discharge is sufficient to effectively depopulate the lower laser level.

One final series of gain measurements were made to complete this study. As discussed in Chapter 2, the central region of the discharge structure contains no visible discharge. However, it is known that gain may still exist in regions of no discharge. For example, it has been observed that excited species may be blown out of the discharge region in a flowing gas laser system.<sup>187</sup> There is nothing to preclude a similar phenomenon from occurring here, except that the particle transport mechanism would be primarily due to the diffusion of vibrationally excited species into this central zone.

Measurements of the gain coefficient in the central region were performed over a varying pressure range at a constant 2 kW input power level and with a 1:1:3 = CO<sub>2</sub>:N<sub>2</sub>:He gas mixture. To conduct these tests, the probe laser beam entered and emerged from the discharge chamber  $\approx$  5 mm from the nearest electrode slot region. The results of these measurements are presented in Figure 3.7. As is evident, a substantial amount of gain does indeed exist in this region, and is  $\approx$  25 % of the value found for the gain coefficient within a discharge channel under the same operating conditions. The linear decrease in the coefficient with increasing pressure is accounted for by the decrease in mean free path length with increasing pressure.<sup>197</sup> As the total gas pressure in the system rises, there is a larger probability of a collisional de-excitation of any vibrationally excited species that diffuse into this central region, and hence the observed gain is reduced. In spite of this however, the fact that a significant amount of gain is observed in this region may have a pronounced effect on the ability to phase-lock the individual discharge channels. The presence of gain in the central

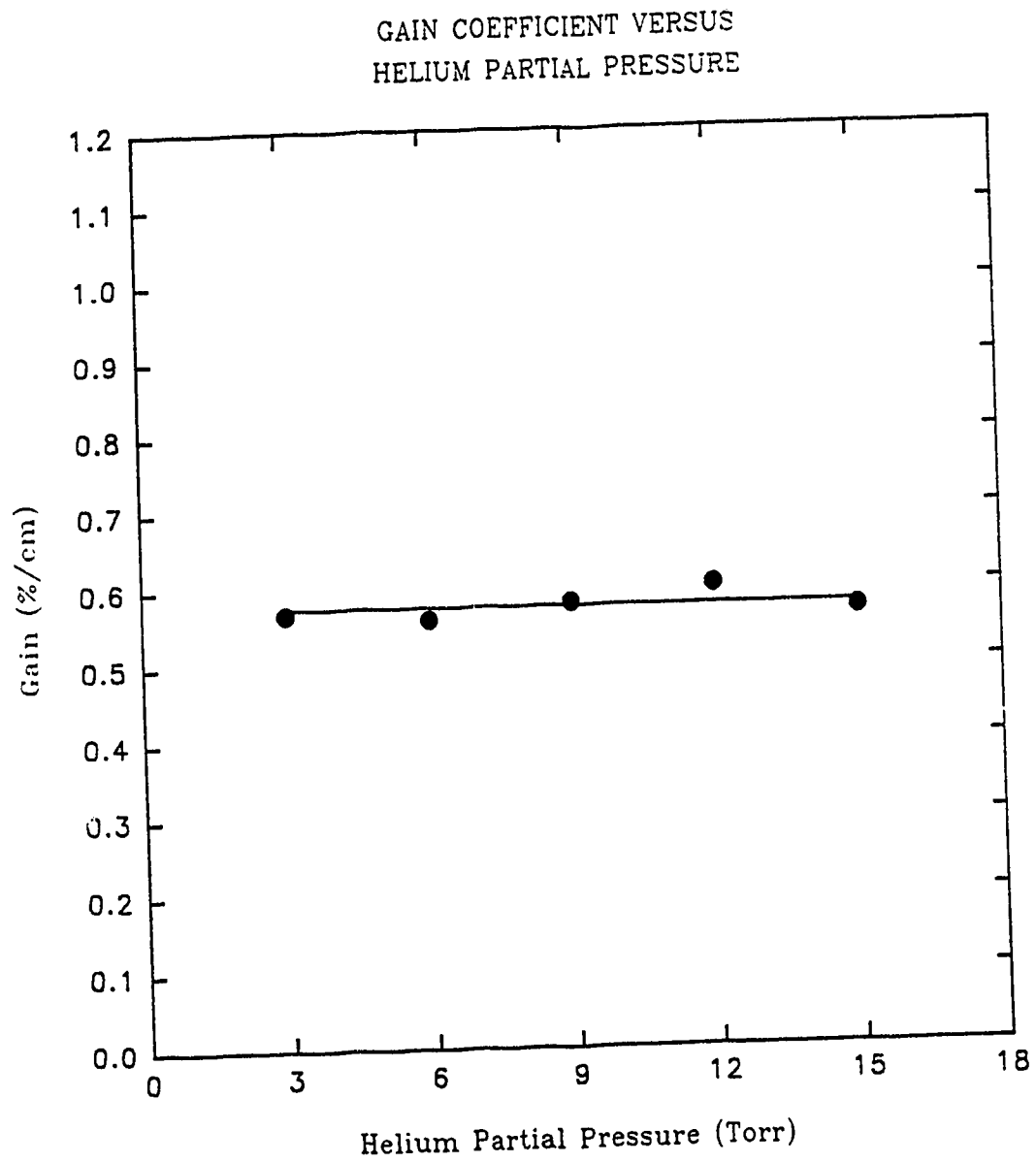


Figure 3.6 Variation of the Gain Coefficient with Helium Partial Pressure

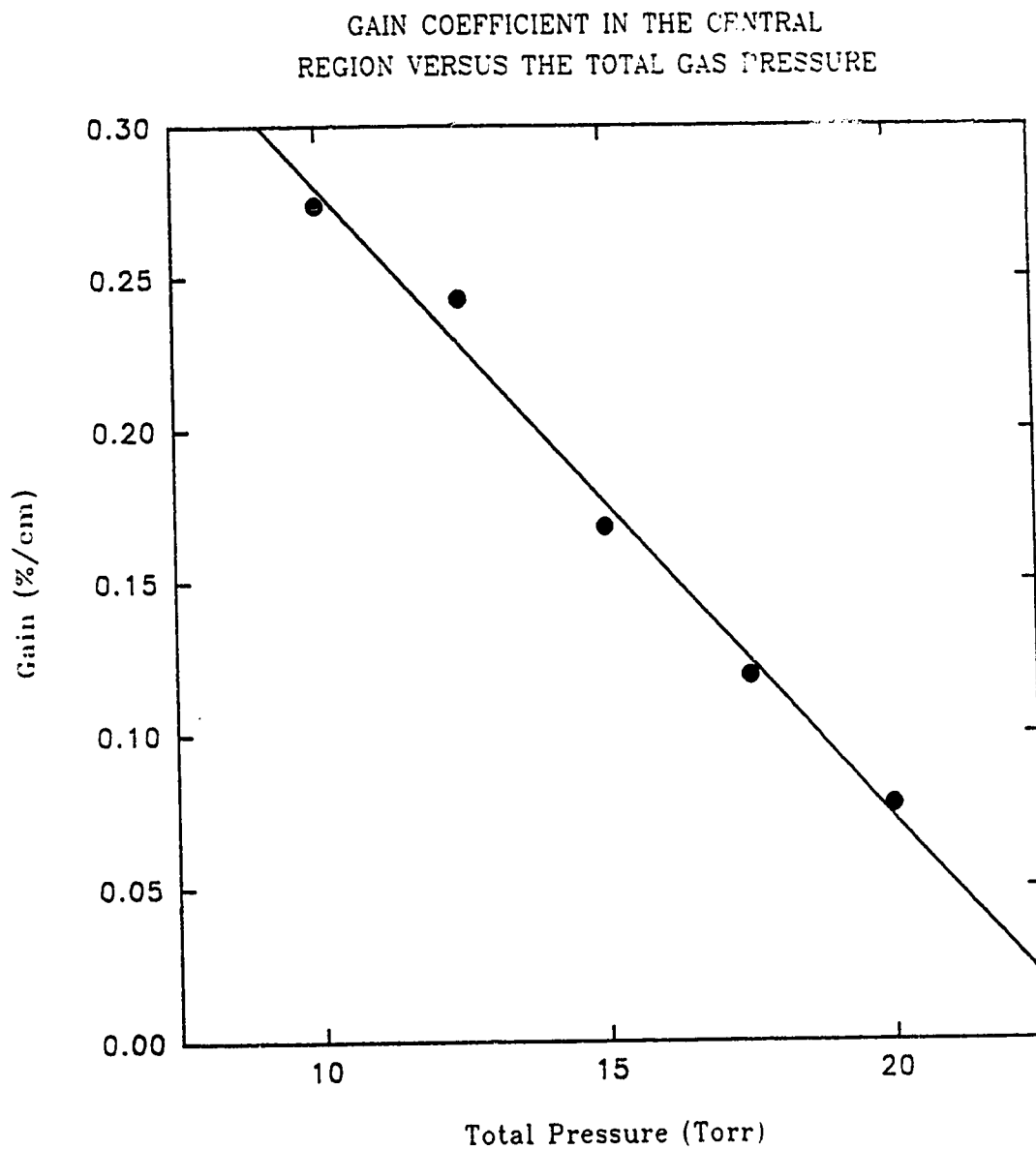


Figure 3.7 Variation of the Gain in the Central Inter-electrode Region as a Function of Pressure

region may enable a coupled optical resonator through beam-combining, as was discussed in Chapter 1.

### 3.3 Saturation Intensity Measurements

The saturation intensity of the multi~~channel~~ discharge device was also investigated. This parameter was measured at various total gas pressures with a constant gas mixture ratio of 1:1:3 = CO<sub>2</sub>:N<sub>2</sub>:He and at a fixed input power level of 2 kW. As outlined in section 3.1, the saturation parameter was obtained by making a gain coefficient measurement at several different probe laser intensities. The results of this are then plotted according to equation (3.6).

Figures 3.8 and 3.9 show the results of such a plot for two representative gas pressures of 12.5 and 17.5 Torr, respectively. From this data, the saturation intensity was determined to be 833 W/cm<sup>2</sup> at 12.5 Torr and 1516 W/cm<sup>2</sup> at 17.5 Torr. Likewise, the true small signal gain coefficient was found to be 0.674 %/cm and 0.763 %/cm for these pressures. These values are in reasonable agreement with those of other investigations.<sup>179,180,185</sup>

The variation of the saturation intensity with total gas pressure is depicted in Figure 3.10. This graph is a log - log plot to emphasize the square law relationship between saturation intensity and total gas pressure. The slope of the best fit line to these points is 1.96, which agrees well with theory. The squared dependence is the result of two contributing factors<sup>197</sup>: (i) the number of molecules within the homogeneous linewidth increases linearly with pressure, and (ii) the vibrational relaxation rate of the upper laser level also depends linearly on pressure.

Finally, Figure 3.11 shows the variation of the product of gain coefficient and saturation intensity with pressure. Again this data is for a constant gas pressure and input power level. The variation of the product of these two parameters is important since it is this product that determines the output power available from a given laser system.<sup>181</sup> As may be seen, the available intensity increases with pressure until it saturates at about 10 W/cm<sup>2</sup>. Eventually, with increasing pressure, the available intensity will begin to decrease still further.



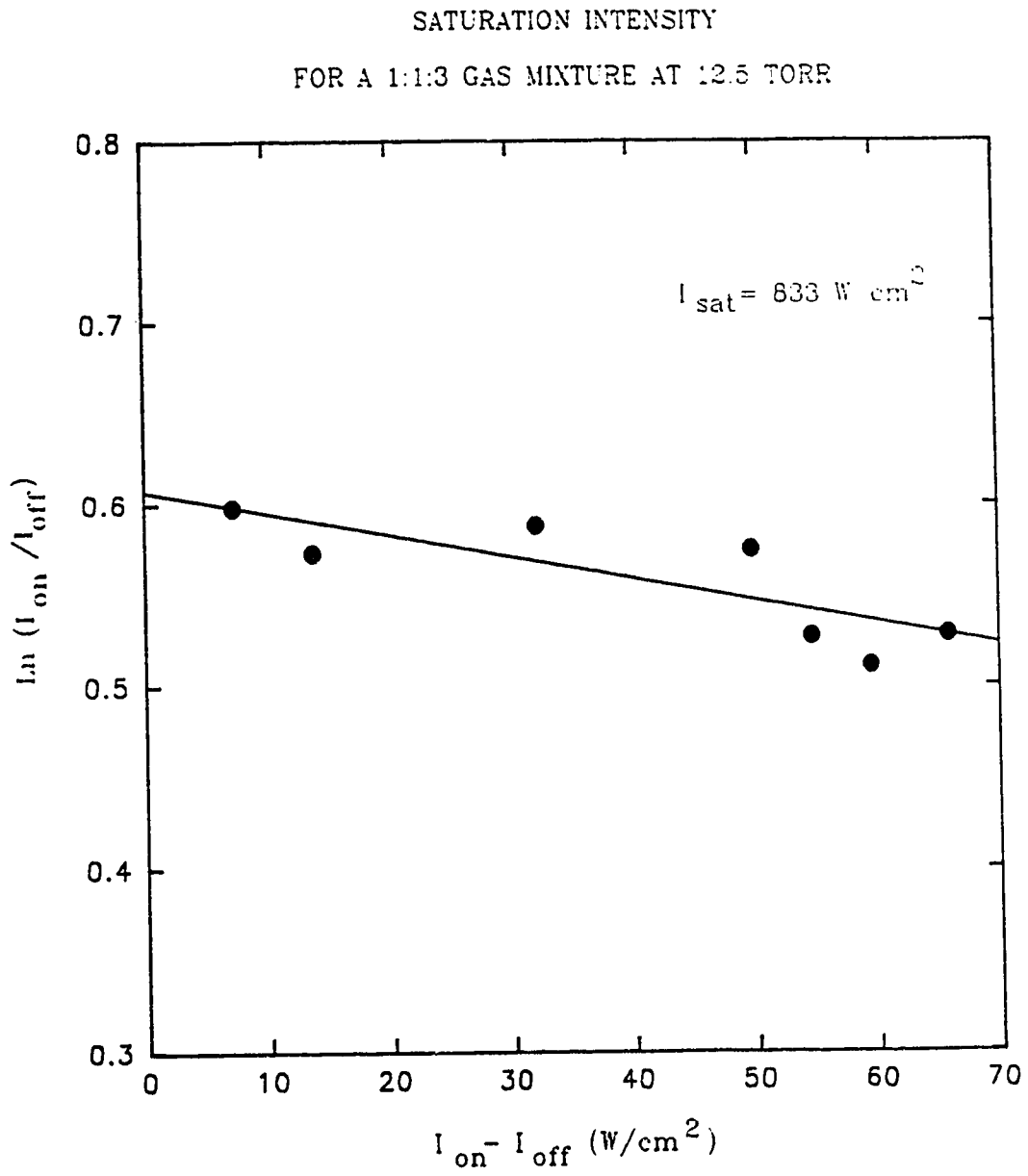


Figure 3.8 Saturation Intensity for a 12.5 Torr Gas Pressure

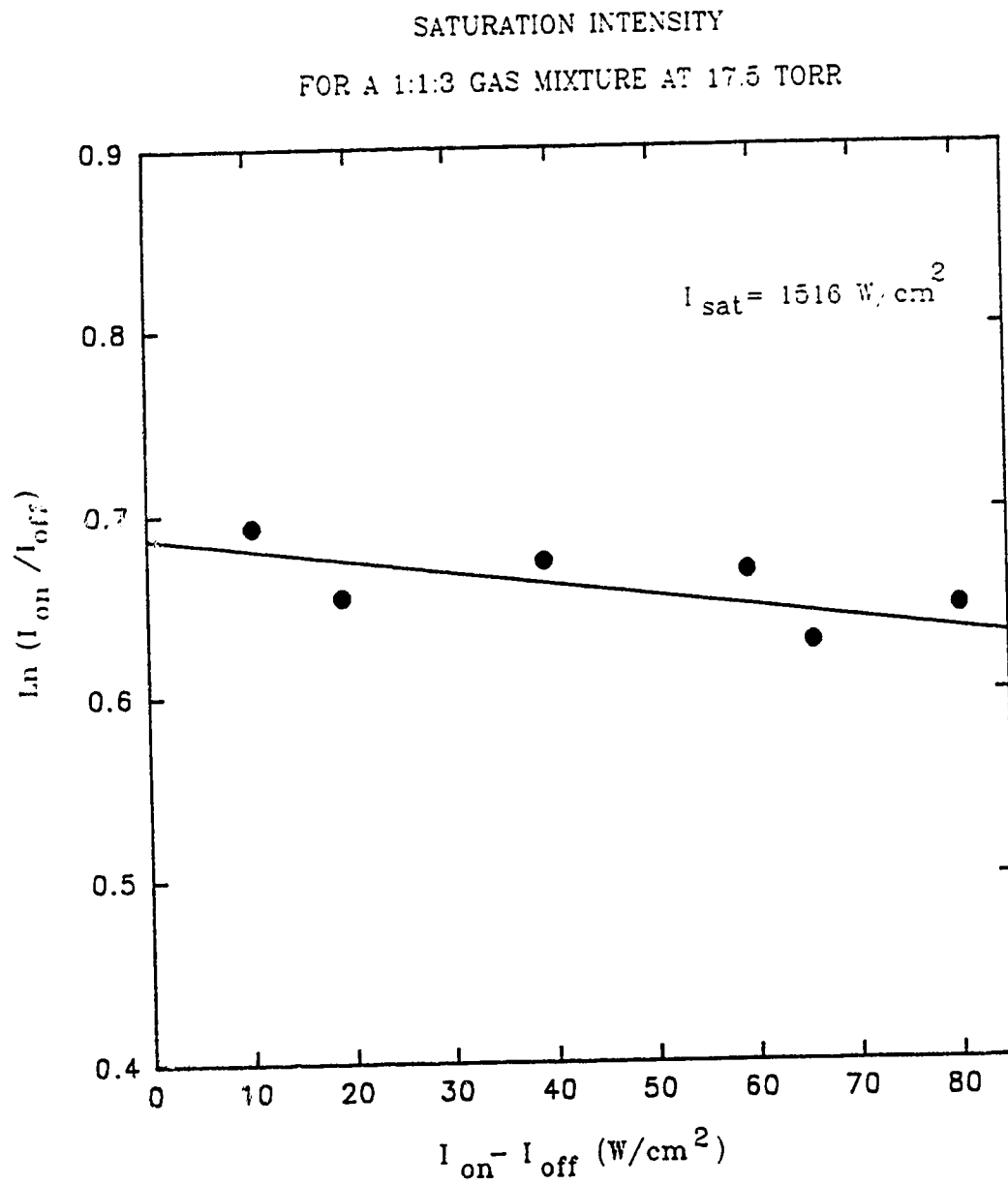


Figure 3.9 Saturation Intensity for a 17.5 Torr Gas Pressure

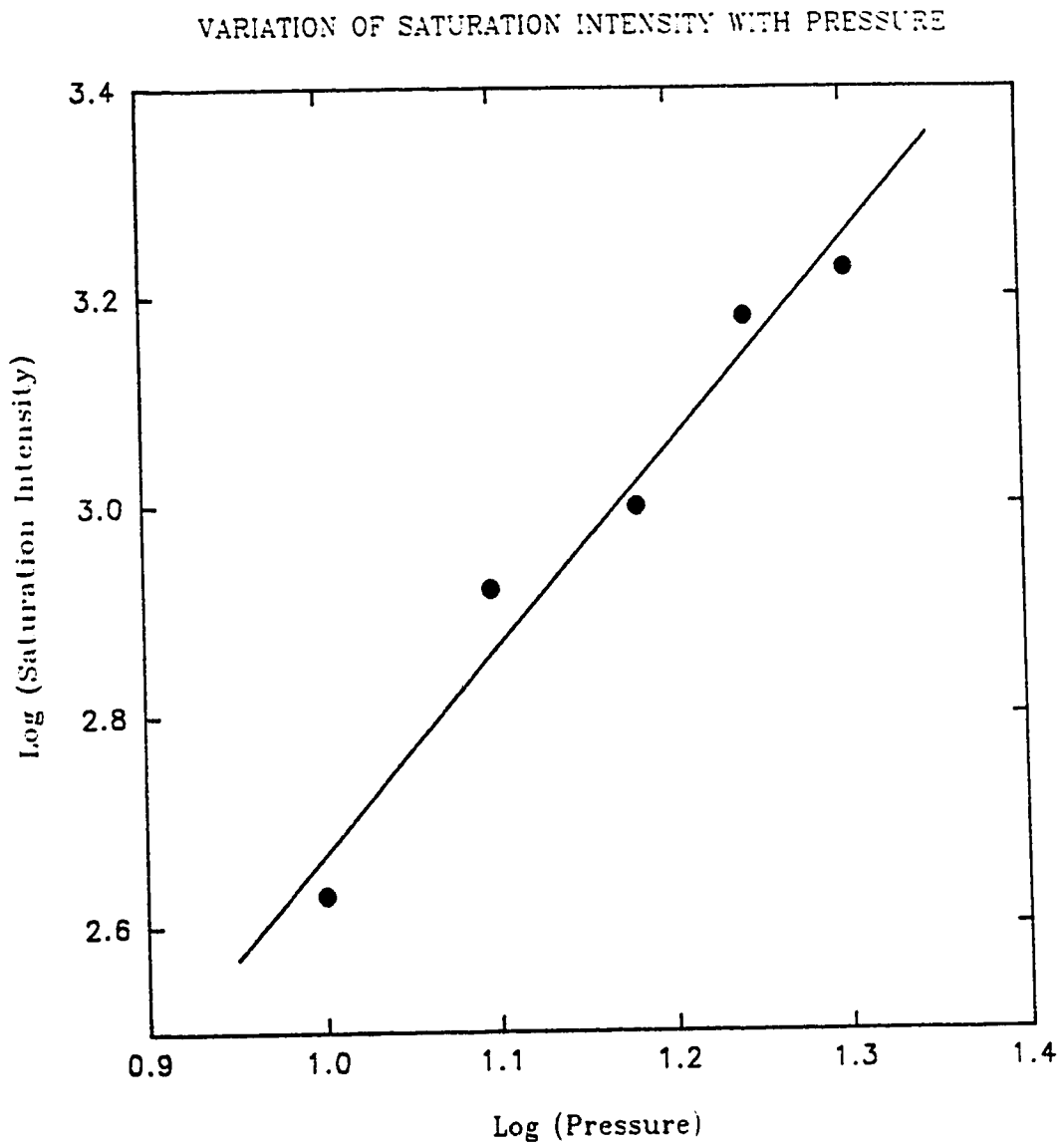


Figure 3.10 Variation of the Saturation Intensity with the Total Gas Pressure

VARIATION OF THE GAIN - SATURATION  
PARAMETER PRODUCT WITH TOTAL GAS PRESSURE

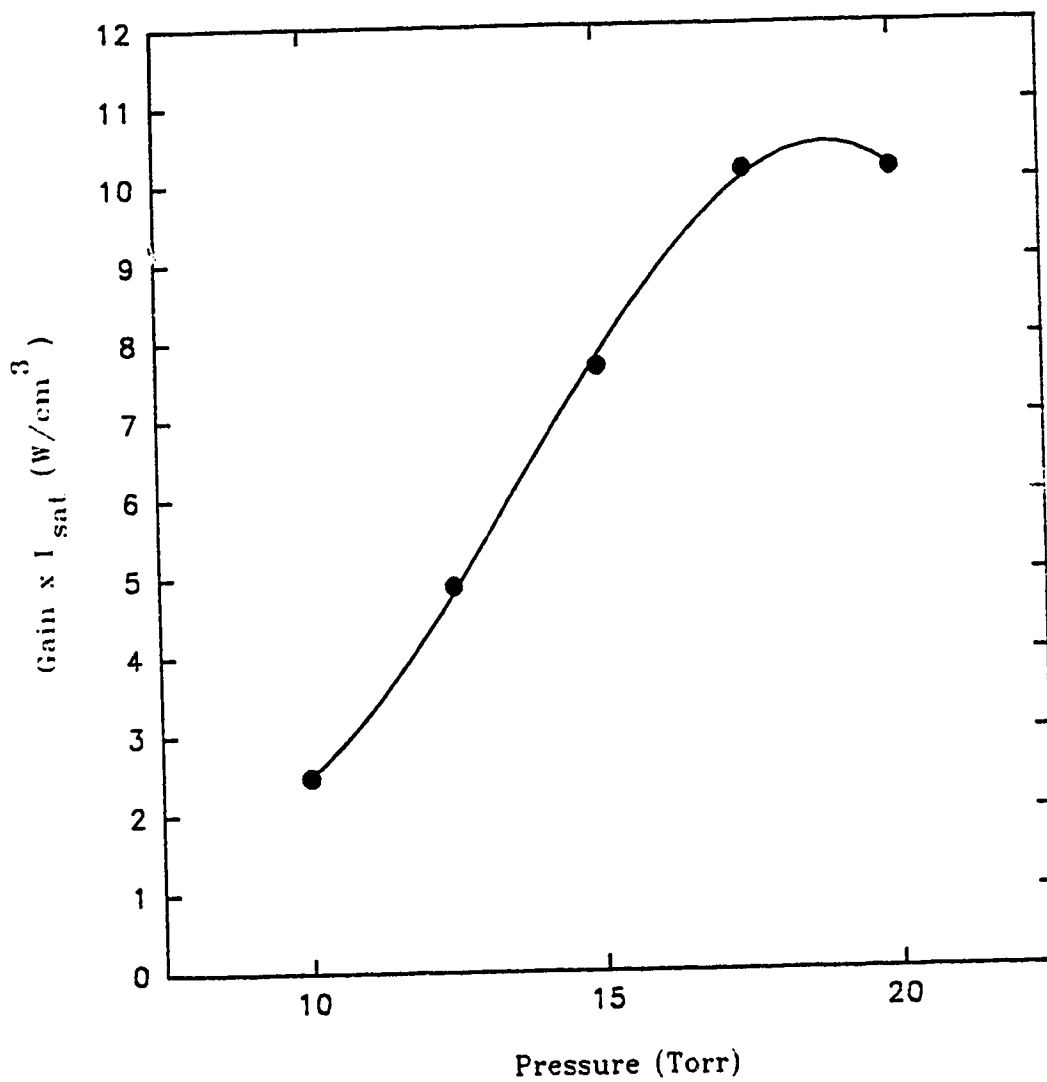


Figure 3.11 Gain Coefficient - Saturation Intensity Product Variation with Pressure

This is because, even though the saturation intensity increases, the gain decreases at a faster rate with rising pressure.<sup>181</sup>

In summary, it has been shown that the unique multichannel gas discharge device investigated herein is indeed well suited for optical energy extraction experiments. Measurements of the gain coefficient and saturation intensity parameter have clearly documented this point. Additionally, the observation of gain in the central, dischargeless region of the system is very encouraging, and suggests the possibility of initiating a coupled optical beam approach to phase-locking of the individual channels in the device.

## CHAPTER 4

### OPTICAL EXTRACTION SYSTEMS

The previous chapters have documented that the extended-area electrode and multichannel array approaches to discharge scaling are indeed well suited to compact laser systems. This fact was particularly emphasized by the gain and saturation intensity parameters observed for such devices. This chapter presents the results of a comprehensive series of optical resonator experiments performed on the aforementioned gas discharge structure. Included in these tests were: output power characteristics, focal spot sizes, alignment sensitivity, and the polarization properties of several different resonator configurations.

#### 4.1 Optical Resonator Background

As with any laser system, there were several different optical resonator designs that could have been used with this structure. All of these possible configurations fall into two broad categories, with numerous variations within these two groups. The two fundamental resonator designs were the stable resonator and the unstable resonator.

The use of a stable resonator would have been straight forward but it also would have introduced some inherent disadvantages. The two major shortcomings would have been the fact that a stable resonator has a very small mode volume<sup>29</sup>, and that one of the mirrors had to be partially transmitting to allow for the extraction of the output beam. For the above reasons, a stable resonator design was not seriously considered for this multichannel laser system. However, the unstable resonator category warranted further investigation.

Because of their unique modal characteristics, unstable resonators have long been a topic of special emphasis concerning high power lasers. First reported by Siegman over a quarter century ago<sup>198</sup>, numerous theoretical and experimental studies of this special class of optical cavity have periodically appeared in the scientific literature.<sup>199-216</sup> As a result, salient features and advantages offered by unstable resonators have gradually become better understood. These include:<sup>217</sup> large mode volumes; good transverse mode discrimination;

controllable diffractive output coupling; efficient power extraction; and high quality far-field beam profiles. The ability to utilize single-ended, all metallic, water-cooled mirrors has also been an important feature prompting the incorporation of unstable resonators in high powered devices.

Design procedures for the fabrication of an unstable resonator system have been widely documented for specific cases. These include: collimating confocal resonators<sup>217,218</sup>, in which both of the resonator mirrors have a coincident focus, symmetric double-ended resonators, as well as asymmetric single-ended systems.<sup>217</sup> In some instances, the analysis has been quite elementary; requiring only a knowledge of the resonator length and mirror curvatures. Conversely, elaborate investigations such as Chernin's confocal study<sup>218</sup>, require a detailed knowledge of the gain and loss mechanisms within the active media.

A resonator is defined to be either stable or unstable by an analysis of its  $g$ -parameters, defined by:<sup>217</sup>

$$g_1 = 1 - \frac{L}{R_1} \quad (4.1)$$

where  $L$  is the mirror separation and  $R_1$  is the mirror radius of curvature. If the focus of the mirror is on the cavity side of the mirror then  $R_1$  is defined as being positive. If the condition that

$$0 \leq g_1 g_2 \leq 1 \quad (4.2)$$

is satisfied, then the resonator is classified as being stable. A value of  $g_1 g_2$  outside of this range corresponds to an unstable optical resonator, in which optical energy from the resonator is extracted primarily by diffraction over the edge of the smaller secondary mirror. The resonator stability diagram is shown in Figure 4.1 with regions of stable operation shaded. Output from such a resonator is characteristically annular in shape, with a typical full beam diameter on the order of several centimeters.<sup>219,220</sup> In most applications this beam is coupled

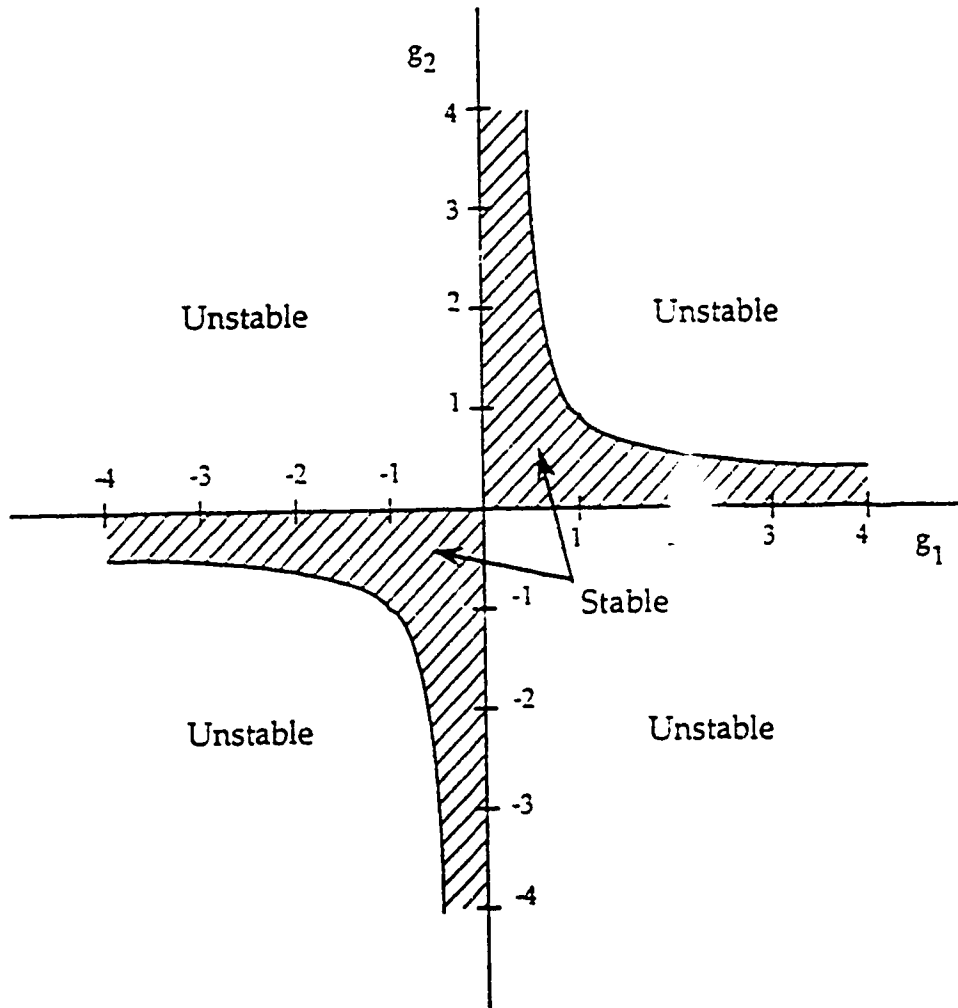


Figure 4.1 Resonator Stability Diagram



out of the laser vessel through a relatively large, and therefore expensive, ZnSe window. If desired, the beam may first be compacted with an additional optical element, such as an axicon, before exiting the laser structure<sup>221</sup>, or it may be extracted through an aerodynamic window.<sup>11,222</sup>

A variation on the traditional unstable resonator concept has also been investigated as an alternative to conventional optical extraction systems. These cavities were modified versions of the toric, or unobscured unstable resonator, which was first proposed by Reilly<sup>223</sup>, and later re-examined by Townsend and Reilly<sup>224</sup> and Ferguson and Smithers.<sup>225</sup> The toric unstable resonator possessed the basic advantages of a conventional unstable optical cavity, but also offered some desirable features. The design premise is to have the optical radiation walk from the outside of the resonator toward the center of the device rather than diffracting over the edge, as in a conventional unstable resonator design. This has the advantage of eliminating the large output window or optical compaction devices previously described. Additionally, this feature of the toric optical system lends itself to the symmetry of the multichannel laser structure investigated herein.

#### 4.2 Resonator Design

As was discussed in the previous section, the two fundamental resonator designs studied were the toric unstable and the conventional unstable resonators. Included in these two broad categories were several variations of these two resonators. The primary variation was the use of a confocal or a non-confocal resonator design. The principle difference between the two cases was that the confocal situation used mirrors that had a coincident focal point, and hence its name.

The traditional unstable resonator design that was used for these experiments is shown in Figure 4.2. The resonator consists of mirrors,  $M_1$  and  $M_2$ , separated by a distance  $L = 63$  cm. An optional beam compacting axicon is also shown in the figure. This axicon compacted the output beam into a smaller diameter profile but had no other affect on the optical properties of the system.

## Unstable Multi-Slot Resonator

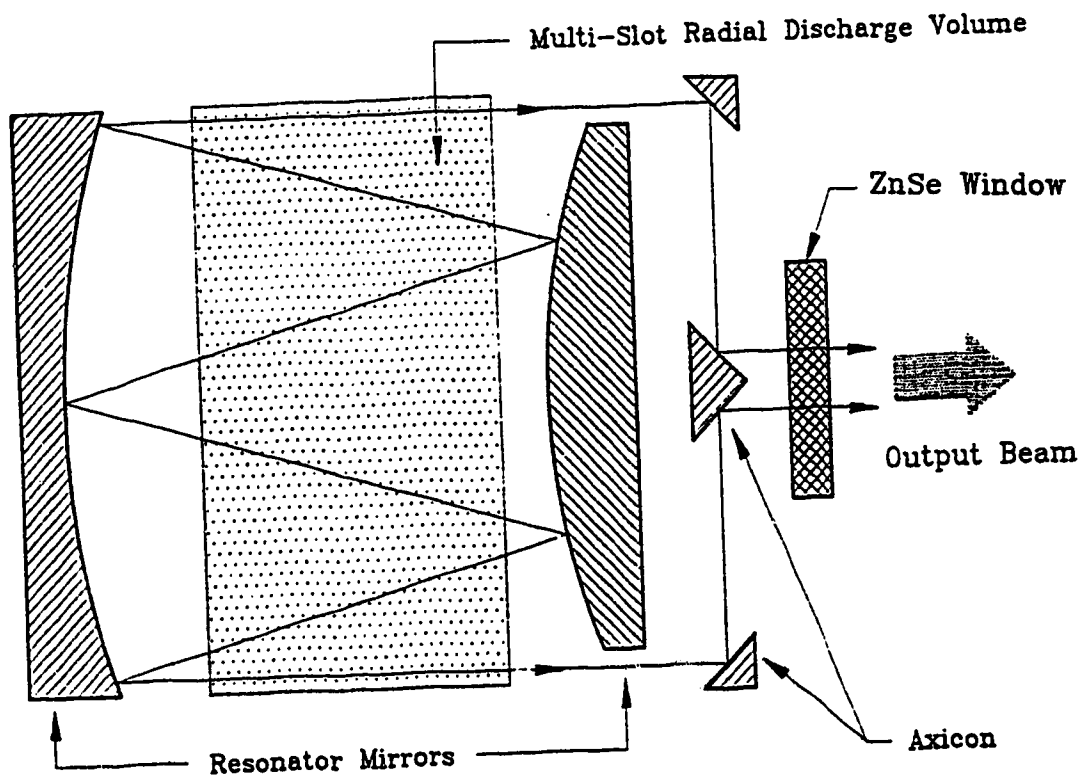


Figure 4.2 Conventional Unstable Resonator Schematic

Two versions of this resonator were studied. The first design was a positive branch confocal system having a magnification given by:

$$M = \frac{R_1}{R_2} \quad (4.3)$$

where  $R_1$  and  $R_2$  are the radii of curvature of the back concave mirror and the front convex mirror, respectively. The diameter of the back mirror for this resonator, and all of the other resonators used herein, was  $2a_1 = 11.6$  cm. This diameter was  $\approx 1$  cm larger than the discharge diameter and was chosen to allow for future phase-locking experiments. Several different diameters were used for the output mirror  $M_2$ . This was done in an effort to determine the output coupling characteristics of the various resonators. The diameters of these mirrors will be given as appropriate.

A second variation of the traditional unstable resonator was also investigated. It was designed to be non-confocal. The magnification for this type of single-ended cavity is given by:

$$M = m + \sqrt{m^2 - 1} \quad (4.4)$$

where

$$m = \frac{L + D}{2} = 2g_1g_2 - 1 \quad (4.5)$$

is the half trace of the usual ABCD matrix for a single-ended cavity.<sup>217</sup> Values for the radii of curvature,  $R_1$  and  $R_2$ , were chosen such that both confocal and non-confocal resonators had the same magnification.

The other category of resonators that was investigated was the unstable toric resonator. As discussed previously, the additional feature of the toric system was that the

output beam may be extracted near the centerline of the laser device. A schematic diagram of the basic toric resonator design is shown in Figure 4.3. Here, as in the previous case, a confocal and a non-confocal version were implemented. The radii of curvature of the mirrors were chosen, in both cases, to be the same as in the corresponding non-toric resonators described above.

It should be emphasized that the toric resonators used herein were initially designed as if they were conventional unstable resonators. The distinguishing aspect of the system only occurred during the actual physical fabrication of the mirrors. At this particular stage, the center of the radius of curvature of a conventional unstable resonator was taken to be at the outer edge of the toric mirror. Thus, in this type of resonator, the optic axis was actually a cylinder having a diameter equal to the diameter of the resonator mirrors. This diameter was equal to  $2a_1 = 11.6$  cm for this particular structure. The mirror surface extended slightly beyond the electrode, and hence the discharge cavity, by  $\approx 5$  mm. This feature was added to permit optical feedback experiments to be performed with this device. However, the region beyond the discharge cavity was not made into a flat surface, or a region of stability, as suggested by Townsend and Reilly.<sup>224</sup> Therefore, some energy may have been lost from the resonator by diffraction past the optic cylinder.

As with the conventional unstable resonators, various aperture sizes were used to couple optical radiation out of the cavity. It was found that the choice of this aperture had a profound influence on the characteristics of the output beam.

Table 4.1 gives a summary of the various resonators investigated in this study. Included in this table are the resonator type, magnification, corresponding mirror radii of curvature and the ideal geometrical output coupling fraction  $\delta$ . The output coupling was given by the familiar relation:<sup>199,217</sup>

$$\delta = 1 - \frac{1}{M^2} \quad (4.6)$$

and depends solely on the resonator magnification.

Table 4.1 Design Specifications for the Optical Resonator Systems

Resonator Type	Magnification	Radius of Curvature $R_1$ (m)	Radius of Curvature $R_2$ (m)	Output Coupling (%)
non-confocal	1.05	25.0698	-23.8760	9.30
non-confocal	1.09	25.0698	-22.7907	15.8
non-confocal	1.12	25.0698	-21.7998	20.3
non-confocal	1.16	25.0698	-20.0558	25.7
non-confocal	1.18	25.0698	-19.0283	28.2
non-confocal	1.20	25.0698	-18.5702	30.6
non-confocal	1.21	25.0698	-17.9070	31.7
non-confocal	1.24	25.0698	-16.7132	35.0
confocal	1.16	9.1547	-7.8947	25.7

## Toric Resonator Design

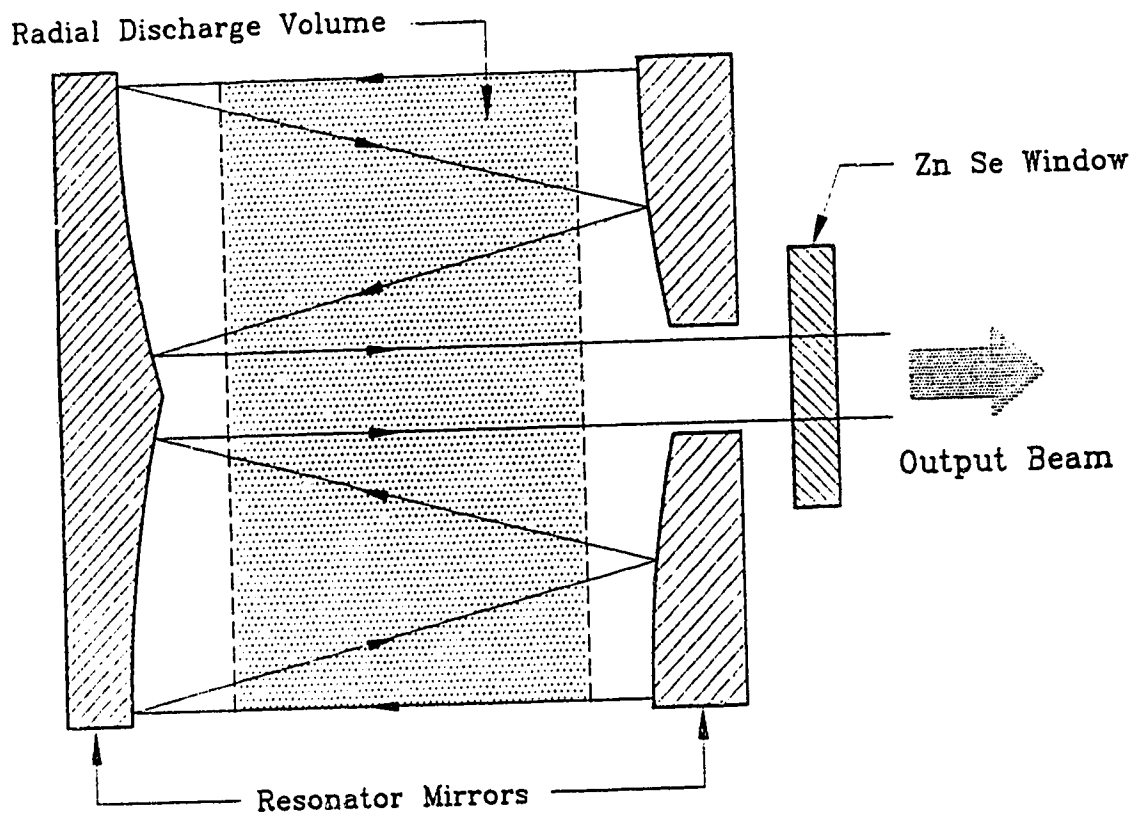


Figure 4.3 Toric Unstable Resonator Schematic

Mirrors were fabricated from an extruded Al-Cu-Ti alloy and diamond machined on a microsurface lathe. To minimize cost, these aluminium mirrors were left uncoated. As such they exhibited an optical absorption of  $\approx 2\%$ .<sup>226</sup> The units were water-cooled to minimize thermally induced surface figure distortion and misalignment. In all, approximately 100 mirrors were used to perform the experiments that are described in this chapter. One set, with gold surface coatings, was used to investigate the effects of reduced optical absorption on the output parameters.

#### 4.3 Resonator Parameter Characterization Techniques

In order to characterize the individual resonators described above, several output parameters were measured for each system. This section will briefly describe the methods and techniques employed that were common to all of the resonator designs.

For all of the optical extraction experiments, unless stated otherwise, a static gas mixture that consisted of 1:1:3 = CO<sub>2</sub>:N<sub>2</sub>:He at 15 Torr, combined with 2 kW of RF excitation, was used throughout the tests. No attempt was made to optimize either the gas mixture, the gas pressure, or the RF input power.

In order to assess the effect of varying the output coupling aperture or the resonator magnification, a series of output power tests was undertaken. These output power measurements were conducted with the aid of a Coherent model 201 water-cooled power meter. For those resonators which possessed an output beam diameter larger than the power meter aperture, the beam was first focused with an 8.89 cm diameter, 25 cm focal length, ZnSe lens. The absorption of this antireflection coated ZnSe lens at 10.6  $\mu\text{m}$  was less than a fraction of one percent<sup>227</sup> and therefore did not affect the observed power reading. The few output beams that were still larger than the clear aperture of the ZnSe lens were first reduced in size via the beam compacting axicon, as shown in Figure 4.2. Tests with this axicon in place, and removed, indicated that the axicon produced a 9% reduction in total output power. All values of output power reported in this thesis are the corrected values.

In an effort to further characterize the output from the various resonators, the two-dimensional and three-dimensional intensity profiles of the near-field optical output were taken. These profiles were derived by using a computer-based image analysis device, which was developed recently in our laboratory.<sup>228,229</sup> In this approach, the output beam was imaged onto a thermally sensitive screen that fluoresced when illuminated by ultraviolet light. When heated by a laser beam, the fluorescence of that portion of the screen was quenched in direct proportion to the intensity of the heating. In this manner, an image of the beam's intensity profile was formed upon the screen. This image was then recorded with a standard color video camera, digitized using a Live 2000 frame grabber, and finally analyzed using an Amiga 2000 computer.

The far-field properties of the various resonators were also investigated. This involved passing the output beam through the 25 cm focal length ZnSe lens and then measuring the focal spot size. A BeamScan model LBA 1/A rotating wire beam analyzer was employed to facilitate the analysis. This device uses fast pyroelectric detectors to measure the intensity of radiation scattered from a wire which rotates through the laser beam.<sup>230,231</sup> In theory, it was possible to measure intensity profile information with the wire beam analyzer. However, it was much more cumbersome and time consuming than the above-described image analysis. For all of these measurements, the beam analyzer was mounted on an optical bench and adjusted in all three directions to find the minimum focal spot size.

Alignment sensitivity is another parameter of major importance to the laser user, and therefore it was also prudent to explore this quantity. By definition, the angular sensitivity  $S$  is a measure of how much misalignment a resonator can withstand before a significant reduction in its output performance is observed. In practice, this usually corresponds to the condition that the oscillating cavity axis coincides with the edge of the opposite mirror. An equivalent criterion is achieved when the observed output power has been reduced by  $\approx 50\%$ .<sup>220</sup> Krupke and Sooy<sup>200</sup> presented a theoretical analysis to help quantify this important parameter. Their analysis revealed that the sensitivity depends on several resonator characteristics, such as the mirror diameter, radii of curvature, and the resonator length.



Their formulation is characterized by the S parameter, which is defined as:

$$S = \frac{1 - g_i}{1 - g_i g_j} \quad (4.7)$$

where the  $g_i$  are given by equation (4.1). Equation (4.7) thus gives a relative measure of the alignment sensitivity. In this context, larger values of S indicate a more sensitive alignment arrangement.

The criterion used herein to evaluate the misalignment sensitivity was that the output radiation decreased to 50 % of its best aligned value. Knowing the distance of the alignment screw to the pivot point of the mirror, and the tilt that was required to effect this condition, allowed the angular deviation to be calculated. In this case, the distance to the alignment screw was 11.4 cm and the screw had 14 threads/cm. Therefore, measurement of the number of turns of the alignment screw that were needed to reduce the output to one half of its best value provided the misalignment angle.

Finally, it has been well documented in the scientific literature that the polarization state of a laser's output beam can profoundly influence a laser-material processing interaction.<sup>232</sup> This is especially true for applications such as cutting, scribing, and drilling.<sup>233,234</sup> This being the case, the polarization properties of the various resonators were also investigated. In order to perform these measurements, a ZnSe wire grid polarizer was inserted between the output of the laser and a power meter. Rotation of the polarizer, in conjunction with power readings, thereby allowed a determination of output beam polarization.

#### **4.4 Resonator Output Characteristics**

The following sections will give a detailed description of the various output properties described above for the various resonators investigated in this study. One attribute that was found to be common to all resonators was that the output radiation predominately corresponded to the P(20) transition of the CO<sub>2</sub> molecule at 10.6 μm. This was determined

by directing the output beam into an Optical Engineering CO<sub>2</sub> Laser Spectrum Analyzer. Occasionally, other transitions would also be present but it was found that these were caused by a slight maladjustment of the optical resonator.

#### 4.4.1 Toric Non-Confocal Resonator

One of the most interesting aspects of this resonator was how the character of the output beam could be varied by a change in the output aperture of the convex mirror  $M_1$ . Figures 4.4 and 4.5 show typical near-field output patterns obtained under identical operating conditions, except for two different aperture sizes. Both patterns were for a geometrical magnification of 1.16. Figure 4.4 is for a 3.18 cm aperture in the convex mirror, whereas Figure 4.5 is for a 1.27 cm aperture. Both of these near-field patterns were obtained  $\approx 55$  cm from the ZnSe output window by imaging the output beams with a ceramic board. The transition from the individual beams that were present in Figure 4.4 to a single beam in Figure 4.5 is immediately evident. The eight beamlets, one from each of the inter-electrode regions, have overlapped completely to produce a single output beam.

Figures 4.6 and 4.7 show the corresponding near-field intensity profiles that were obtained with each of the apertures discussed above. These profiles were derived using the techniques outlined in the previous section. As is clear from Figure 4.6 each of the individual beamlets that were obtained from the larger 3.18 cm aperture have a similar structure and amplitude. This fact is documented further in Figure 4.8, which is a cross-sectional view through the xz-plane of the intensity profile given in Figure 4.6. In contrast, Figures 4.7 and 4.9 are the corresponding near-field intensity profiles obtained with the 1.27 cm aperture. It is evident that the profile of the beam from the 1.27 cm aperture has coalesced to fill in the available aperture area completely. This resulting single beam was approximately twice as broad but occupied a smaller area than did the corresponding multiple beamlets from the 3.18 cm aperture.

In an effort to characterize the output parameters in more detail, the  $1/e^2$  focal spot sizes were also measured. This data was collected at a constant magnification of  $M = 1.16$ ,

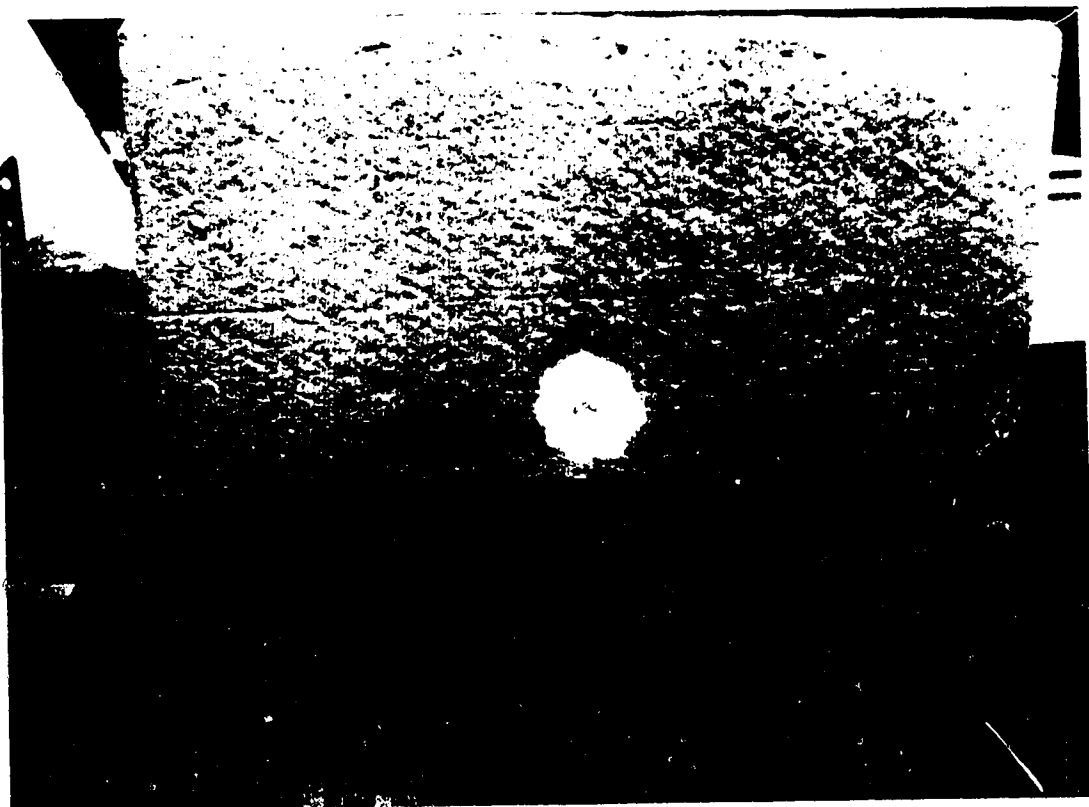


Figure 4.4 Near-field Beam Pattern for a Toric Non-Confocal Resonator with  $M = 1.16$  and a 3.18 cm Aperture

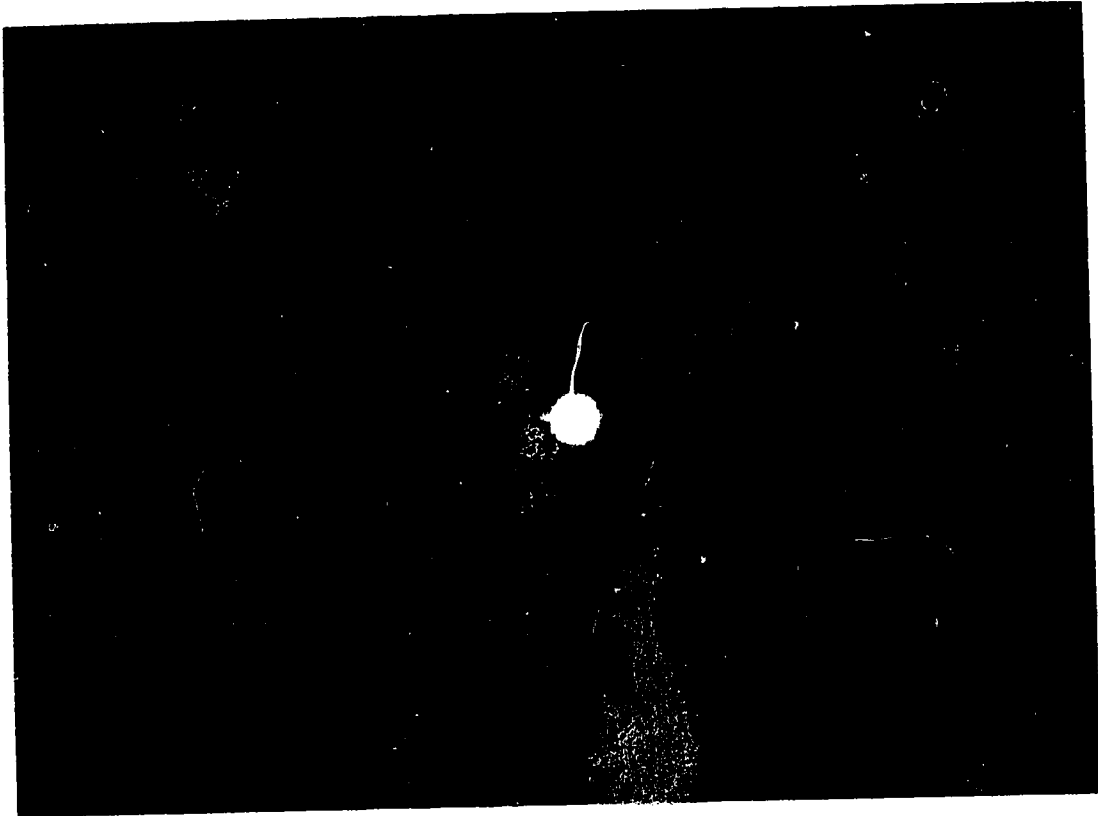


Figure 4.5 Near-field Beam Pattern for a Toric Non-Confocal Resonator with  $M = 1.16$  and a 1.27 cm Aperture

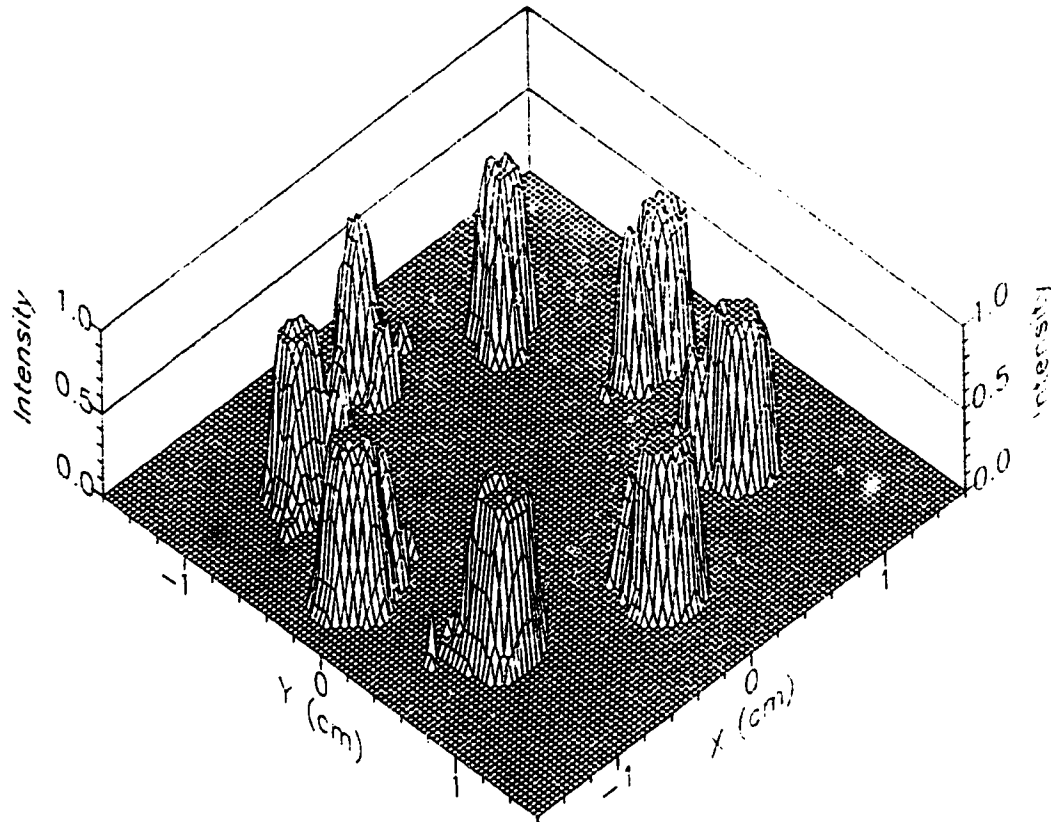


Figure 4.6 3-D Near-field Intensity Profile for a Toric Non-Confocal Resonator with  $M = 1.16$  and a 3.18 cm Aperture

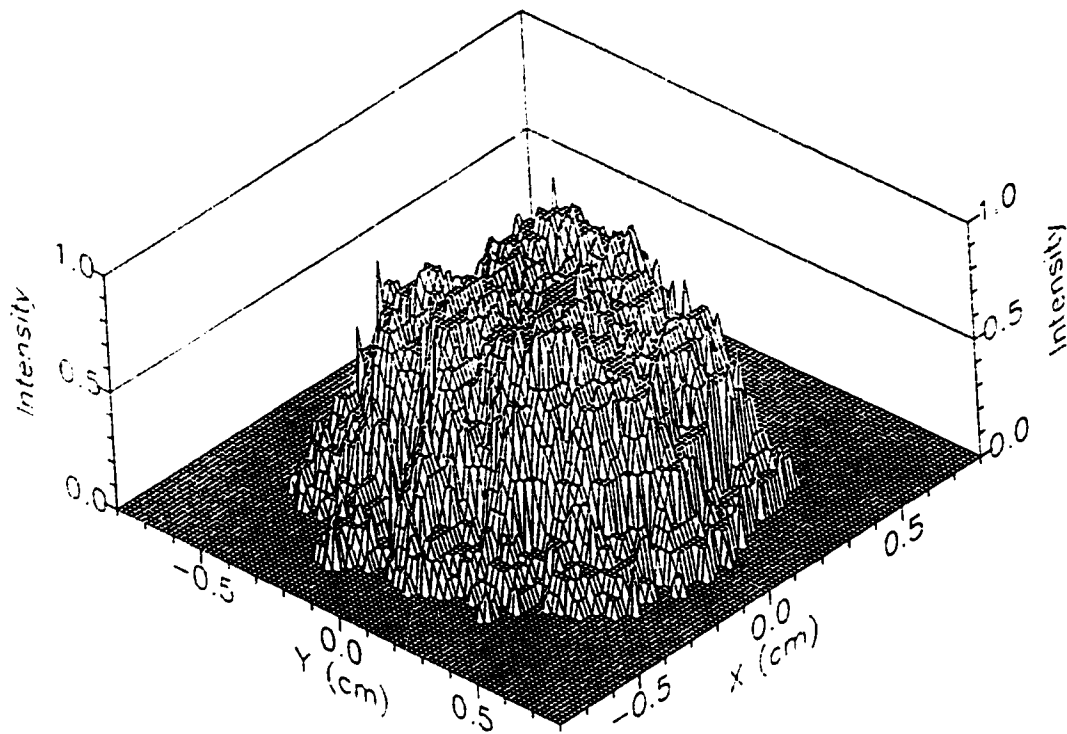


Figure 4.7 3-D Near-field Intensity Profile for a Toric Non-Confocal Resonator with  $M = 1.16$  and a 1.27 cm Aperture

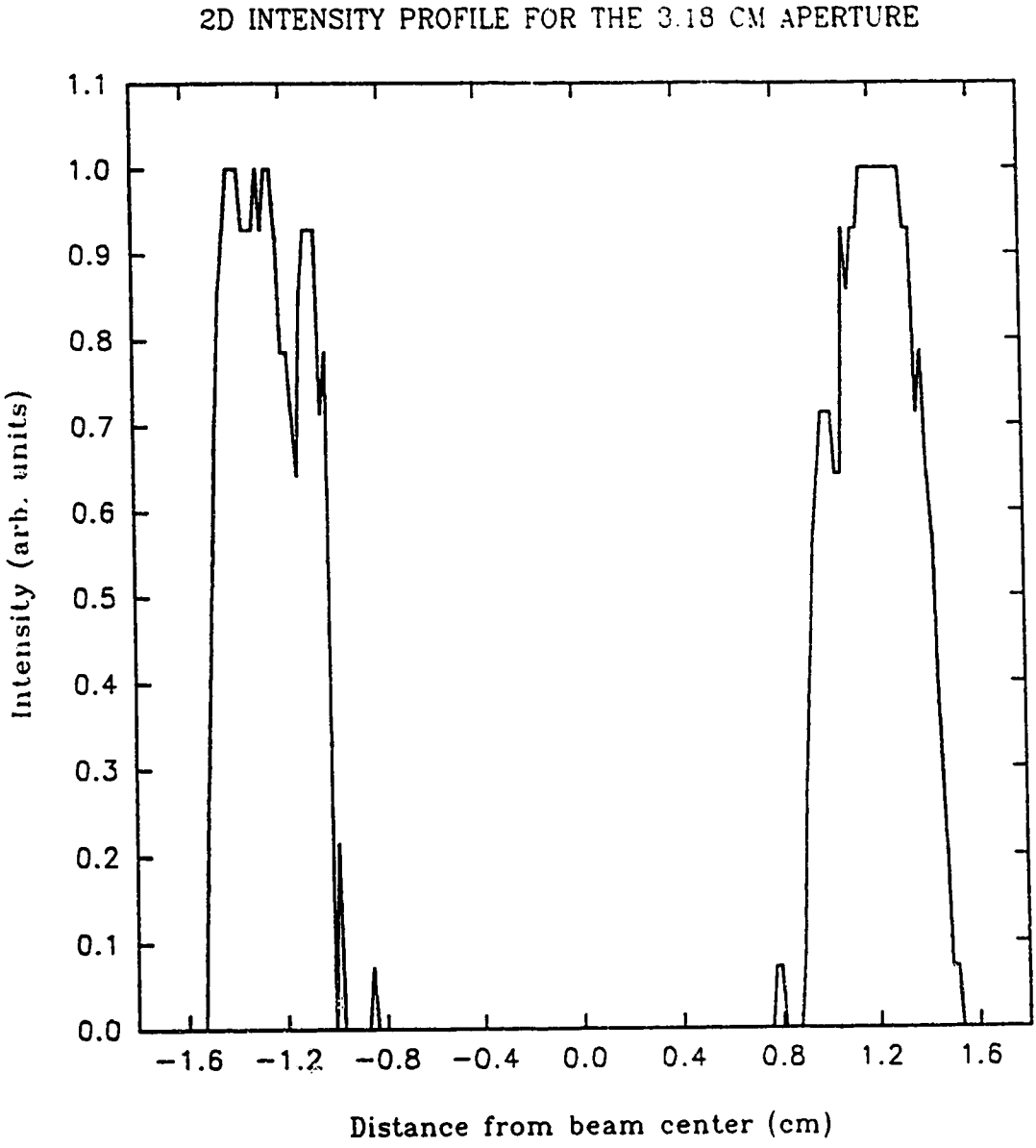


Figure 4.8 2-D Near-field Intensity Profile for a Toric Non-Confoal Resonator with  $M = 1.16$  and a 3.18 cm Aperture

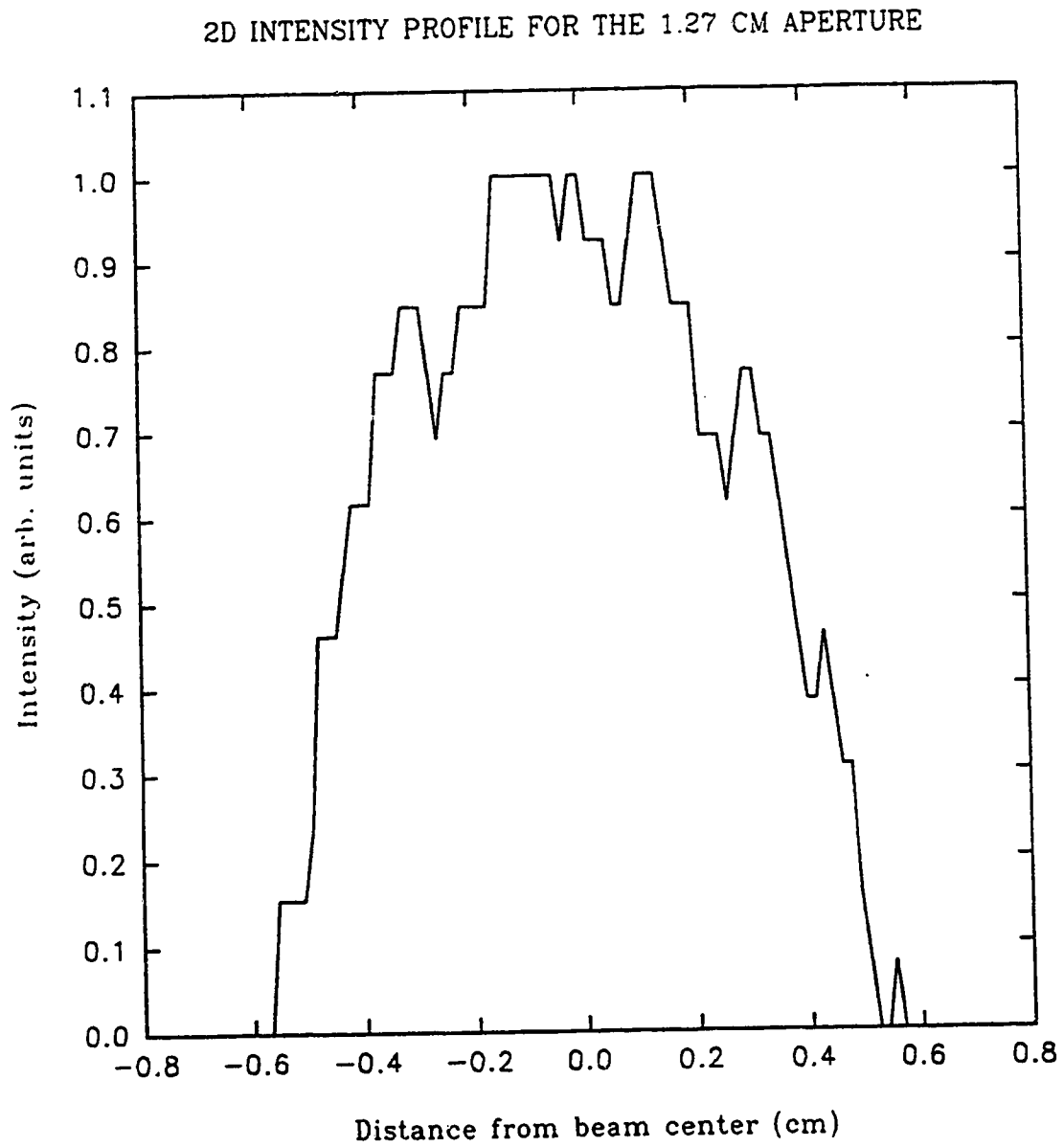


Figure 4.9 2-D Near-field Intensity Profile for a Toric Non-Confocal Resonator with  $M = 1.16$  and a 1.27 cm Aperture



and the results of this investigation are presented in Figures 4.10 and 4.11. Figure 4.10 shows a typical far-field beam pattern obtained with a 3.18 cm aperture. This picture was obtained by placing a Perspex rod at the focal point of a 25 cm ZnSe lens and then permitting the beam to penetrate the material for a brief period. As may be seen, the focused beam is clean and exhibits a strong central peak with little or no energy contained in the sidelobes, which is usually referred to as  $TEM_{00}$  in nature.

Figure 4.11 illustrates the dependence of the focal spot size on the coupling aperture size. It was interesting to note that there appeared to be three different regimes of operation as the aperture was increased. The first regime was for apertures that were between 0.95 and 1.78 cm [points to the left of line (a)]. They were characterized by a steep slope. This was the regime in which the output emerged as a single beam. The second part of the graph, for an aperture size of 2.16 - 2.54 cm [between lines (a) and (b)], was characterized by a transition region where the inner portion of the beamlets overlap but their outer edges were still distinctly separate. Finally, the third regime, for apertures between 2.92 and 3.56 cm [all points to the right of line (b)], featured the condition of eight distinct output beams. This portion was distinguished by a considerably flatter slope. It should also be noted that, in the two extreme conditions, the focal spot size varied inversely with the aperture, as was expected from standard diffraction theory.<sup>235</sup> To the left of line (a) the steep slope was indicative of the limiting size of the aperture. To the right of line (b) the essentially flat slope indicated a constant effective aperture where the beams did not interact at all. Furthermore, the focal spot size of one single channel was found to be similar to that of all eight channels acting simultaneously, irrespective of the aperture size. Had the individual beamlets been coherently phase-locked together, a much sharper peak in the intensity profile or a correspondingly smaller focal spot size, which was in direct proportion to  $N^2$ , where  $N$  was the number of individual sources in the array, should have been exhibited.<sup>127</sup> This property, as well as other phase-locking characteristics, will be discussed more fully in the next chapter. The triangles in Figure 4.11 correspond to the calculated theoretical diffraction-limited spot size for the representative single beam and individual beamlet cases.<sup>235</sup>

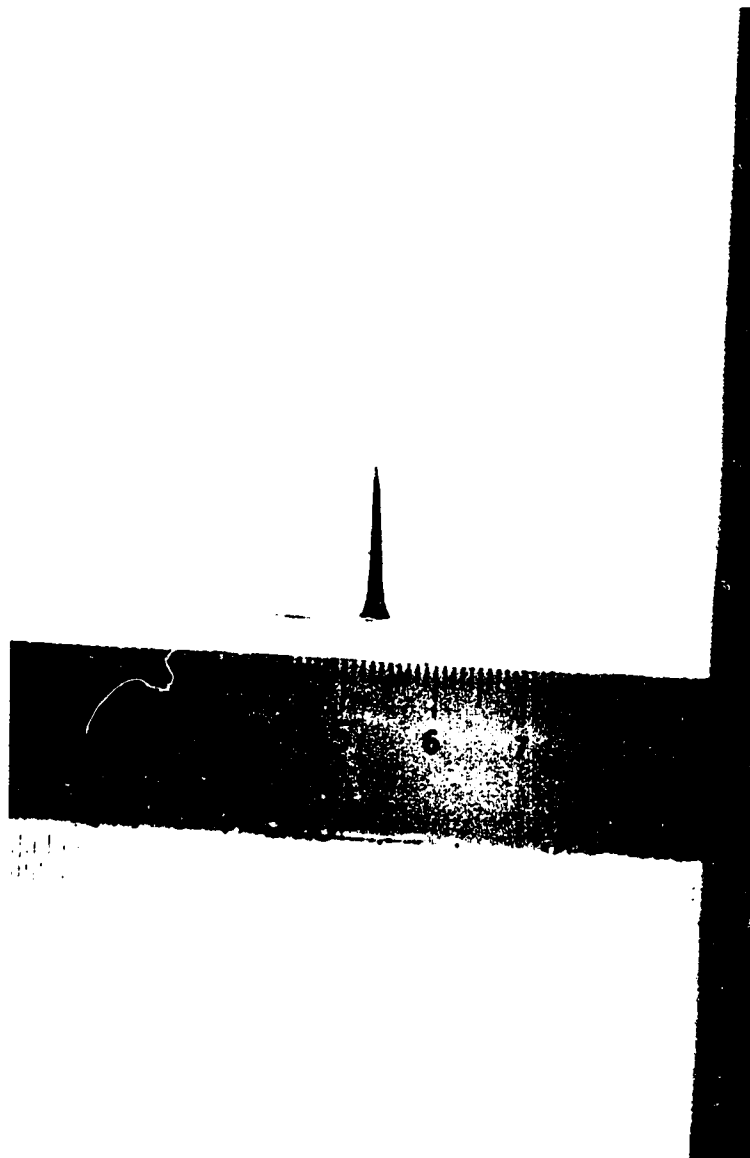


Figure 4.10 Typical Far-field Burn Pattern in Perspex for a Toric Non-Confocal Resonator with  $M = 1.16$  and a 3.18 cm Aperture

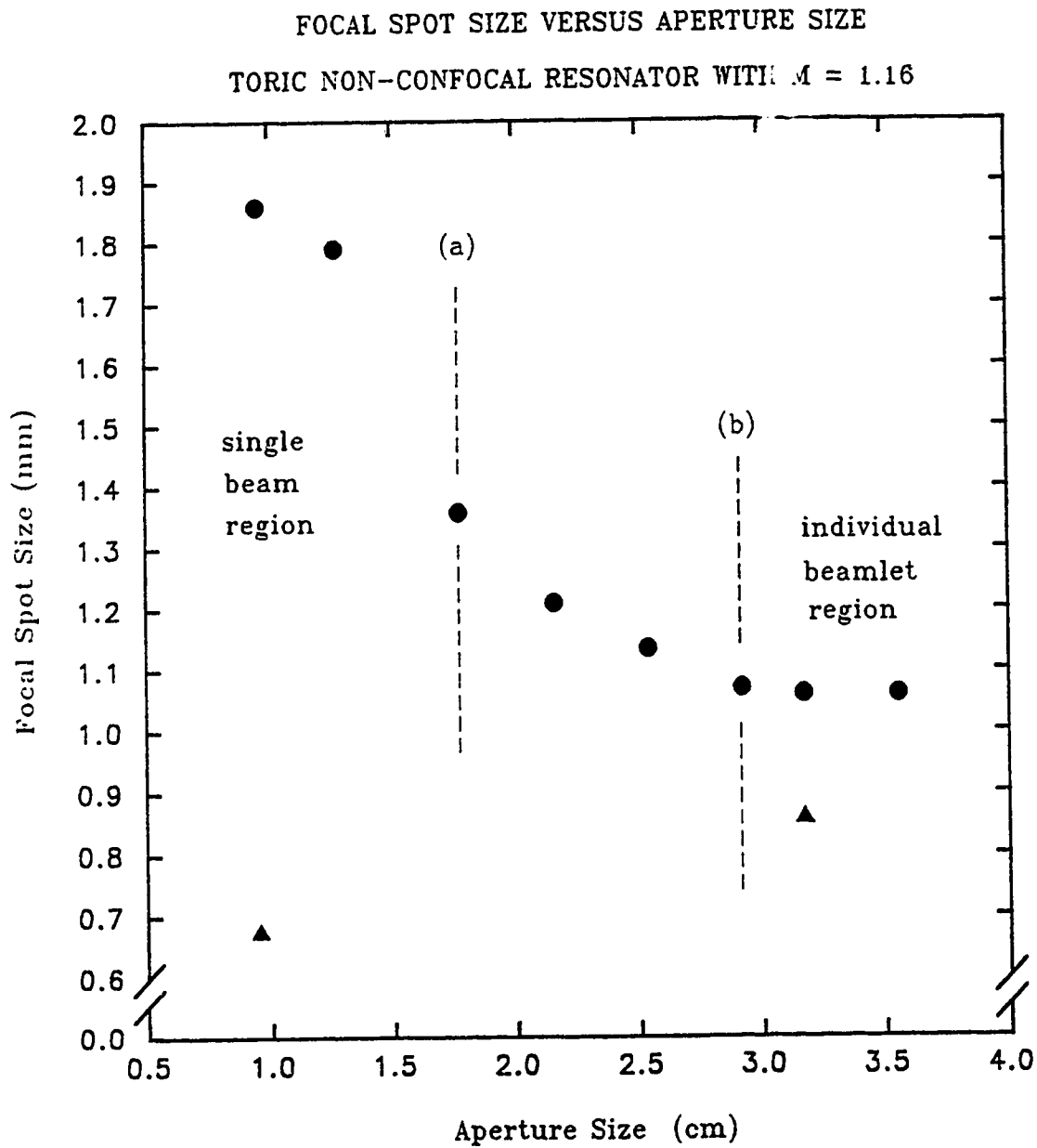


Figure 4.11 Variation of  $1/e^2$  Focal Spot Size with Aperture Size for a Toric Non-Confocal Resonator with  $M = 1.16$

A series of experiments has also been performed to determine the effect of the convex mirror aperture on the output power achievable from the device. The magnification of the resonator was also varied to determine its influence on system behaviour. Figures 4.12 - 4.14 show the results of this study for three representative magnifications over a broad range of aperture sizes. These apertures correspond to coupling factors  $\delta^*$  ranging from 9 % for the smallest aperture to 34 % for the largest. This range spans the regime in which near-ideal geometrical output coupling should be experienced. The ideal output coupling factors  $\delta$  were given in Table 4.1 for the various resonators. These values depend solely on the resonator magnification. It should be emphasized that the above values of  $\delta^*$  are the actual values of output coupling calculated as the ratio of the aperture radius in the secondary mirror to the total radius of the discharge region, which is a value that is independent of the resonator magnification.

It is clear that all the curves follow the same general trend; that is, each shows a peak in the output power for apertures in the 2.5 - 3.0 cm range. These particular apertures correspond to a 24 and a 29 % output coupling fraction  $\delta^*$ , respectively. With the exception of the  $M = 1.12$  case, the peak in the output power was consistent with predictions of the geometrical theory that was mentioned above. For this particular magnification, an ideal output coupling fraction of  $\delta = 20$  % was predicted. This calculation presumed that there was a uniform gain medium present over the entire cross-section of the secondary mirror. However, as was documented in Chapter 3, this was not the situation for the particular system in question here. Because of the geometry of the structure, there was a central zone in which no discharge was present. The gain that was found in this region was due solely to the diffusion of vibrationally-excited species into that area, and was roughly 25 % of the gain coefficient found in the inter-electrode regions. Hence, the region exhibited a higher absorption and a concomitant decrease in the output power than would otherwise have been the case. Consequently, the optimum output aperture for  $M = 1.12$  was shifted toward a larger size, which made better use of the gain available within the region.

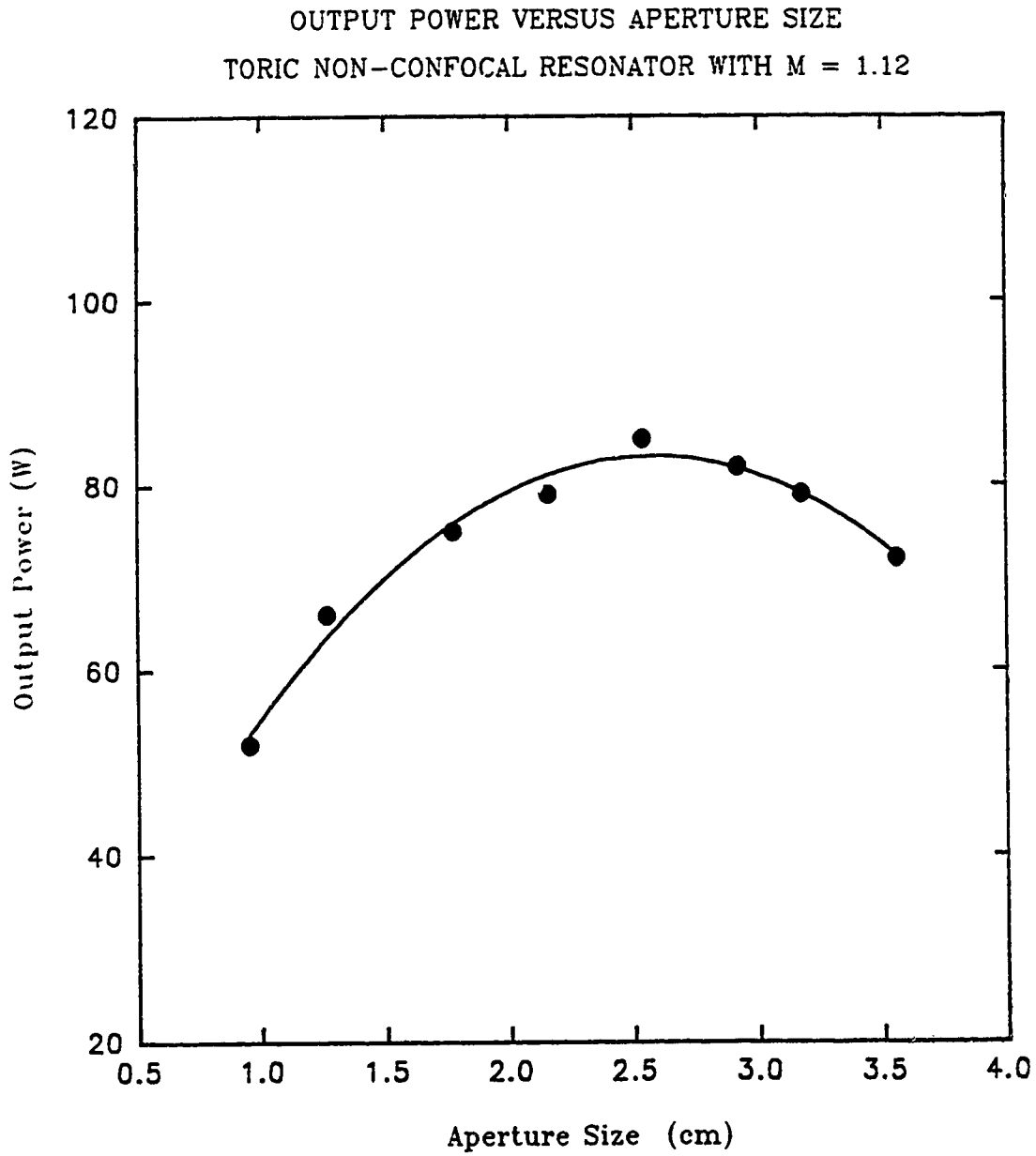


Figure 4.12 Variation of Output Power with Aperture Size for a Toric Non-Confocal Resonator with  $M = 1.12$

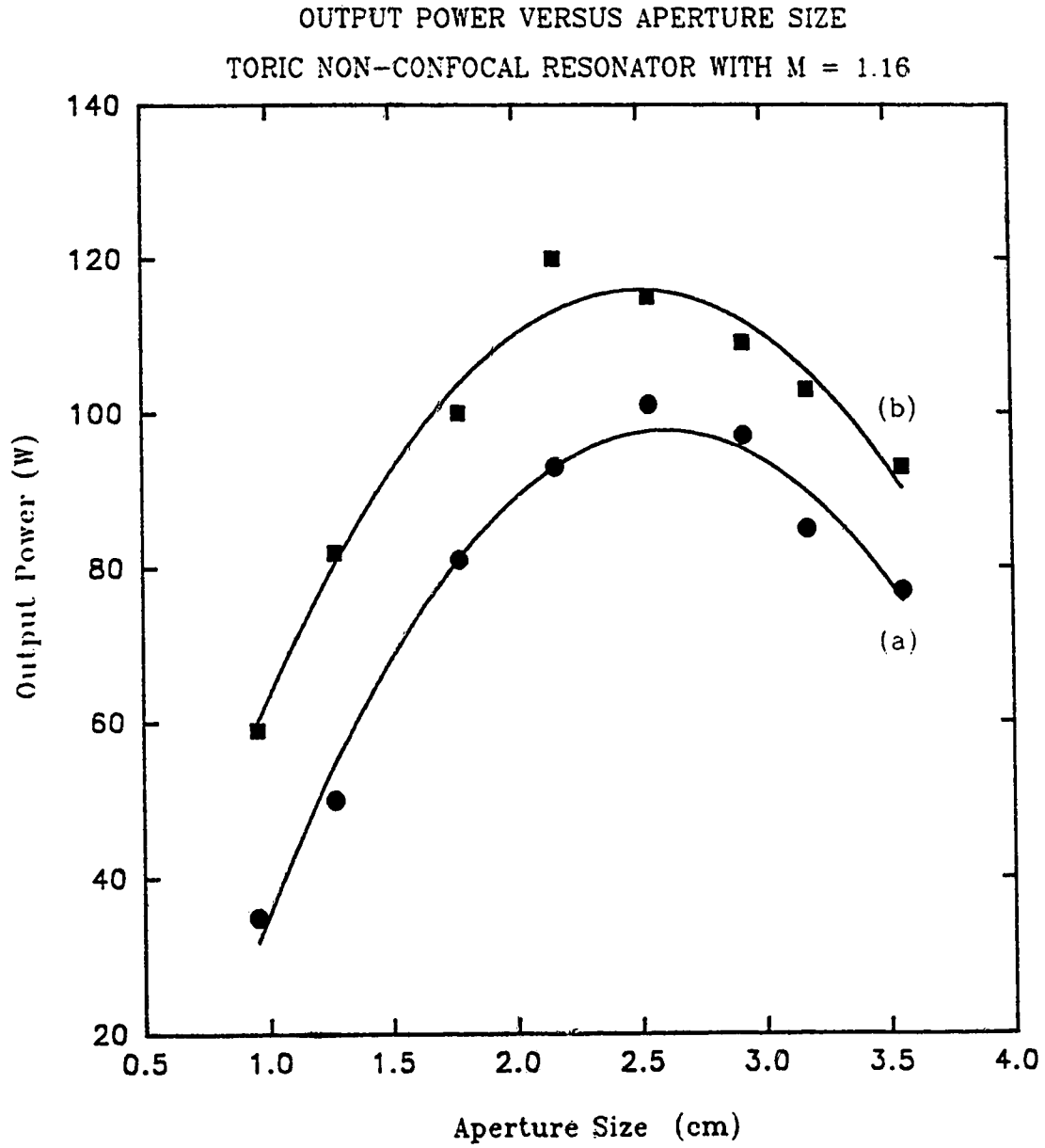


Figure 4.13 Variation of Output Power with Aperture Size for a Toric Non-Confocal Resonator with  $M = 1.16$

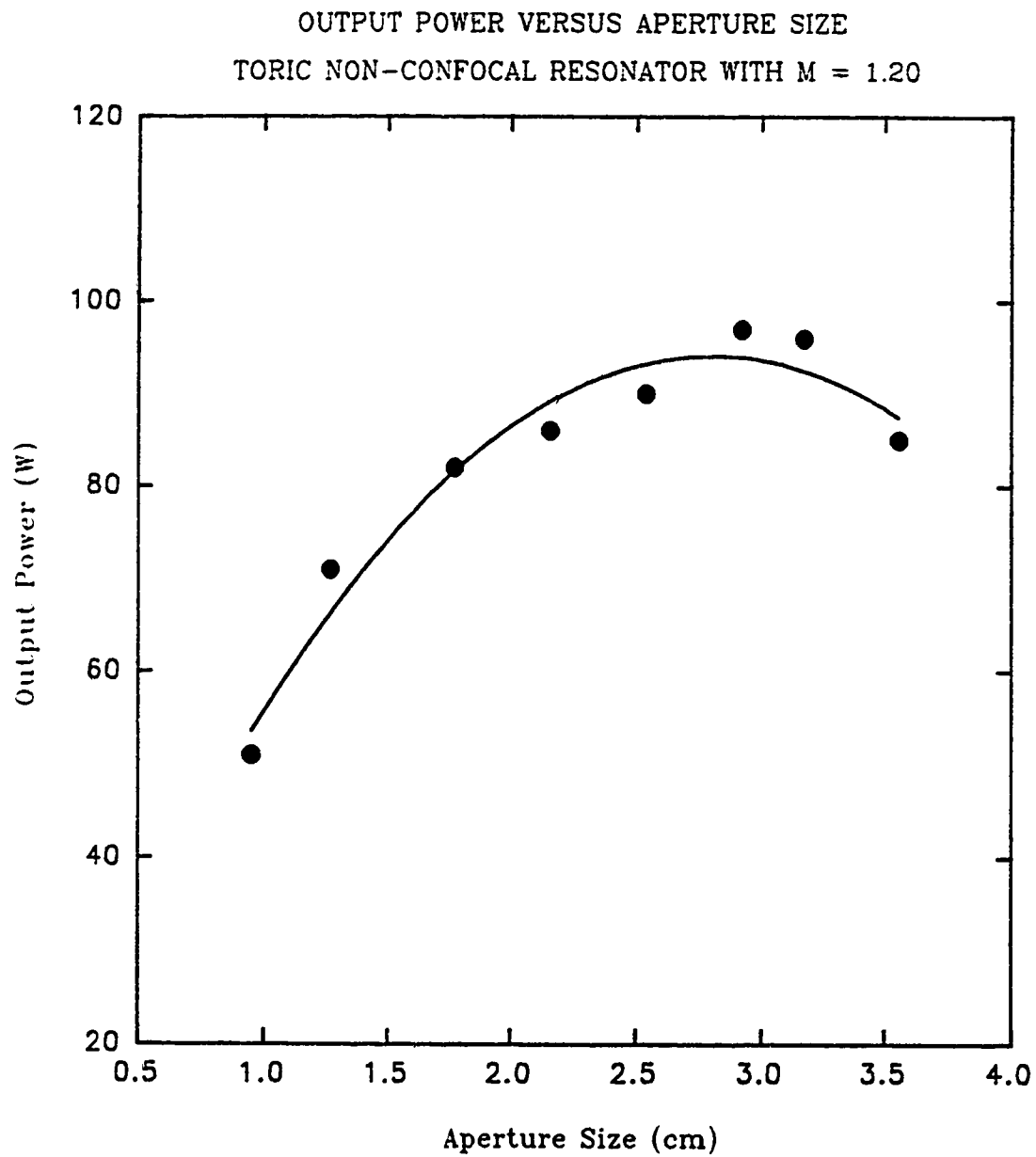


Figure 4.14 Variation of Output Power with Aperture Size for a Toric Non-Confocal Resonator with  $M = 1.20$

In addition to the data for the uncoated aluminium alloy mirrors, Figure 4.13 curve (b), also shows the data that was obtained with gold-coated mirror surfaces. These experiments were performed to evaluate the impact of a reduced mirror surface absorption on the output power and coupling characteristics. As is evident, the gold-coated mirrors showed an increase in the attainable optical power of approximately 20 % and a slight shift of  $\approx 5$  % in the optimum aperture size. Both of these findings were borne out by an analysis presented by Kaufman and Oppenheim.<sup>236</sup> Their analysis was based on the well-known Rigrod formulation but applied to a higher gain system. By using previously measured gain values of  $0.77 \text{ m}^{-1}$ , a saturation intensity of  $995 \text{ W/cm}^2$  together with the  $10.6 \text{ }\mu\text{m}$  reflectivities for uncoated aluminium mirrors of 98 %, as well as that of gold-coated mirrors of 99.4 %<sup>226</sup>, a shift in the optimum output coupling value of near 3.5 % was predicted. In addition, an increase of  $\approx 18$  % in the overall output power was projected. These results were a consequence only of the change in mirror reflectivity; all other factors were held constant. It is clear that these theoretical predictions agree well with the experimental findings reported here.

It was further observed that when the individual beamlets coalesced to fill in the near-field output profile completely, the power decreased to  $\approx 80$  % of its maximum value. This situation occurred with the 1.27, 1.78 and 1.78 cm apertures for magnifications of 1.12, 1.16 and 1.20, respectively. Considering that for the individual beamlets to overlap they must traverse a region of the resonator that contained a reduced gain coefficient, these findings are not unexpected. A second plausible explanation for the power decrease is related to the aperture size in the convex mirror as well as the beam size in each individual channel. For any given magnification, there was a corresponding beam size associated with it. Hence, if the aperture that was selected was smaller than the beam, a portion of the beam may have been reflected past the central tip of the primary concave mirror, and thereby lost into the opposite gain cell. This situation occurred for any aperture that was smaller than 1.13, 1.45 and 1.76 cm for magnifications of 1.12, 1.16 and 1.20, respectively. In spite of this, however, a large penalty in output power was not observed despite the selection to operate with only a single beam instead of eight individual beamlets.



It is observed from Figures 4.12 - 4.14 that the maximum output power that was obtained was not constant but depended on the particular resonator magnification used. To investigate this phenomenon further, a series of experiments were performed in which the maximum output power was measured as a function of the geometrical magnification. Figure 4.15 presents the data for a range of magnifications from  $M = 1.09$  to 1.24. For each point on the graph, a series of different aperture sizes were used to determine which provided optimum coupling. This aperture was then used to measure the output power that is shown in the figure. The curve exhibits a broad peak near a magnification of 1.18. This was in relatively good agreement with results obtained from Chernin's resonator design analysis which predicted an optimum magnification value of 1.15 for this laser structure.<sup>218</sup>

For values of  $M$  below this peak the optical radiation makes a larger number of passes through the gain medium. However, the effect of these increased passes was offset by the concurrent losses that were accumulated through mirror absorption. Therefore, any power gains that were made within the active medium were more than negated by internal cavity losses.<sup>217</sup> Hence the observed maximum output power decreased. Of equal importance was the reduced value of gain in the central region. Thus, as explained previously for the  $M = 1.09$  and 1.12 cases, the peak in the output power was shifted to a higher value of output coupling than the ideal prediction. The reduction in maximum power that was observed at lower magnifications may be due to similar reasons. Conversely, for values of  $M$  that are larger than 1.18, the photons make fewer passes in the gain medium. Thus, full advantage of the energy stored therein was not experienced. Consequently, the output power decreased for magnifications beyond  $\approx 1.18$ .

An investigation of the non-confocal toric resonator alignment sensitivity was also undertaken. For comparison, the sensitivities of the  $M = 1.09$ , 1.16 and 1.24 resonators were measured. Analytically these three situations correspond to  $S$  values of 15.2, 5.99 and 3.24, respectively, where the  $S$  parameter has been calculated via equation (4.7). As discussed in the previous section, the 50 % reduction in optimum output power criterion was adopted herein to determine alignment tolerances. Following this approach, a deviation of 42  $\mu$  was found for

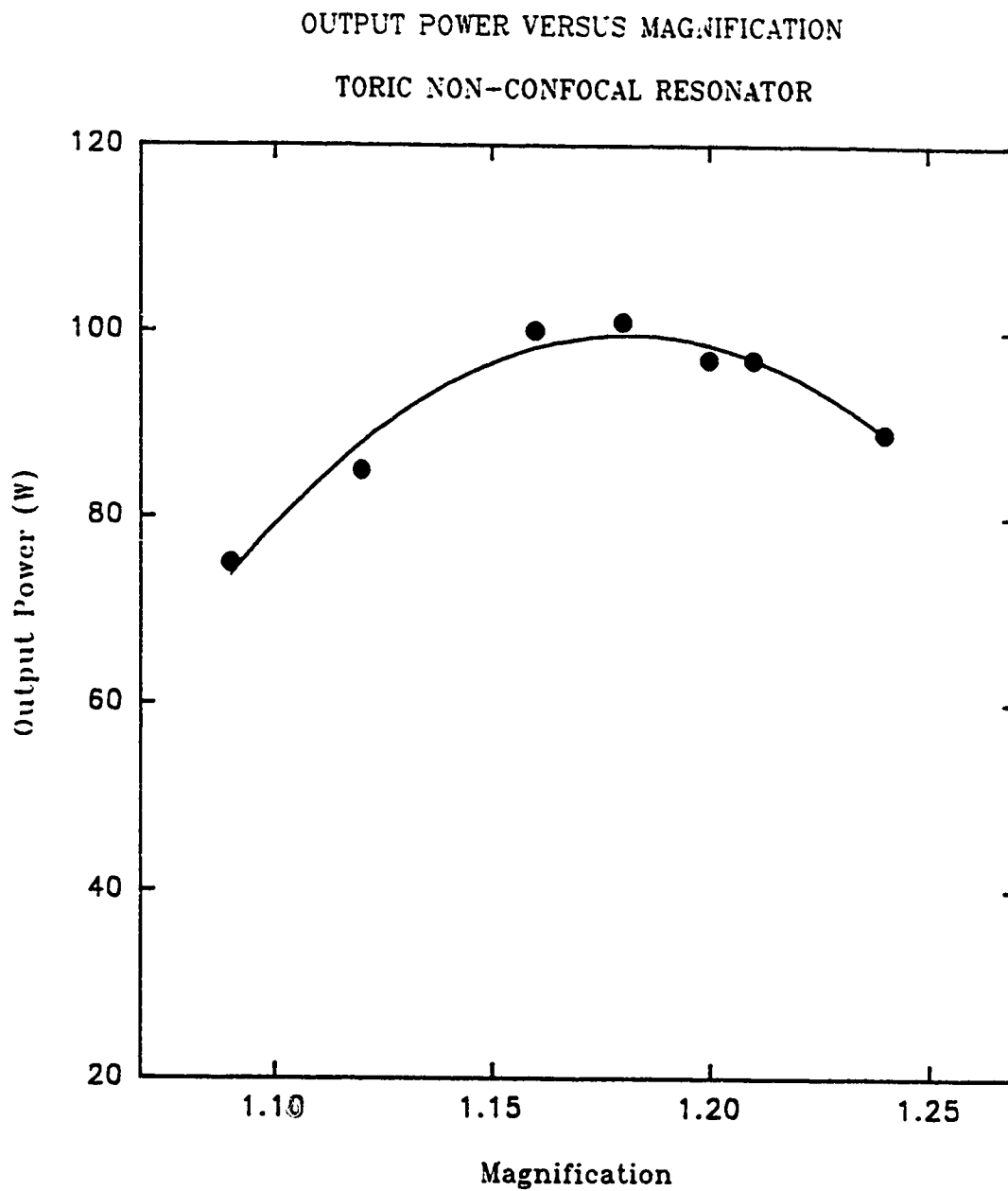


Figure 4.15 Variation of Output Power with Magnification for a Toric Non-Confoocal Resonator

the  $M = 1.09$  case, 83 s for the  $M = 1.16$  situation, and a value of 141 s for the  $M = 1.20$  resonator. These values are in qualitative agreement with Krupke and Sooy. It should also be mentioned that, in general, the resonator became more sensitive to misalignment as the magnification decreased. In fact, for a value of  $M = 1.05$  ( $S = 44.5$ ), the resonator was so sensitive that a stable condition with all eight beams lasing simultaneously was not achievable.

Also noteworthy was the appearance of the output beams during misalignment. It was evident that the beam began to take on a crescent shape or became lopsided as the resonator was misaligned. This was in agreement with the hypothesis of Townsend and Reilly.<sup>224</sup> However, their prediction of a hole forming in the output beam during a misalignment could not be confirmed, since the aperture size that was used during these experiments already contained eight individual beamlets.

Because of the unique features of the toric resonators that were outlined previously, polarization measurements were made for both the single-beam output and the eight individual beamlet configurations. Figure 4.16 shows the polarization state that was observed when all eight distinct beamlets were present: It is evident that each channel was linearly polarized in a direction that was parallel to its electrode faces. Although this result is typical of many RF excited waveguide CO<sub>2</sub> lasers<sup>237</sup>, it was not anticipated here. In particular, tests have been performed in which the electrode faces were made rough to determine if waveguiding effects were important. These studies indicated that the lasing performance of the system was not hampered by the roughness of the electrode faces, and that the polarization orientation was also unaffected. Therefore, it was concluded that waveguiding effects are minimal.

The polarization state of the beam that emerges from the 1.27 cm aperture is more difficult to explain. Measurements that were performed with this aperture indicated that there was no preferential direction of polarization of the beam as a whole. In particular, the electric field exiting the test polarizer exhibited an equal amplitude for all polarizer orientations. It was believed that this particular condition resulted from the superposition of the individual polarizations that exist within each slot.<sup>238</sup> This hypothesis was confirmed by observing the

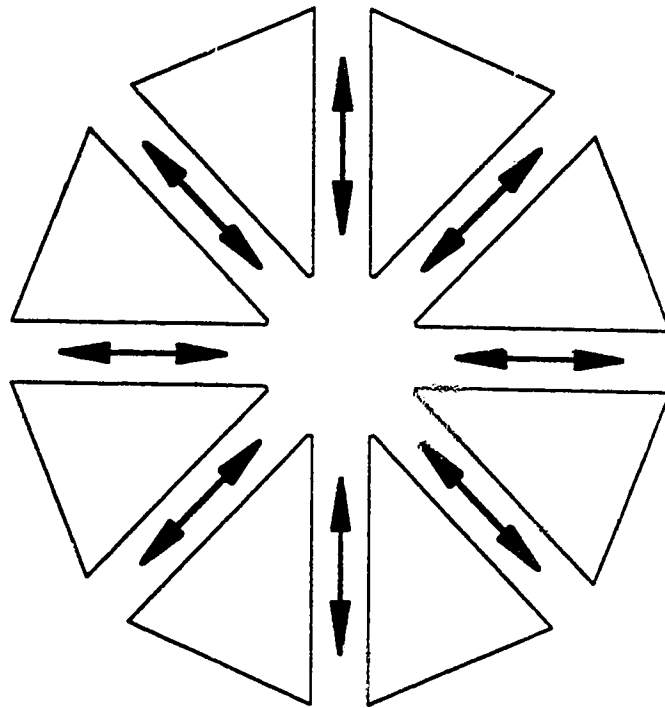


Figure 4.16 Schematic Representation of the Output Beam Polarization for the Toric Non-Confocal Resonator with a 3.18 cm Aperture

polarization at a point, which although dominated by a single beamlet, still contained contributions from the other channels. This was accomplished with a slightly larger aperture size. Although an intensity maximum in the direction corresponding to the slot geometry was measured, a uniform background intensity at all other polarization angles was also apparent. Similar patterns were also detected with the remaining seven channels as well.

#### **4.4.2 Toric Confocal Resonator**

A series of experiments were also performed using a toric confocal resonator. However, these tests were not as extensive as those with the non-confocal resonator. For these investigations, only one value of magnification was used, 1.16.

The general appearance of the output beam from the confocal resonator was very similar to that of the equivalent non-confocal system, until a critical output aperture size was reached. At any aperture size of 2.16 cm or less, the output beam was a complete annulus. This is shown in Figure 4.17. Further studies of the phenomenon included capturing the three-dimensional and two-dimensional intensity profiles for the 1.78 cm aperture. These two profiles are depicted in Figures 4.18 and 4.19, respectively. As is evident from these profiles, the toric confocal resonator produced a uniform annulus having no output at the center of the profile. This was in contrast to the output from the equivalent non-confocal case, which was shown in Figures 4.5, 4.7 and 4.9, which clearly indicated a gaussian-shaped profile that completely covered the output aperture.

The differences in the output profiles may be explained by the differences in the radii of curvature of the resonator mirrors. The confocal case produced a collimated output beam and hence an annular shape was expected. However, the toric non-confocal configuration had much larger radius of curvature mirrors. The back mirror had a larger radius of curvature than the front mirror, hence it had a focal point beyond that of the front mirror. Therefore, the back mirror radius could not entirely compensate for the diverging reflection from the front mirror. Consequently, the output beam filled in the central region of the aperture.

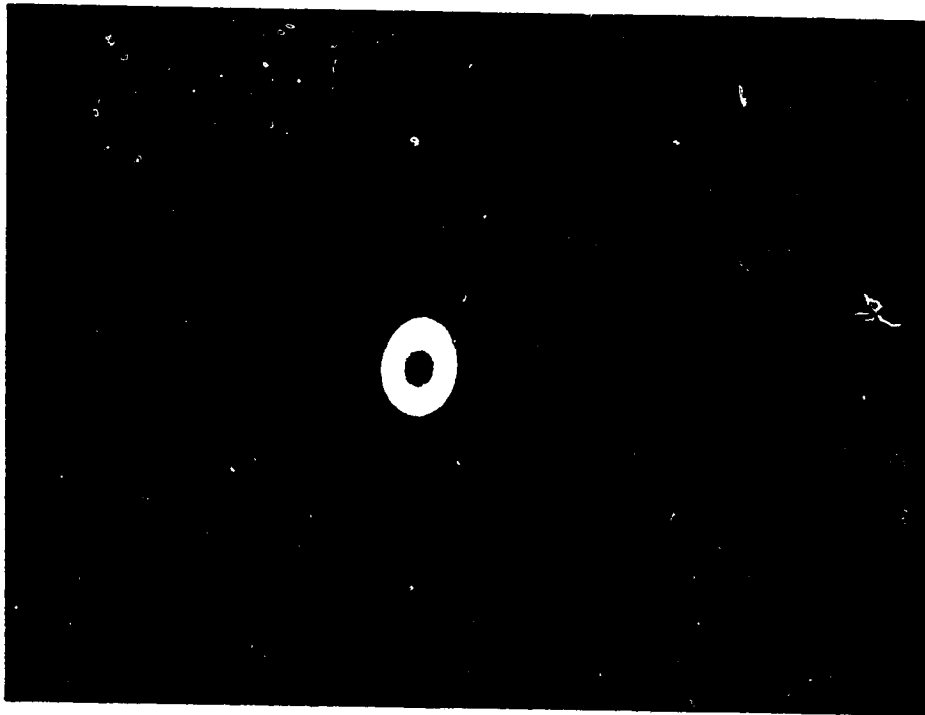


Figure 4.17 Near-field Beam Pattern for a Toric Confocal Resonator with  $M = 1.16$  and a 1.78 cm Aperture

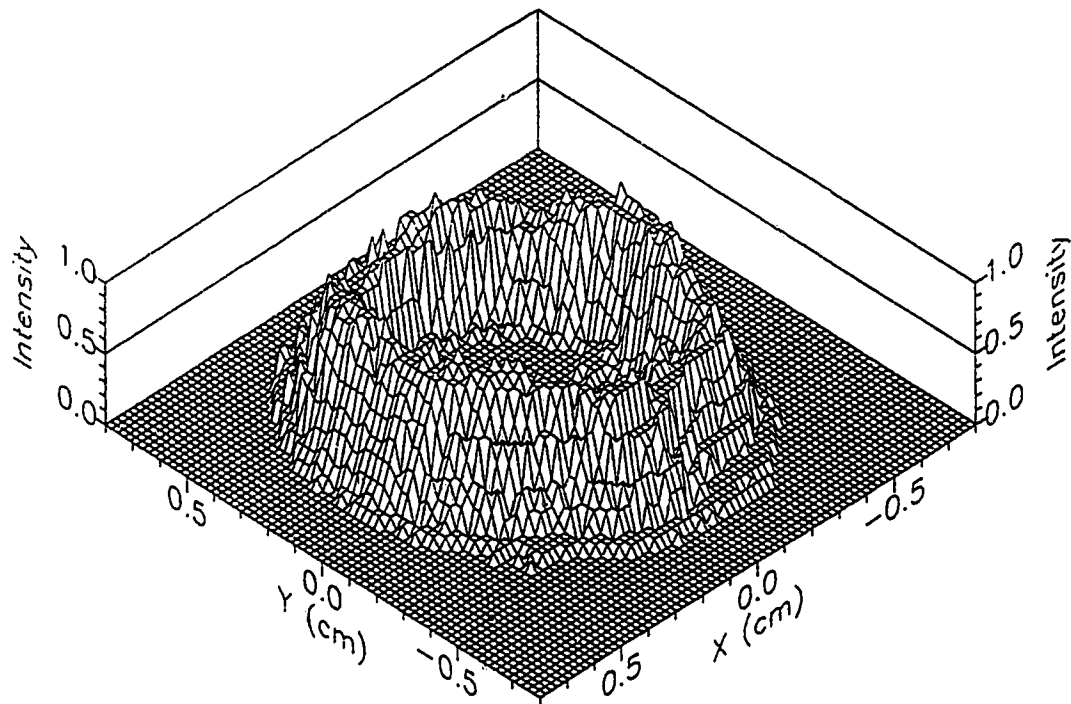


Figure 4.18 3-D Near-field Intensity Profile for a Toric Confocal Resonator with  $M = 1.16$  and a 1.78 cm Aperture

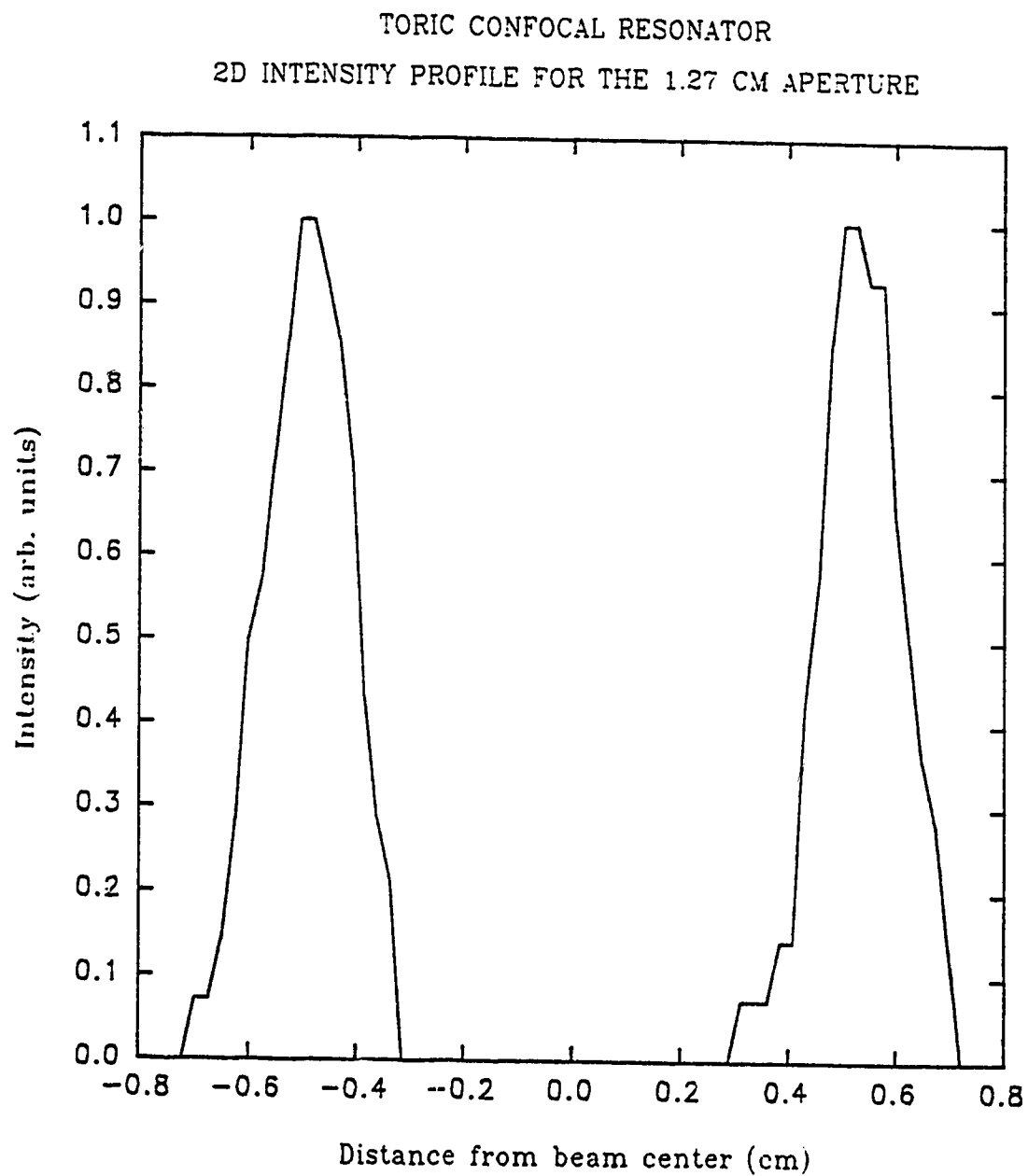


Figure 4.19 2-D Near-field Intensity Profile for a Toric Confocal Resonator with  $M = 1.16$  and a 1.78 cm Aperture



The  $1/e^2$  focal spot size variation with aperture size is shown in Figure 4.20. As is clear, the confocal resonator focal spot size followed a trend similar to that of the non-confocal case. When independent beamlets were present in the output profile, the focal spot size was essentially a constant, as indicated by the points to the right of line (a). Conversely, for all points to the left of line (a), the beamlets overlapped and formed an annular output in which the focal spot size increased inversely with the aperture size.

The variation of the output power as a function of aperture size in the convex mirror was also examined. The data from this study are presented in Figure 4.21. A maximum in the output was observed for an aperture size of  $\approx 2.50$  cm, which correlated well with the findings of the non-confocal resonator and the predicted ideal output coupling value, which was independent of resonator configuration.

Both the misalignment sensitivity and the output beam polarization were determined for the toric confocal resonator. The angular deviation required to produce a 50 % power reduction was found to be  $\approx 80$  s. This was in good agreement with the previously measured value for the non-confocal resonator with the same value of magnification. This was expected since the analysis by Krupke and Sooy had indicated a slight difference between a confocal and a non-confocal resonator type.<sup>200</sup> Another notable difference was the intensity profile of the misaligned beam. Since the output beam was an annulus when properly aligned, it took on a crescent or half-moon shape when misaligned.

The polarization of the output beam was found to behave in a manner similar to the non-confocal design when the individual beamlet aperture sizes were in place. When the output beam formed an annulus however, the polarization once again became the superposition of adjacent slots. This is depicted in Figure 4.22. Using the methods described in the toric non-confocal resonator section, it was discovered that the optical radiation was polarized linearly when it was probed adjacent to a discharge slot. However, when the annular part of the beam immediately next to an electrode tip was measured, it was found to be the combination of the two channels on either side of that point.

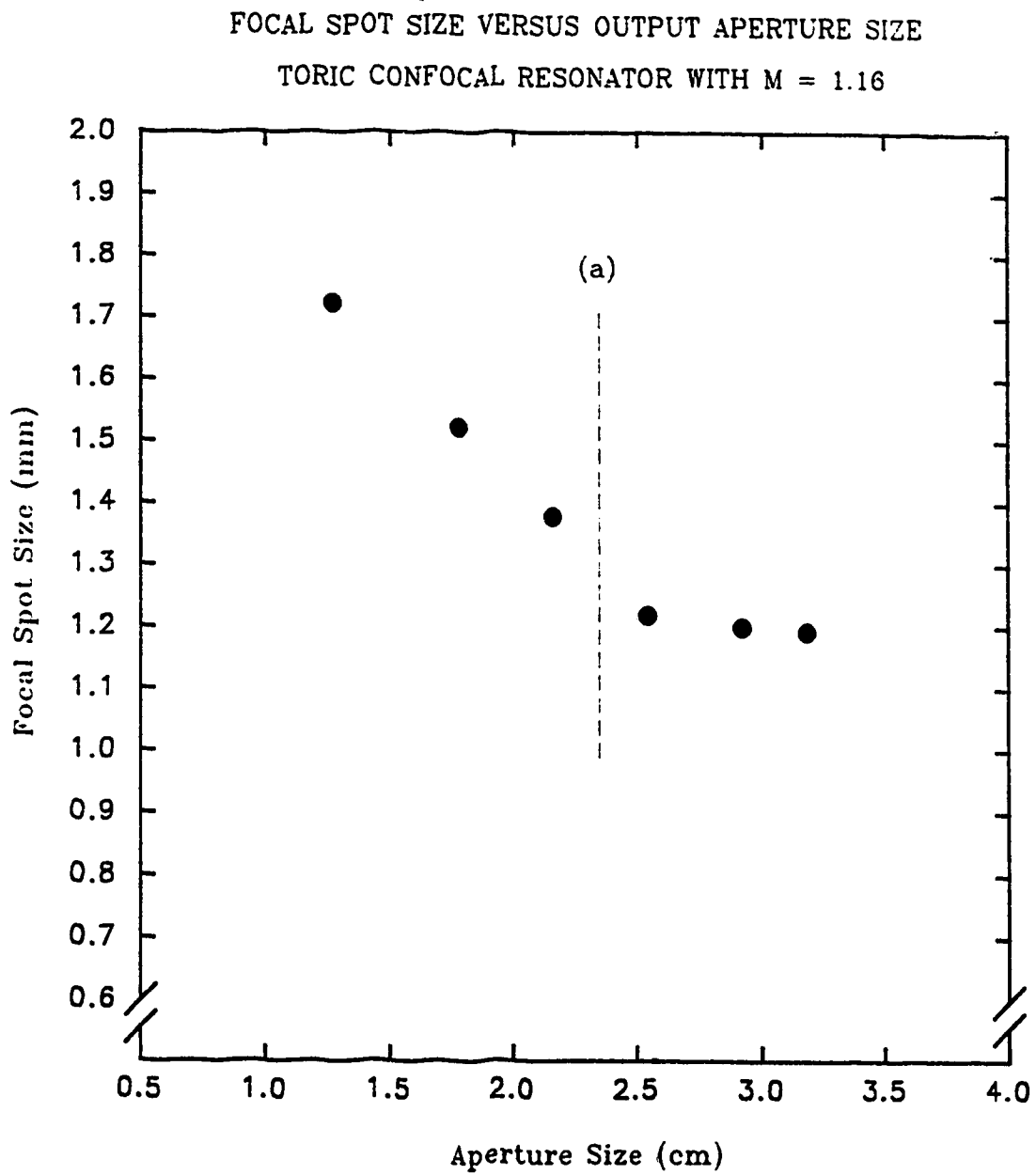


Figure 4.20 Variation of the  $1/e^2$  Focal Spot Size with the Aperture Size for a Toric Confocal Resonator with  $M = 1.16$

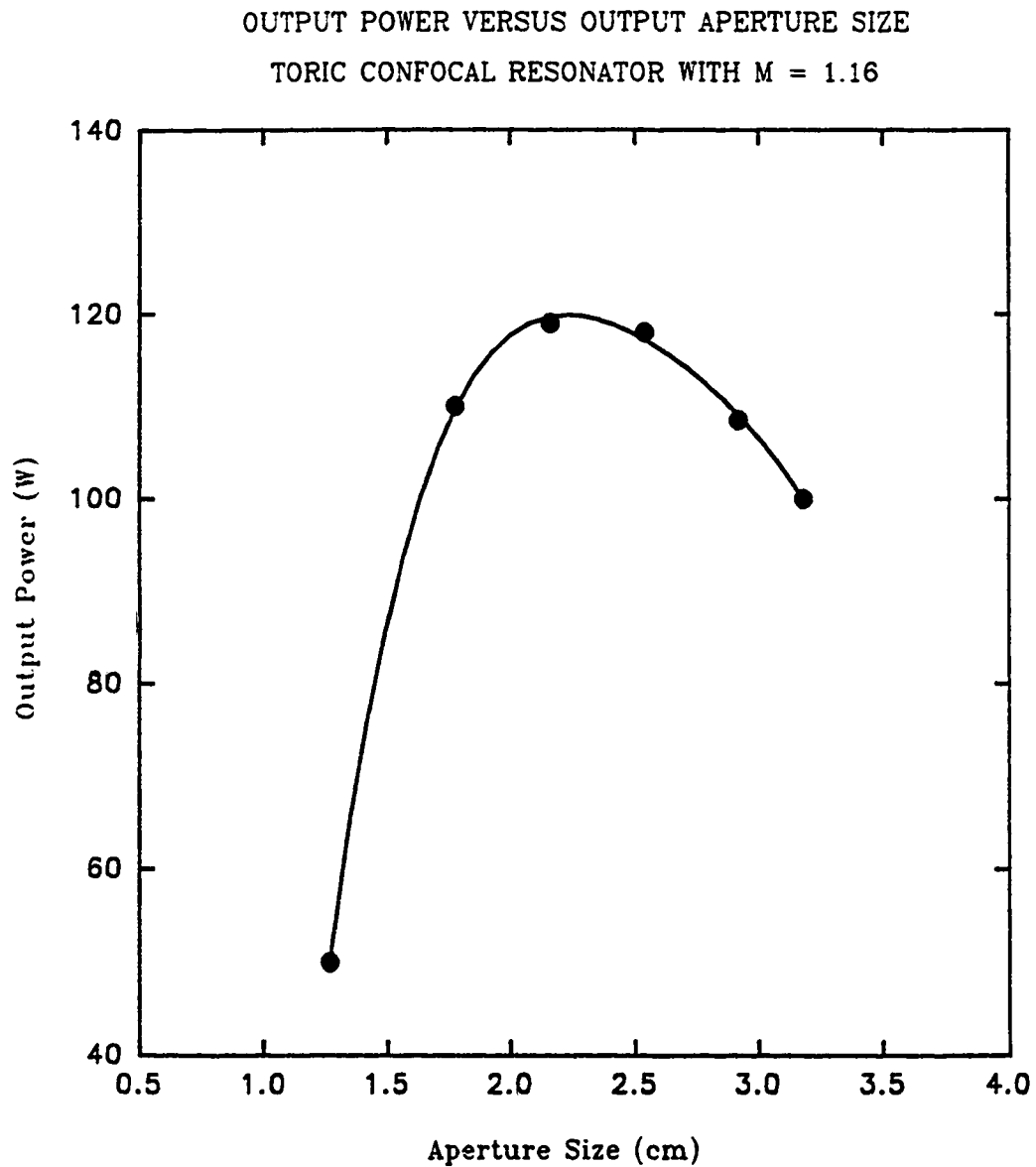


Figure 4.21 Variation of Output Power with Aperture Size for a Toric Confocal Resonator with  $M = 1.16$

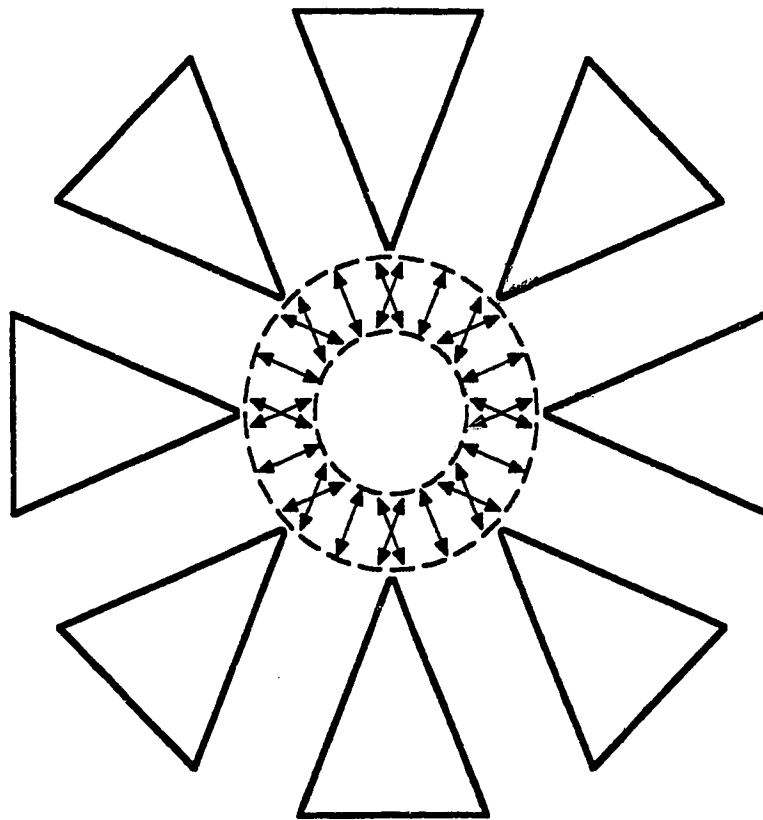


Figure 4.22 Schematic Representation of the Output Beam Polarization State for a Toric Confocal Resonator with a 2.16 cm Aperture

#### 4.4.3 Conventional Confocal Resonator

In order to provide a more complete comparison, the multichannel discharge structure was also fitted with a conventional resonator design. The same output parameter characterization, as described previously, was also conducted for this resonator.

The image of the output beams on a ceramic board is shown in Figure 4.23. This photograph was taken with a resonator magnification of 1.16 and a convex output mirror diameter of 8.64 cm. The individual beamlets were found to be very similar in appearance and this was further confirmed by the near-field intensity profiles which are shown in Figures 4.24 and 4.25.

The far-field properties of the conventional resonator were subsequently examined. A typical far-field pattern obtained by placing a Perspex rod at the focal point of a 25 cm ZnSe lens is presented in Figure 4.26. The burn pattern was very clean and indicated that there was little or no power contained in the sidelobes of the intensity profile. The variation of the  $1/e^2$  focal spot size as a function of output mirror diameter was also measured. The results of this survey, for convex mirror diameters ranging from 7.87 to 9.78 cm, are displayed in Figure 4.27. Immediately evident from the graph was the fact that the focal spot size was essentially a constant over the entire output mirror diameter range. This was expected since the output profile always contained eight individual beamlets.<sup>235</sup> The triangle in Figure 4.27 represents the diffraction-limited focal spot size for this particular situation, which is seen to be very close to the measured values for this parameter.

The effect of changing the convex mirror diameter on the output power was also investigated. These results are shown in Figure 4.28. The output power followed a trend similar to the previously examined resonator configurations. A peak in the output was found at an optimum mirror diameter of  $\approx 8.60$  cm. This corresponded to a geometrical output coupling factor of  $\delta^* = 19\%$ . The ideal value of coupling, given in Table 4.1, was 25.7%, which is slightly greater than the measured quantity. This decreased value was explained by considering the geometry of the discharge structure, and in particular, the central inter-electrode region. As pointed out in Chapter 3, and discussed in the preceding sections

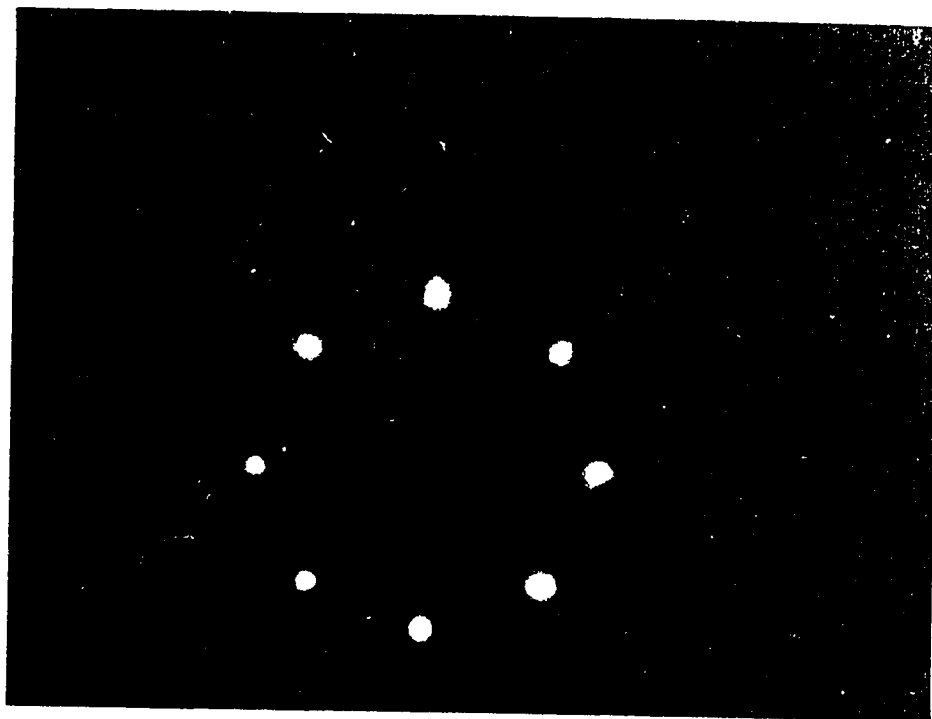


Figure 4.23 Near-field Beam Pattern for a Conventional Confocal Resonator with  $M = 1.16$  and an 8.64 cm Output Mirror Diameter

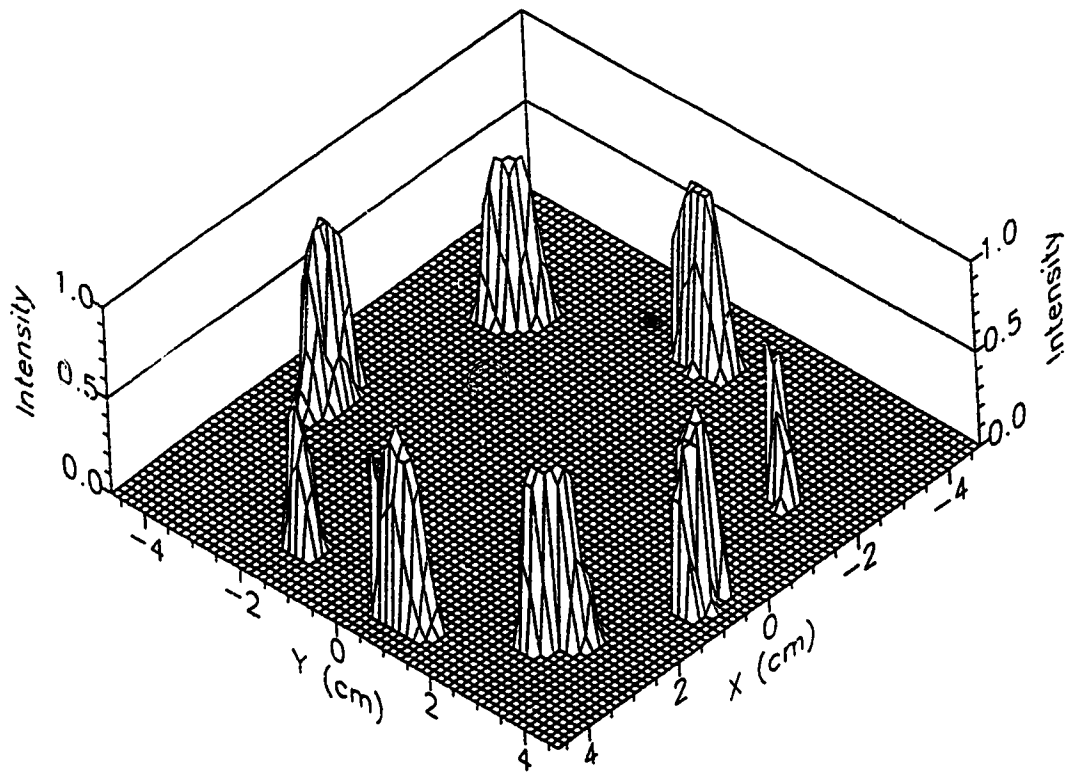


Figure 4.24 3-D Near-field Intensity Profile for a Conventional Confocal Resonator with  $M = 1.16$  and an 8.64 cm Output Mirror Diameter

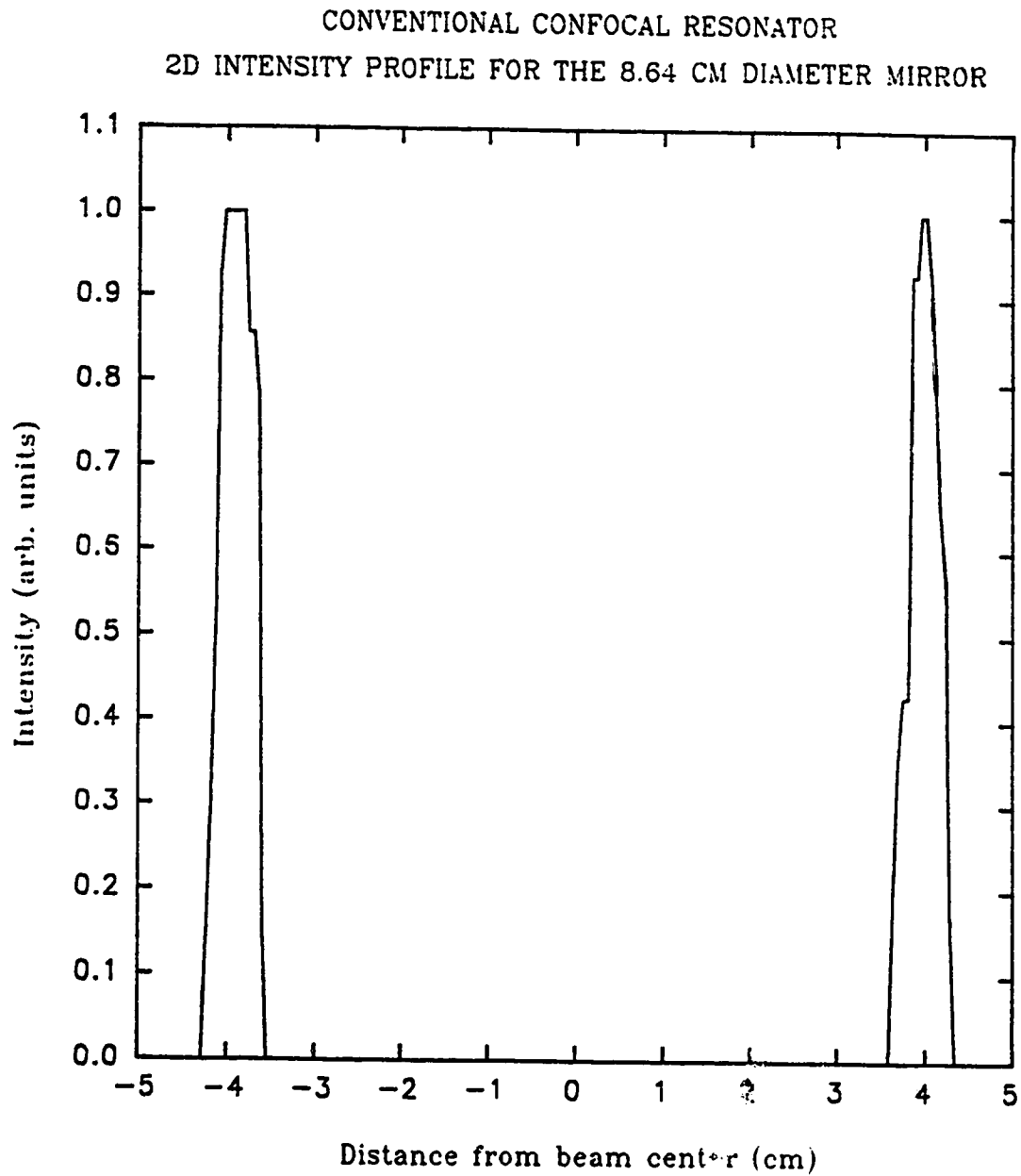


Figure 4.25 2-D Near-field Intensity Profile for a Conventional Confocal Resonator with  $M = 1.16$  and an 8.64 cm Output Mirror Diameter





Figure 4.26 Typical Far-field Burn Pattern in Perspex for a Conventional Confocal Resonator with  $M \approx 1.16$  and an 8.64 cm Output Mirror Diameter

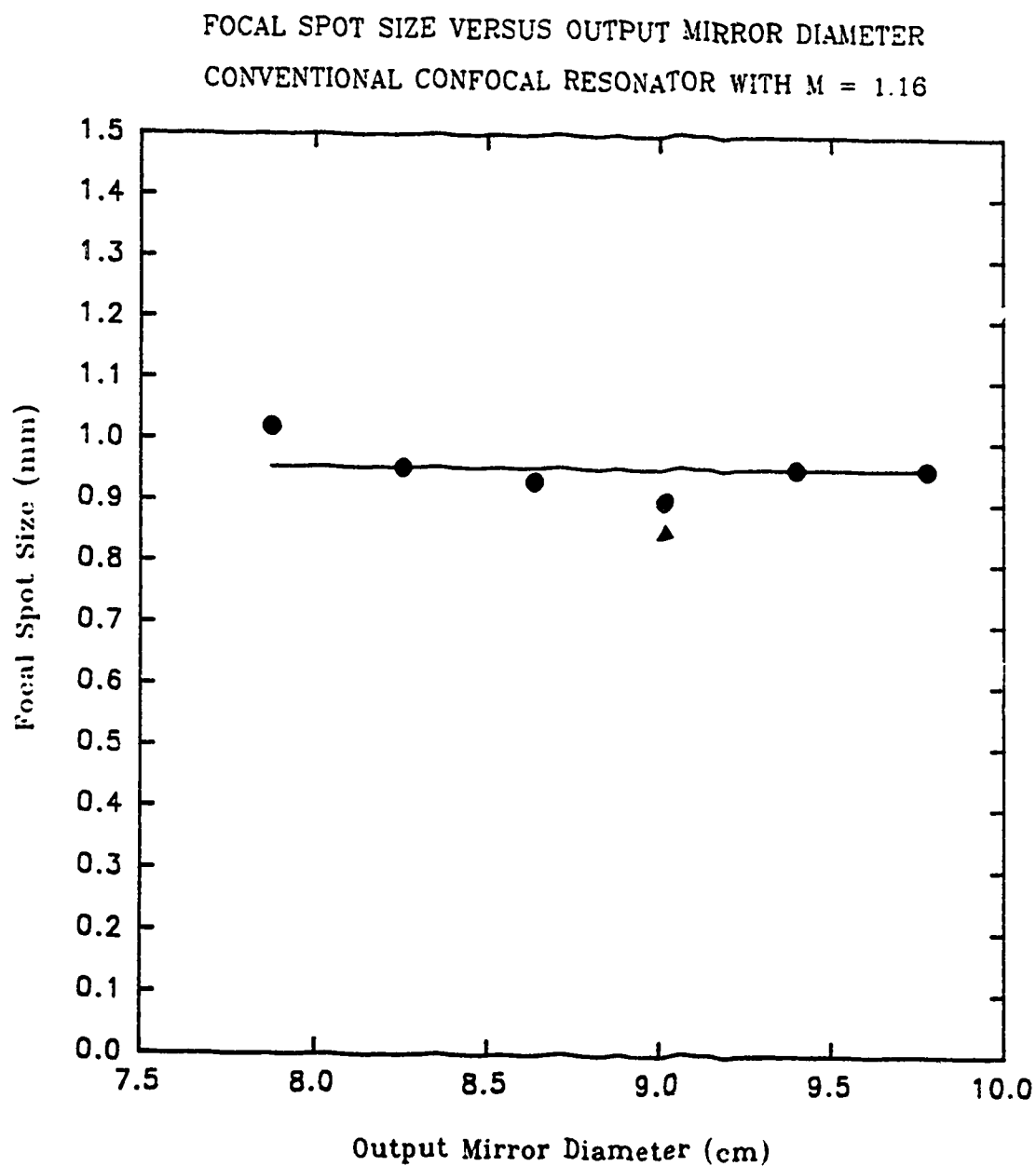


Figure 4.27 Variation of the  $1/e^2$  Focal Spot Size with the Output Mirror Diameter for a Conventional Confocal Resonator with  $M = 1.16$

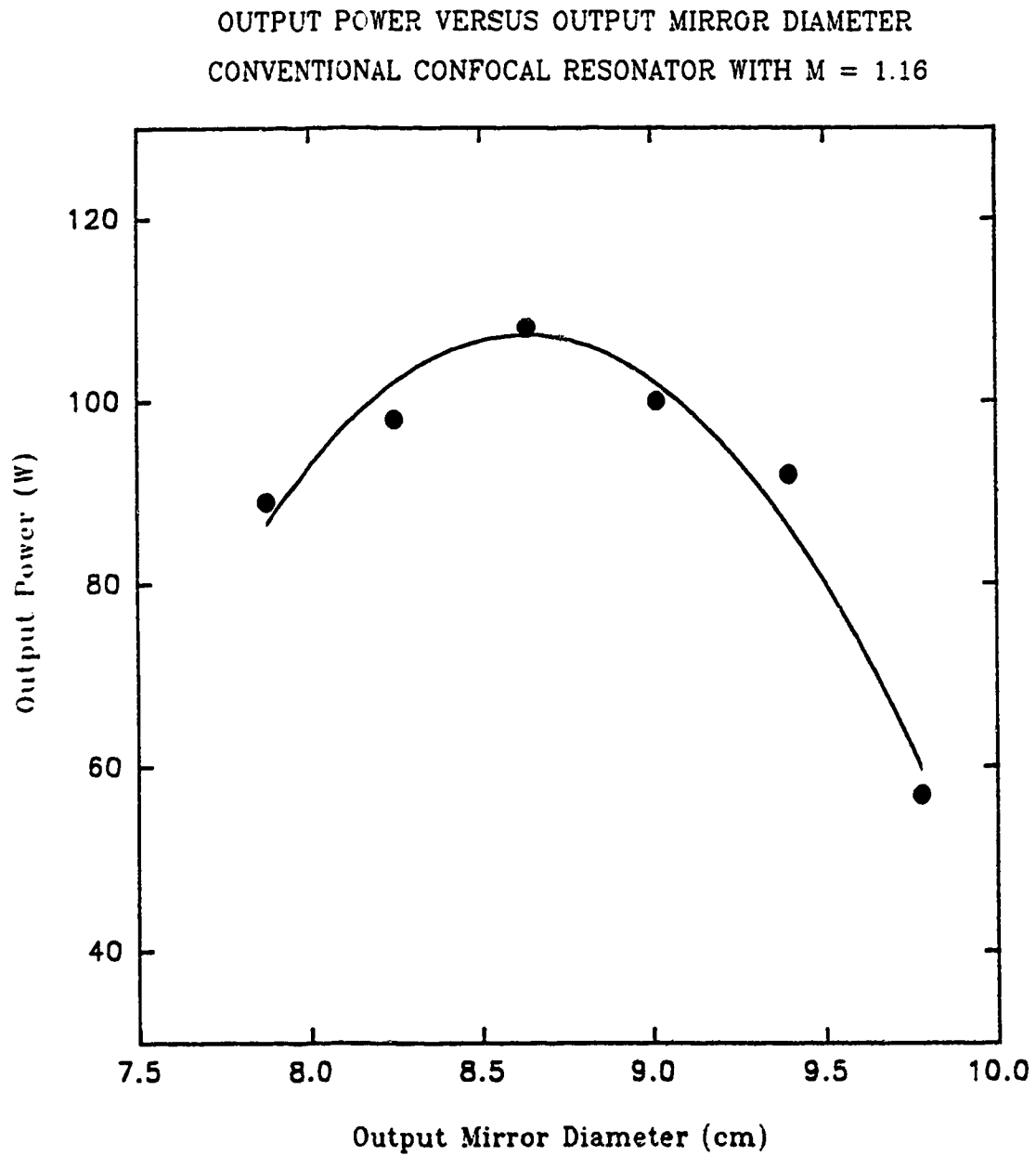


Figure 4.28 Variation of the Output Power with the Output Mirror Diameter for a Conventional Confocal Resonator with  $M = 1.16$

for the toric resonators, there was a significantly reduced value of gain in this central region. Therefore, a reduced value of  $\delta$  was found because the discharge does not completely fill the available volume. If the reduced gain region was subtracted from the overall discharge volume, and the output coupling recalculated, a value of  $\delta^* = 24.3\%$  was obtained. This was in much better agreement with the ideal value and emphasizes the importance of the central region of the resonator to the outer areas of the system. This subject will be dealt with in more detail in the discussion of phase-locking, which is presented in the following chapter.

The sensitivity to misalignment was also determined. It was found that an angular deviation of  $71^\circ$  was required to reduce the output power to one half of its maximum value. This was in good agreement with the analysis of Krupke and Sooy<sup>200</sup>, which predicted that an angle of  $78^\circ$  would be appropriate for the resonator in question here.

Finally, the polarization properties of the output beamlets were measured. The beams were found to be polarized predominately in a direction parallel to the electrode faces. However, there were also components of polarization in all other orientations, which indicated that the beamlets were actually randomly polarized. The ratio of maximum to minimum readings found with the polarizer was 10:1 at angles which were orthogonal to each other. The explanation for these results will be discussed shortly.

#### 4.4.4 Conventional Non-Confocal Resonator

For completeness, the series of experiments was also performed for the conventional non-confocal resonator. Fundamentally, there were no major differences observed with this resonator as compared to the confocal version. For this reason, only the salient distinctions are presented below.

The nature of the output beams was the same as the previous resonator. Shown in Figure 4.29 is the variation of output power with mirror diameter. The same general trend displayed by the previous resonators was observed, with a peak in the output found at a mirror diameter of  $\approx 8.80$  cm. The  $1/e^2$  focal spot size was also determined to be essentially constant over the entire range of convex mirror diameters used herein, and was found to be

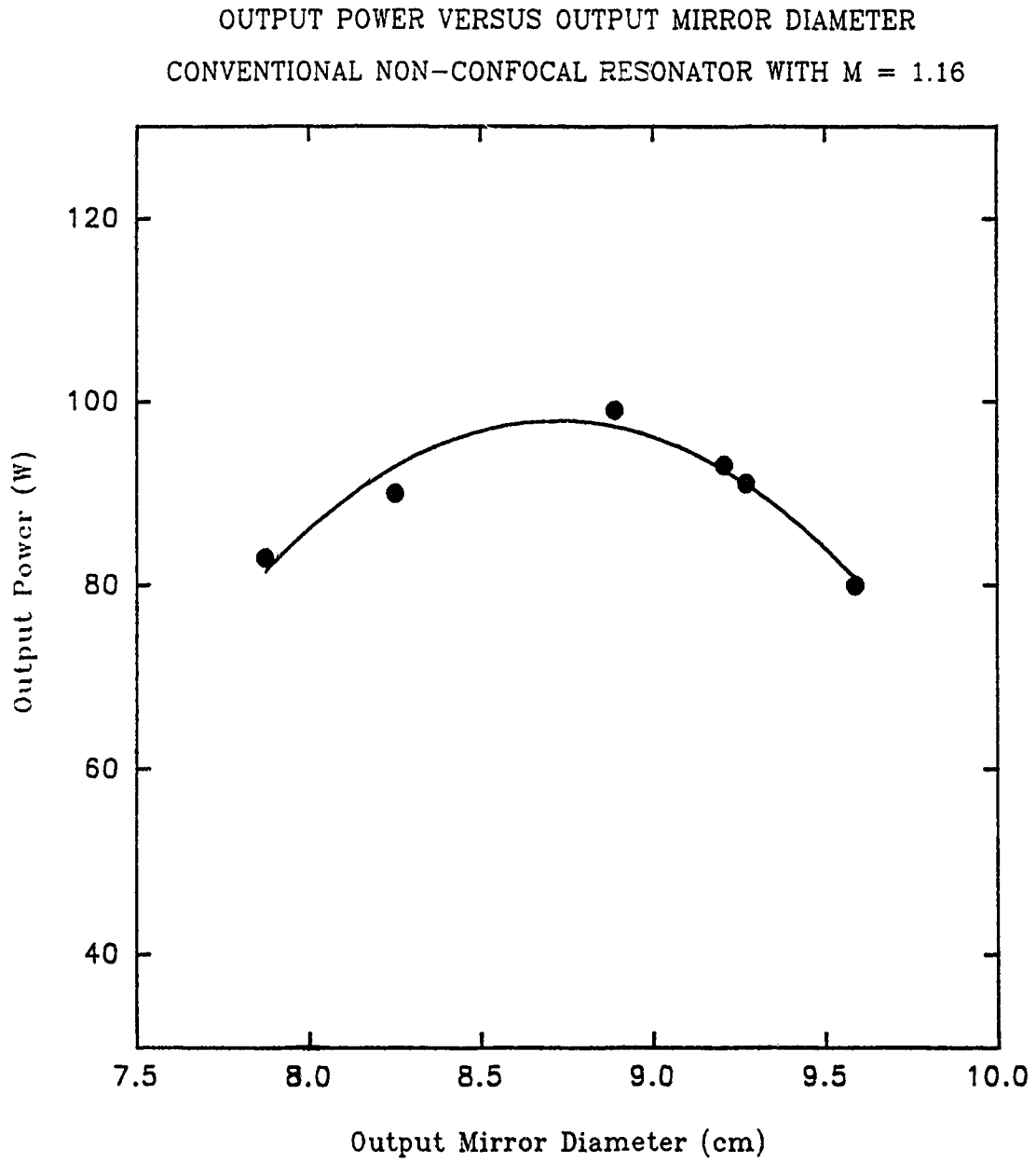


Figure 4.29 Variation of the Output Power with the Output Mirror Diameter for a Conventional Non-Confocal Resonator with  $M = 1.16$

0.93 mm. The polarization properties of the output beams were found to be identical to the confocal resonator design discussed above. In addition, the measured misalignment angle of 73° agreed well with the predicted value of Krupke and Sooy.

#### **4.5 Resonator Performance Comparison**

The previous several sections outlined the general characteristics of the individual resonators that were fitted to the multichannel laser structure. This section will compare some of these properties for the different resonators and explain the reasons for these distinctions.

Table 4.2 gives the  $1/e^2$  focal spot sizes for the x and y components of the beam for the various resonator configurations. Evident from the table is that the different resonators have distinct focusabilities. Both of the conventional resonators displayed small, and nearly symmetrical, beam waists, which were significantly better than any of the toric cases. Both confocal devices showed a slight asymmetry in the x and y components; however, this asymmetry was easily within the experimental error of  $\pm 50 \mu\text{m}$  for these measurements.

There are two possible explanations for the large disparity in focal properties observed for the two different resonator configurations. The two possibilities are related to the radius of curvature of the toric mirrors and to phase-locking of the individual channels. Combinations of these two effects are also a distinct possibility. Because of the machining process on the microsurface lathe, the toric mirrors were not spherical, as in the conventional resonator case, but were actually aspherical in shape. The surface of each mirror resembled a potential well, hence the gradient of the mirror curvature was not the same in all directions, as it was with a spherical mirror surface. Townsend and Reilly<sup>224</sup> have suggested that this may cause the optical mode to be compressed in the azimuthal direction as it walked toward the centerline of the device. However, because of the slot geometry used in these experiments, the mode was confined between the electrodes, and there was very little, if any, azimuthal compression. Therefore, it was possible that the curvature of the mirrors caused the beam to spread somewhat, with a larger amount of energy contained in the sidelobes. Hence, the beam did not focus as well as in the conventional unstable resonator configuration. This situation

Table 4.2 Focal Spot Size Variation with Resonator Type

Resonator Type	Aperture Size or Mirror Diameter (cm)	1/e <sup>2</sup> Focal Spot Size (mm)	
		x	y
TC	3.18	1.17	1.19
TNC	3.18	1.06	1.06
TC	1.78	1.48	1.56
TNC	1.78	1.36	1.36
CC	8.64	0.96	0.95
CNC	8.89	0.93	0.93

The resonator types are denoted as: TC = toric confocal, TNC = toric non-confocal, CC = conventional confocal, and CNC = conventional non-confocal.

was more pronounced with the confocal case because the mirror radii of curvature were much smaller.

The second factor was the possibility that some phase-locking occurred between the individual channels. This aspect will be more fully dealt with in the next chapter; however, tests indicated that there was a degree of phase-locking present with the conventional unstable resonator configuration. It is known that, had the individual beamlets been 100 % optically phase-locked, the output would have a far-field intensity profile that scales as the square of the number of beams.<sup>96</sup> Therefore, partial phase-locking would also produce a reduced focal spot size.

The larger beam waist obtained for the toric resonator with the 1.78 cm aperture was the result of an overlap of the multiple beamlets before they emerged from the system. As shown in section 4.4.1, beamlet overlap caused a broader intensity profile. This broader profile contained more energy in the sidelobes and thereby produced a larger focal spot size. Once again, if the beams could have been optically phase-locked, a much sharper focal spot size with a correspondingly improved beam quality would have been achieved.

Table 4.3 summarizes several of the measured parameters for the various resonators. Included in this list is the maximum output power obtained with the different optical configurations. This data revealed that the confocal resonators had consistently higher output power than the corresponding non-confocal systems. Also, the toric designs provided greater output power levels than similar conventional resonators. The explanation for these observed differences is given below.

The major difference between toric and conventional unstable resonators stems from how these systems utilized the available discharge volume. The optimum toric aperture was found to be slightly larger than the inner edge of the electrode assembly, whereas the optimum conventional aperture exposed part of the outer radial portion of the active discharge region. It therefore appears that the toric resonator more effectively used the entire discharge region as gain medium. In particular, it was shown that a reduced value of gain coefficient exists in the central region of the discharge assembly, due to the diffusion of



Table 4.3 Summary of Various Resonator Properties

Resonator Type	Aperture Size or Mirror Diameter (cm)	Output Power (W)	Misalignment Angle (seconds)	Polarization State
TC	2.54	120	80	linear
TNC	2.54	101	83	linear
TC	1.78	110	80	linear superposition (see text)
TNC	1.78	81	83	no preferential direction (see text)
CC	8.64	108	71	random
CNC	8.89	99	73	random

The resonator types are denoted as: TC = toric confocal, TNC = toric non-confocal, CC = conventional confocal, and CNC = conventional non-confocal.

vibrationally excited species into this region. Consequently, the energy gained during the final passes through the central portion more than compensates for the additional mirror losses in this area. The optimum toric aperture was therefore found to lie within this central zone, near the inside edge of each electrode. However, if the beam is forced to make many more passes through this region, increased losses occur due to absorption in the non-cooled gas. This phenomenon is reflected in Table 4.3, where it is seen that considerably smaller toric apertures indeed resulted in lower output power.

In contrast, the conventional resonator does not make such optimum use of the gain medium. Since there was reduced gain in the central region of the structure, primary beam development did not begin until very near the inner edge of the discharge region. At the other extremity, after the cavity mode has walked through the discharge slot, the output beam emerged. However, unlike the toric resonator, the final pass through the gain medium in the conventional design was just an amplification pass, since the optimal mirror diameter exposed part of the gain medium. Again this phenomenon was related to the diffusion of vibrationally excited species within the discharge. Because of the cylindrical geometry of the structure, the volume into which any particles diffused was inversely proportional to the radial distance from the device's centerline. Hence, particles which diffused into the central region occupied a much smaller volume than those at the outside edge of the electrode assembly. This in turn implied that a larger value of gain was available near the inner edge of the electrodes than at the opposite side. Therefore, in summary, the toric resonator made better use of the gain medium and subsequently yielded a higher output power under the same discharge conditions.

The difference in power levels for the confocal and non-confocal versions of both resonator designs was believed to be related to the radii of curvature of the mirrors. In the non-confocal cases, the curvature of both mirrors was significantly larger than for the confocal situation. Larger curvatures implied more passes through the gain medium and hence, more overlap of each pass. This aspect may have caused over-saturation of the gain medium. Consequently, additional amplification passes actually reduced the available output power, since they contributed additional mirror absorption losses once the gain had been fully

depleted.

The measured values of misalignment sensitivity were all very similar. This was somewhat expected since the analysis by Krupke and Sooy applied to the confocal and non-confocal resonators predicted only a 2 second difference in the misalignment angle.<sup>200</sup> Perhaps more striking was the similarity in the measured values for the toric and the conventional designs. Townsend and Reilly<sup>224</sup> have concluded that an equivalent toric system was less sensitive to misalignment than a conventional resonator design. This property was borne out in the data collected herein, however only marginally so. Two factors were present that could have influenced this parameter. First, the geometry studied herein consisted of multiple individual slots, whereas Townsend and Reilly analysed a completely open structure. This perturbation could affect the properties of the resonator, such as the azimuthal mode compaction which was discussed previously. Second, the gain in the system was not uniform across the entire mirror diameter, therefore the output coupling factors, output power levels, and other characteristics of the resonator were modified to a certain extent.

The ascertainment of dissimilar polarization states for the conventional and toric resonators was not anticipated. This follows since the discharge gap was the same in both resonators, and was large enough to allow for free space propagation to occur in both electrode gap directions.<sup>67</sup> Also, there were no optical elements present that would select a particular polarization direction. Since all mirrors used in these experiments were fabricated on the same microsurface lathe, the quality of each mirror should be identical. Polarization effects due to any mirror surface grooves produced during the diamond machining process were discounted, as they were also present on the conventional resonator optics, which produced a randomly polarized output beam. It was postulated therefore, that the polarization selectivity observed in the toric resonators was caused by the curvature on the mirrors themselves. As described previously, the toric resonator mirrors were surfaces of revolution that were aspherical. Thus, the curvature of the mirrors was such that some portion of the propagating beam could have been directed toward the electrode surface. This results in the perpendicularly polarized component of the beam experiencing larger losses due to interaction

with the electrode. This is similar to the polarization selection method in a typical waveguide laser.<sup>67</sup> However, as will be shown in the following section, under the appropriate conditions the conventional resonators also produced linearly polarized output beams.

#### 4.6 Central Inter-electrode Region Experiments

Due to its unusual properties, and the pending importance of the central region to phase-locking experiments, a series of measurements were performed to gain a better understanding of this region in the discharge structure. As was noted earlier, the gain coefficient in this zone was  $\approx 25\%$  of that in the inter-electrode gap regions. However, it was unknown if any output power could be extracted from this area of the optical resonator.

To investigate this possibility, a conventional confocal resonator was installed in the system, but the convex mirror had an additional 1 mm hole drilled through the centerline of the resonator. The output from all of the other channels was directed into a beam block and only an area around the geometrical center of the system was left undisturbed. There was output power detected from this hole and a value of 35 mW was found. Subsequently, the size of the hole was then increased to 3 mm and this resulted in  $\approx 800$  mW of output power being detected. Obviously something very interesting was taking place in the central discharge region.

There were two possibilities that could explain the above results. First, the beam that was detected from the central region may be somehow emerging from the individual channels and then walking through the central region to escape from the hole on axis. The second possibility was that enough gain existed in that zone so that lasing could take place independently of the other channels.

The first explanation suggested above has actually been known to exist in unstable resonators, and is technically referred to as the converging or reverse wave phenomenon. This wave is a manifestation of the solution to the resonator equations and is as equally valid as the more familiar forward travelling, or magnifying, wave solution.<sup>217</sup> This reverse wave has the same radius of curvature as the forward wave. The term converging wave, or

demagnifying wave, is appropriate since on each round trip through the resonator the transverse size of this wave is reduced by a factor of  $1/M$ . In contrast, the forward wave solution is magnified by a factor of  $M$  on each successive round trip in the resonator. It has been shown that the converging wave is considerably weaker in intensity than the forward wave however, this intensity may be enhanced by scattering off sharp edges of output mirror apertures<sup>239</sup>, or judiciously placed reflective surfaces.<sup>240</sup> It is therefore possible that a converging wave could walk backwards through the inter-electrode slot, through the central region, and then emerge from the hole in the convex mirror.

To further probe this hypothesis, several ceramic plugs were fabricated that could be placed in the central region of the discharge structure. One plug was a solid disc, one was a 0.635 cm thick annulus with a 0.635 cm hole in the center, and a third disc was a 0.3175 cm annulus with a 0.9525 cm hole in the middle. Each of these plugs was placed, in turn, into the laser system. With the 0.634 cm annulus in place, only the eight individual beams from each of the electrode slots were present. There was no indication of any output from the central hole. However, with the 0.3175 cm annular disc, 150 mW of power was detected from the central region. Unfortunately, these tests were not conclusive since it was still possible that part of the beam could "jump" over this annulus, and continue unaffected toward the central hole.

A final decisive test was implemented. An absorbing mask was made that had a central hole equal to the central inter-electrode region in size. Additionally, this mask covered the remaining output mirror area except for  $\approx 6$  mm at the top of each electrode slot. In this manner, the proper resonator alignment could be achieved by detecting the eight individual beams, as well as ensuring that no part of these beams could be reflected into the central region and still emerge through the on axis hole. With this mask in place, an output power of 5 mW was observed from the central region of the laser structure. There was no possible way that any beam could pass over the 2 cm absorbing region in order to reach the central area. Therefore, it was concluded that the central region of this structure contains enough gain to overcome the losses present and lase independently.

Because of the influence that this central section may have on attempting to phase-lock the output beams, the polarization of this region, and its effects, were investigated. First, the beam that was produced solely in the central region was found to have a random polarization. In light of previous discussions, this result was expected since there were no polarization selective elements in this central zone. An experiment was also performed with the solid ceramic disc inserted into the central region. With this plug in place, the polarization of the eight individual output beams was measured. It was found that, under these conditions, the channels were linearly polarized just as in the toric resonator cases. Therefore, the previously measured random polarizations were caused exclusively by the influence of the central region of the discharge assembly on the individual channels. This aspect will be dealt with in more detail in the chapter concerned with the phase-locking experiments.

#### **4.7 Optical Resonator Summary**

The results of this chapter have elucidated several of the characteristics of toric and conventional unstable resonators that have been fitted to multichannel laser systems. The selection of the appropriate resonator type depends on the desired application of the system. For instance, it was found that a toric resonator design produced the largest output power with a less sensitive alignment tolerance. In contrast, the conventional resonator configurations produced consistently smaller focal spot sizes. It was also determined that the central region of the discharge structure could lase independently, and could also influence the behaviour of the discharge channels. This feature could be of great significance with respect to the desire to achieve phase-locking amongst the individual channels of this multichannel laser array.

## CHAPTER 5

### PHASE-LOCKING STUDIES

The optical extraction experiments discussed in the preceding chapter demonstrated the viability of the extended-area electrode, multichannel laser array concept. However, the feasibility of phase-locking all of the individual channels has yet to be addressed. This chapter presents the results of experiments performed to ascertain the feasibility of phase-locking such a laser structure.

#### 5.1 Introduction to Phase-Locking

The coupling or phase-locking of lasers has been studied periodically since the invention of the laser itself. As presented in Chapter 1, numerous investigators have conceived of, and implemented, some very elaborate and elegant methods by which to phase-lock multiple laser devices.

The motivation to couple several independent lasers arises from the desire to achieve a larger and more powerful device than would otherwise be possible from a single source. This goal is typified by materials processing applications, which require high beam intensities, and in lidar applications which demand a high power, yet ultrastable laser source.<sup>241</sup> The scaling of current technologies to larger devices has encountered two main stumbling blocks.<sup>105,127</sup> First, the physical processes within the gain medium have generally restricted the scale-up size and thereby limited the output power attainable from a single device. Second, the availability and prohibitive cost of adequate optical systems for higher power lasers has further hampered single device development.<sup>242</sup>

In contrast, coupled laser systems can produce mutually coherent multiple output beams, which can be coherently added in the far-field. This mutual coherence allows the multiple beams to act as one.<sup>243</sup> Ideally, the combination of  $N$  separate, but coherent beams, increases the far-field intensity profile by a factor of  $N^2$ , with a corresponding reduction of the far-field focal spot size by  $\sqrt{N}$ .<sup>127</sup> As an example, the intensity of two combined beams is

given by:<sup>244</sup>

$$I_c = I_1 + I_2 + 2\sqrt{I_1 I_2} \cos \phi \quad (5.1)$$

with

$$\phi = \text{phase difference} = \frac{2\pi}{\lambda} d \quad (5.2)$$

where  $I_c$  is the combined beam intensity,  $I_j$  is the intensity of the individual beams,  $\lambda$  is the output wavelength and  $d$  is the optical path length difference. As indicated by equation (5.1), for two beams of equal intensity and zero path length difference, the combined intensity becomes the square of the number of beams. On the other hand, incoherent lasers only produce a far-field intensity that is  $N$  times as bright as a single source, and no reduction in the focal spot size is observed.

Having established the advantages of phase-locking several individual devices together, some techniques commonly used to detect the presence of phase-locking are now presented. Since one of the benefits of laser radiation is its high degree of temporal and spatial coherence, these properties can be exploited to determine phase-locking. As mentioned previously, the combination of several coupled beams results in an increase in the far-field intensity profile with a concomitant reduction in the focal spot size. The identification of this phenomenon has been used as one method to demonstrate phase-locking between separate laser devices.

A second method used was also based on a similar feature. One manifestation of the above-mentioned coherence of a laser is the ability of the output beam to interfere with itself. The interference fringes that are produced in the overlapped region can then be detected. It is well known that two independent lasers, operating at essentially the same wavelength, do not produce any interference fringes when they are overlapped.<sup>245</sup> Thus, a second method to determine phase-locking is to observe any interference phenomena between the individual



lasers. If any interference is detected, the degree of cross-coupling, or correlation, can be calculated from the visibility function, which is given by:<sup>155</sup>

$$V = \frac{I_{\max} - I_{\min}}{I_{\max} + I_{\min}} \quad (5.3)$$

where  $I_{\max}$  and  $I_{\min}$  are the maximum and minimum detected intensities of two consecutive light and dark fringes, respectively. Clearly, equation (5.3) ranges from zero for completely incoherent beams, to unity for 100 % phase-locked outputs.

A third method by which phase-locking can be detected is that of beat frequency analysis.<sup>94,115,154</sup> It is well known that two superimposed electromagnetic waves of frequencies  $\nu_1$  and  $\nu_2$  also produce a characteristic beat frequency which is given by the difference  $\nu_1 - \nu_2$ . Therefore, if the output from two separate laser channels overlap, and this combination is subsequently directed into a suitable photodetector, the absence of a beat frequency signal implies phase-locking between the two beams. This method also provides an opportunity to measure the fundamental locking range, which is the region over which the path lengths of one optical resonator can be varied while still maintaining phase-locking with the other devices. This feature is usually accomplished by observing the output from a fast photodetector on an RF spectrum analyzer, while the length of one of the resonator cavities is adjusted with a piezoelectric transducer mounted onto one of the primary mirrors.

A final technique that has been employed to detect phase-locking, or especially injection locking, was demonstrated by Bigio and Slatkine.<sup>119</sup> By observing the output polarization of a given system, and in particular the amount of power contained in the output beam in a certain polarization direction, phase-locking effects can be detected. For example, if a linearly polarized beam is injected into a randomly polarized system, the resulting output beam has a larger percentage of its emerging optical energy in the linearly polarized direction if phase-locking has occurred. In this manner, an estimate of the amount of locking can be determined from the ratios of output power at a particular polarization orientation with and without an injection beam.

## 5.2 Phase-Locking Experiments

A series of experiments was performed in order to evaluate the feasibility of attaining phase-locking in the multichannel laser system described herein. Two basic methods were implemented: that of injection locking, and that of optical coupling between the individual channels themselves. The results of these experiments are presented below, followed by a discussion of their significance.

The principal layout of the experimental apparatus used to conduct these measurements is depicted in Figure 5.1. Basically, two of the output beams from the multichannel laser system were extracted from the device, combined together via the turning mirror and the ZnSe beam splitter, and then the resulting intensity patterns were viewed on a thermal imaging screen. The same methods that were previously described in Chapter 4 were used to perform the intensity profile analysis of the images so formed on the screen.

### 5.2.1 Injection Phase-Locking

A Synrad model 48-2 waveguide CO<sub>2</sub> laser was utilized in these injection locking experiments. The beam from the Synrad was directed through a 3 mm hole in the center of the front convex resonator mirror and into the optical cavity of the multichannel structure. A conventional confocal unstable resonator having a 7.87 cm diameter aperture with a magnification of 1.16 was used for all of the tests. RF input power, gas mixture, and gas pressure were also held constant during the procedure.

Injection locking experiments were performed first, in order to observe the effect of injecting a source beam down the centerline of the system. The source laser beam was directed into the multichannel laser system and aligned such that output radiation could be detected from all eight of the individual channels when only the injected beam was operating. It was estimated that if the injected beam was divided equally into all of the slots, approximately 280 mW of energy was being deposited into each channel.

To ascertain the effect of this injection, the polarization method of determining phase-locking was initially employed. The total output power, which included the

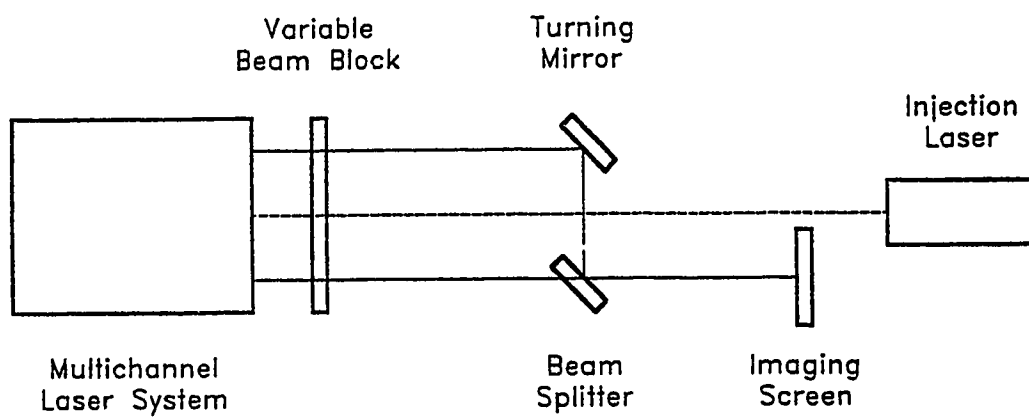


Figure 5.1 Block Diagram of the Experimental Arrangement Used for the Phase-Locking Measurements

contributions from all polarization directions, was measured for a given channel. Then the output power that was reflected from an uncoated ZnSe plate, oriented at the Brewster angle, was also measured. It is known that at the Brewster angle, only the component of the incident beam which is polarized parallel to the plane of the ZnSe plate is reflected.<sup>194</sup> Therefore, a comparison of the amount of optical energy reflected from the Brewster plate, both with and without the injected beam, indicated to what extent the injecting laser had influenced the polarization of the output beam and hence, the amount of phase-locking that had taken place.

The total output power, and that reflected from the ZnSe plate, were measured for three different system channels, one each in the vertical, horizontal and diagonal directions. It was found that in all cases, both in the presence and absence of the injected external beam, the total output power was  $\approx 12.3$  W. The amount of power that was reflected from the Brewster plate was equal to 9, 2.7 and 1.35 W, for the vertical, diagonal and horizontal slots, respectively. These results corresponded to the amount of output power that was naturally linearly polarized in a direction which was parallel to the vertical channels of the multichannel laser system. When the injection beam was turned on, the reflected output powers that were detected were 9, 3.5 and 3.0 W, respectively. These values corresponded to a zero, 30 and 122 percent increase in the observed reflected power from each of the channels. From the above results, it was concluded that injection of a beam into the cavity did indeed initiate phase-locking and that this effect was more pronounced in the channels that were oriented perpendicularly to the direction of the injected beam's polarization. Near-field interference fringe patterns were also captured for the above experiments, and the findings of these are discussed below.

In order to gain deeper insight into this phase-locking phenomenon, interference intensity profiles were also gathered using the imaging techniques described in Chapter 4. Several combinations of two output channels were examined. These consisted of: adjacent slots, orthogonal slots, channels separated by  $135^\circ$  and opposite channels. Prior to this, and in order to confirm that any interference fringes observed were actually caused by phase-locking, the intensity profile of one single beam was measured. This profile is shown in Figure 5.2.

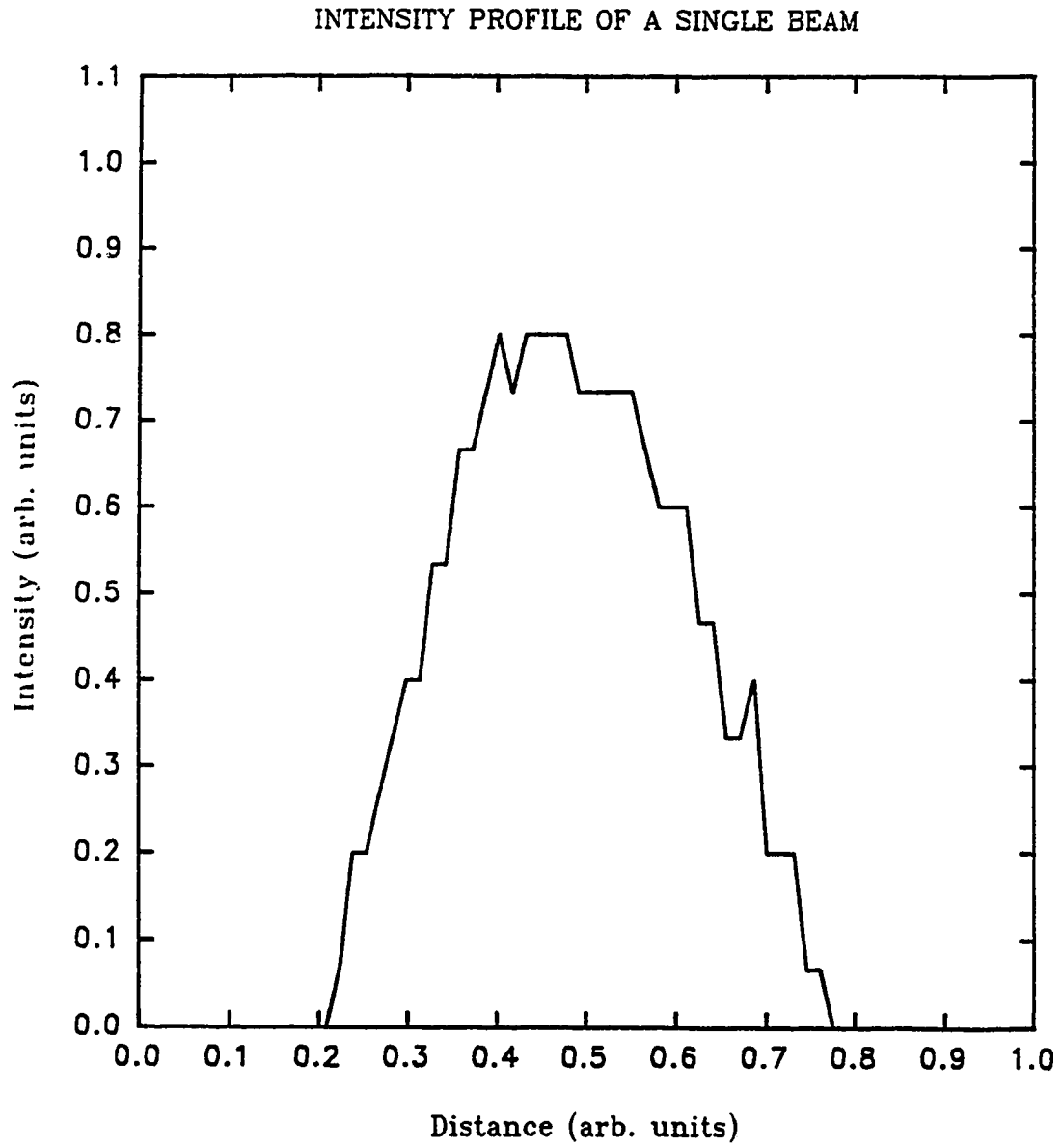


Figure 5.2 Intensity Profile of a Single Beam

Clearly this figure indicates that no fringes are visible with only a single beam present.

In contrast however, fringes were observed when two beams were overlapped while the injection beam was present. A photograph of a typical interference fringe pattern is shown in Figure 5.3. This pattern was obtained from two adjacent channels and the corresponding intensity profile is shown in Figure 5.4. From this figure, and with the aid of equation (5.3), the average visibility was calculated to be 0.91. In a similar fashion, the visibilities of the other channel combinations were found to be 0.40 for the orthogonal slots, 0.42 for the 135° separation set and 0.66 for the opposite channel pair.

### 5.2.2 Self-Phase-Locking

Experiments were also performed with the injection laser source removed. The outputs from the same pairs of channels were again combined together and observed on the thermal imaging screen. A typical intensity profile of the interference fringes obtained from two adjacent channels is shown in Figure 5.5. Calculations from this figure indicated that an average visibility of 0.47 was observed. The other channel combinations produced visibilities of 0.22, 0.32 and 0.62 for the orthogonal, 135° separation and opposite slots, respectively. These results indicate that there was a certain amount of optical coupling between the individual channels. This coupling was obviously greater for slots that were oriented in the same direction. These findings will be explored more fully in a subsequent section.

In order to further examine this apparent self-phase-locking feature, a series of experiments were conducted with a ceramic plug inserted into the central inter-electrode region. This was done in an effort to assess the effect of the central region of the resonator on the phase-locking properties of the system. Figure 5.6 shows a typical output intensity profile that was obtained during these experiments. Immediately evident from this figure is the lack of any detectable interference phenomenon. Similar results were recorded for all combinations of output beams. This data clearly indicates that the central region of the discharge structure is crucial to this self-phase-locking process.

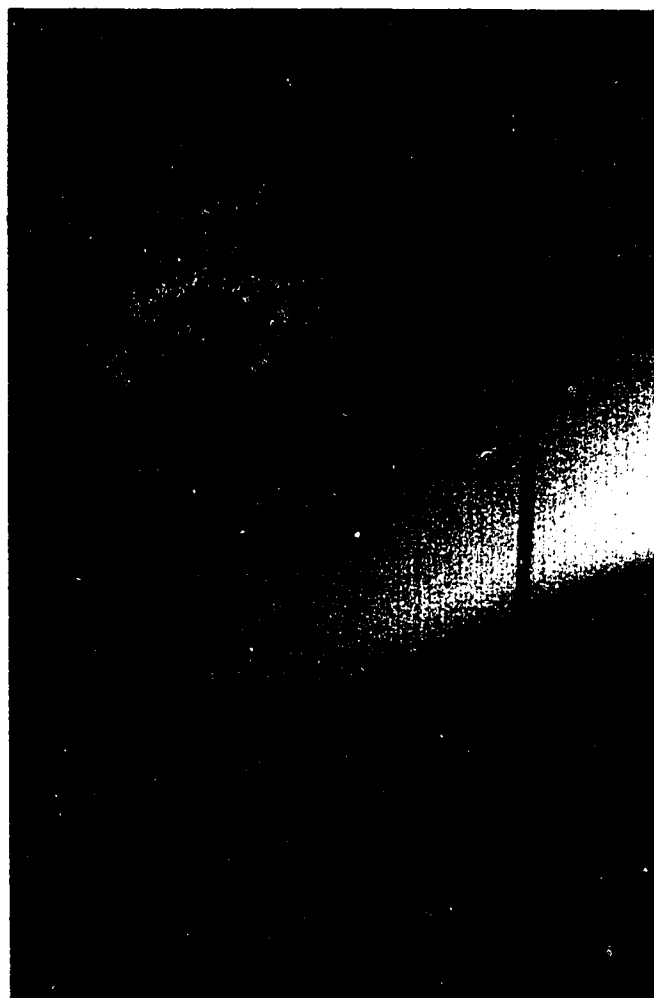


Figure 5.3 Photograph of a Typical Interference Fringe Pattern

ADJACENT CHANNEL INTERFERENCE FRINGES  
WITH AN INJECTED BEAM

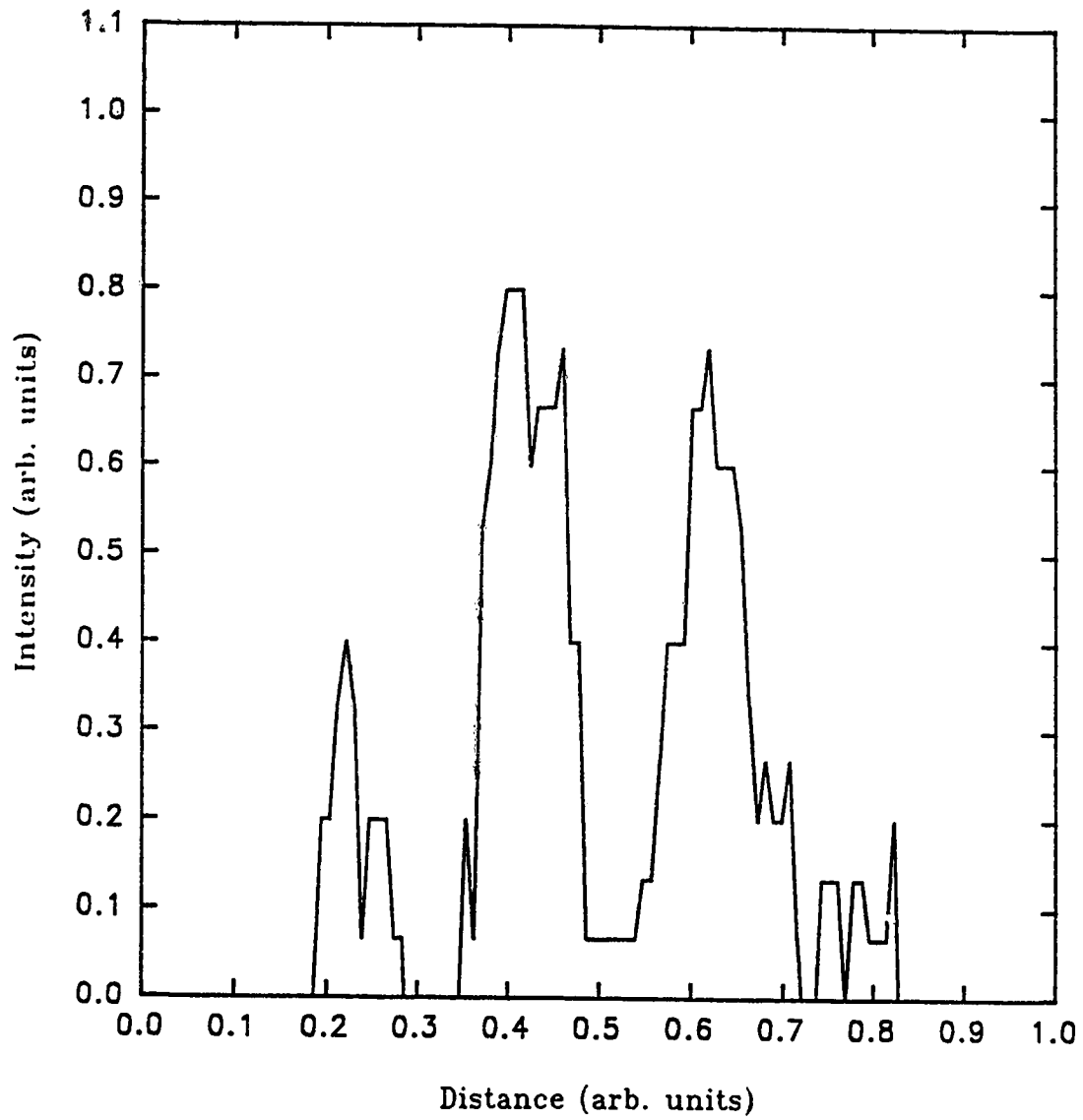


Figure 5.4 Typical Intensity Profile of the Observed Interference Fringes With an Externally Injected Beam



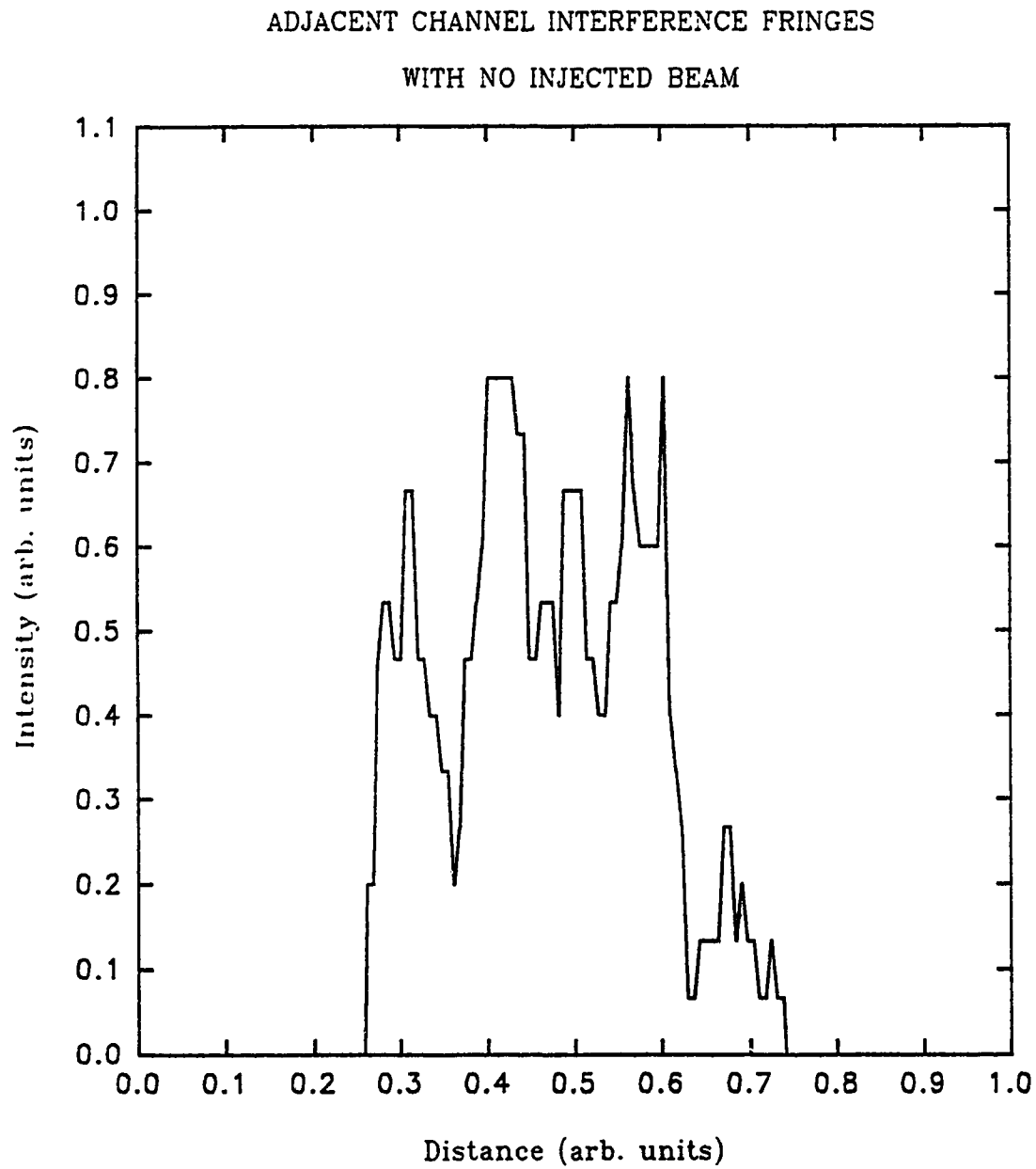


Figure 5.5 Typical Intensity Profile of the Observed Interference Fringes Without an Externally Injected Beam

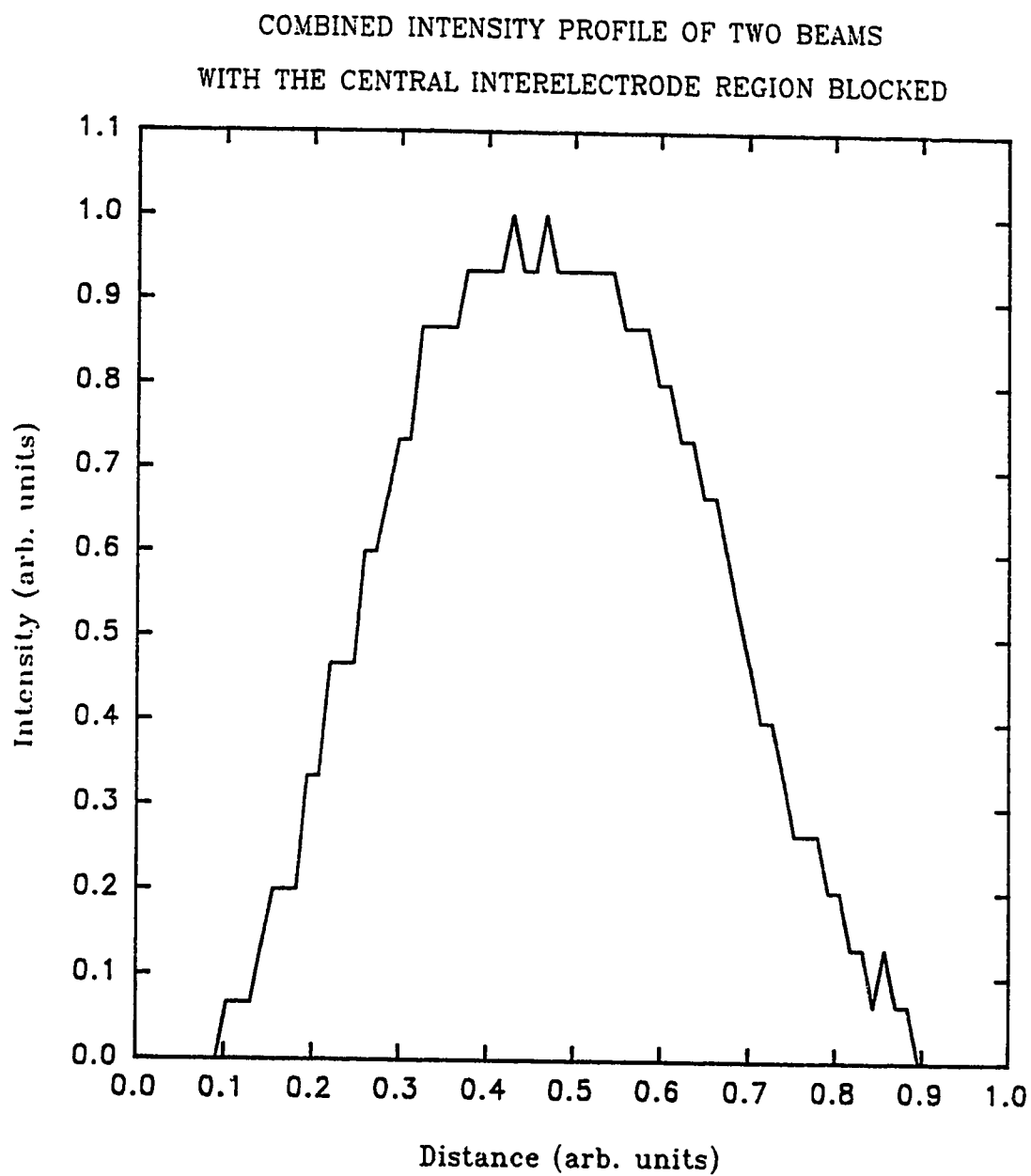


Figure 5.6 Typical Intensity Profile for Two Overlapping Output Beams With the Central Interelectrode Region Blocked

### 5.2.3 Far-Field Experiments

Further to the near-field interference tests that were just outlined, measurements were also made in the far-field in an effort to determine the increase in intensity and the associated reduction in focal spot size that was anticipated. Unfortunately, both of these experiments were inconclusive with all combinations of output beams examined. In retrospect, this result should have been expected due to the extreme sensitivity of the alignment tolerances involved. Previous investigators have documented that the far-field alignment required an accuracy of  $\approx \lambda/30$  or better in path length, with optical elements aligned to within  $\approx 10 \mu\text{rad}$  in tilt angles.<sup>112,115,153</sup> In all of these instances, the attainment of an optimized near-field interference pattern was the first step in a coarse alignment procedure to observe the far-field intensity enhancement. Regrettably, a vibration-isolated optical table was not available for these experiments, and an optimistic estimate of the angular alignment ability for the apparatus used was  $\pm 5 \text{ mrad}$ . Therefore, any observation of the far-field-related phase-locking properties would have been highly fortuitous.

### 5.3 Analysis of the Phase-Locking Results

The results presented above are very encouraging since they demonstrate that there was a significant degree of phase-locking even when the injection beam was not present. Furthermore, there were also two other trends that were observed from this data. First, the amount of phase-locking was found to be greater in all cases with the injected beam than without it. The second tendency was that the opposite channels exhibited the highest degree of locking, and the orthogonal pairs the lowest, with only one exception to this pattern.

The fact that the injected signal experiments produced greater visibilities was not unexpected. By initiating a seed signal into each channel, some degree of coherence was expected since part of this source beam was aligned to traverse each of the discharge slots. Any locking that occurred because of the injected beam was in addition to that which was already occurring in the device from its own self-phase-locking. However, of greater importance was the fact that injecting did not produce the same effect in all of the channel

combinations that were investigated.

The observed discrepancies in the visibility from the different channel pairs was undoubtedly caused by the alignment of the injection beam into the slots themselves. Although care was exercised to align the beam as well as possible, inevitably some channels would have received more injection signal than others did. This factor could easily account for the disparities in observed visibilities. Also, the fact that the adjacent channels produced the greatest visibility most likely indicated that those two slots were fed the largest amount of the injection beam. This would partially explain why 100 % phase-locking was not found for any of the channel combinations. In order to achieve the maximum degree of coupling between the injected signal and the slave cavities, the two must be optically mode matched together.<sup>119,246</sup> This mode matching is usually accomplished by arranging for the radius of curvature of the injected beam to be identical to that of the mirror that it impinges on for its first reflection. In this manner, the injected beam's mode optimally matches the natural mode of the cavity for phase-locking to occur. Unfortunately, it was not possible to perform this experiment within this present investigation. This was primarily caused by the inability to achieve a perfect alignment of the injected beam into the multichannel system since the one end of the device was totally enclosed and thereby not usable for alignment purposes.

The differences in the visibilities measured for the self-phase-locking experiments were related to another phenomenon. The Fresnel-Arago laws of interference state that two coherent but orthogonally polarized beams will not produce any interference fringes due to the fact that the cross-term  $I_{1,2}$  in equation (5.1) is equal to zero in this situation.<sup>238</sup> As was discussed in Chapter 4, the polarization of each of the channels was random with this particular optical resonator, but was dominated by a stronger component in the direction parallel to each of the electrode faces within each slot. Therefore, only smaller fractions of the total power in any pair of channels that was selected for the interference experiments was polarized in a similar direction. This amount increased to a maximum for opposite channels and was a minimum for those slots that were perpendicular to each other.

The mechanism responsible for this self-phase-locking feature was clearly related to the central inter-electrode region of the laser geometry. This was demonstrated by the total absence of any interference fringes when the central region of the device was blocked with a ceramic disc. As was alluded to in the previous chapter, there were two processes taking place simultaneously in this central zone. There was the independent lasing due to the gain present in that area, as well as the converging optical wave which was produced from within each individual channel. Either of these properties could have independently caused the required optical beam coupling necessary to achieve phase-locking. Alternatively, both methods could have been working together in concert to produce these results.

Unstable resonators are commonly thought of as consisting of two regions: a central core-oscillator section, surrounded by an outer amplification region.<sup>247,248</sup> The central oscillator region is an area of very strong diffractive cross-coupling and the fundamental resonator mode is established in this core-oscillator zone. The remainder of the resonator simply acts as an amplifier that is fed from this central area. In this manner, it is clear that either of the two mechanisms described above can take advantage of this property to establish phase-locking within the multichannel array. First, the converging waves can walk into the central oscillator region from all of the separate channels. Once in this zone, strong diffractive coupling occurs amongst the entire set of beams with the possibility that a common optical mode results from the interaction. This common mode then proceeds to expand radially outward from the central region and thereby seeds all of the separate discharge channels. The independent lasing observed in the central portion of the structure can act in a similar fashion. Once lasing has been established in the central region, this area then functions as the core-oscillator and so provides the necessary optical feed into all channels.

Although, as of this time, a conclusive experiment has not been performed, it is felt that the lasing in the central region was the primary source of the phase-locking. This follows from the fact that when the central region was blocked off, the polarization in the individual channels reverted from random to linear. Therefore, taking into account the Fresnel-Arago laws, it is known that no interference, and hence no phase-locking, occurred under these

circumstances. In a similar vein, the converging wave would always have the same polarization as the fundamental mode that has already been established within its own particular slot. Therefore, if each slot has predominately chosen the linear polarization direction, even after interacting in the central zone, the converging wave and its progeny will still be linearly polarized in that same direction. As such, the converging wave would be incapable of exhibiting any phase-locking effects.

Conversely, when the central region establishes independent lasing, it is randomly polarized. Therefore, each slot was seeded with all orientations of polarization and phase-locking between channels was indeed possible. Moreover, once this process has been established, there would be nothing to preclude the reverse wave from enhancing the phase-locking properties, since it would now be composed of all polarization orientations.

In summary, partial phase-locking of the individual channels of a multichannel laser array has been demonstrated. Phase-locking percentages as high as 62 % without any injection seeding and 91 % with an injected beam have been observed. The mechanism responsible for this phase-locking feature was identified to be the optical coupling provided by independent lasing within the central electrode-free region of the laser structure. Forseeably, if this central region could be modified to exhibit higher gain, then the core-oscillator injection phenomenon may be sufficient to provide near 100 % self-phase-locking for all channels. Notwithstanding the above, these experiments have clearly demonstrated that the multichannel laser array concept is viable as a means of providing compact yet high power laser systems for many varied applications.

## CHAPTER 6

### SHEET METAL CUTTING EXPERIMENTS

The preceding chapters of this thesis have documented the design and characterization of a compact, multichannel, extended-area electrode laser array. These chapters have focused primarily on the device properties and the nature of the optical output beams. This chapter is presented as an illustration of the potential of this type of laser in a materials processing application.

#### 6.1 Introduction to Laser Materials Processing

Lasers have been employed in materials processing since the late 1960's<sup>249</sup> and their uses have gradually increased as newer processing techniques and advances in laser technology have unfolded.<sup>12,15</sup> There are numerous advantages to using a laser for materials processing, some of which are:<sup>250-252</sup> ease of controlling the machining process; little or no post-process machining required due to the non-contact nature of the interaction; no machine tool wear; reliable selectability of the workpiece interaction area allows complex component shapes to be handled; and little or no pre-process surface treatment is required.

Processing with lasers has enjoyed a renewed interest in the past several years, which has particularly been spurred on by the development of compact, lightweight, efficient and reliable laser systems. Foremost of these advances has been the realization that diffusion-cooled, RF-excited, CO<sub>2</sub> laser devices may be scaled in proportion to the electrode area, as opposed to just the discharge length.<sup>17,44</sup> This has led to the development of several slab discharge structures<sup>17,44,53,73,81</sup>, and also to the stacking of numerous extended-area discharge slots into multichannel radial arrays.<sup>165,253-254</sup>

Of primary importance to materials processing applications are the output power, intensity of the beam, beam quality, and the beam polarization properties.<sup>89</sup> While the aforementioned slab lasers have produced sufficient levels of output power and intensity to be capable of various processing tasks, they have usually suffered from poor beam quality or

undesirable polarization properties. These devices have typically employed a hybrid stable-unstable resonator which produces an astigmatic output beam.<sup>53,77,79</sup> These resonators have the tendency to produce a line focus as opposed to the preferential circular spot used for processing requirements. Furthermore, because of their waveguide nature, most slab laser devices produce output beams that are linearly polarized.<sup>18,53</sup> These properties, combined with the line focusing characteristics, imply that materials processing with these systems will be highly directionally dependent.<sup>232</sup> Much more desirable, from the materials processing perspective, is a beam which exhibits a circular focal spot distribution and is either randomly or circularly polarized.<sup>8,233</sup>

This chapter presents the results of sheet metal cutting experiments which were performed with a multichannel laser array system. This system has been shown to possess the characteristics of the previously mentioned slab lasers, plus the additional benefits of good beam quality and a desirable output polarization state.

## 6.2 Experimental Apparatus and Techniques

The experimental arrangement used for these tests is shown as a block diagram in Figure 6.1. For all experiments, the multichannel laser structure was fitted with a toric confocal unstable resonator having a magnification of 1.16 and an output coupling aperture of 2.16 cm. This particular resonator produced an annular output beam with a polarization state that was the superposition of the polarizations within each of the individual channels. The properties of this resonator have been described in greater detail in Chapter 4. A 1:1:3 = CO<sub>2</sub>:He:He gas mixture at a total gas pressure of 20 Torr was used throughout. An RF input power level of 3 kW was used to excite the discharge, and this resulted in an optical output of 200 W.

After emerging from the laser structure, the output beam was focused with a 2.5 cm diameter, 6.35 cm focal length NaCl lens. This lens, coupled with the above described output beam, corresponded to an  $f/\# \approx 13$  for this optical system. The 1/e<sup>2</sup> focal spot size of this combination was measured with the aid of the BeamScan LBA 1/A beam analyzer and was



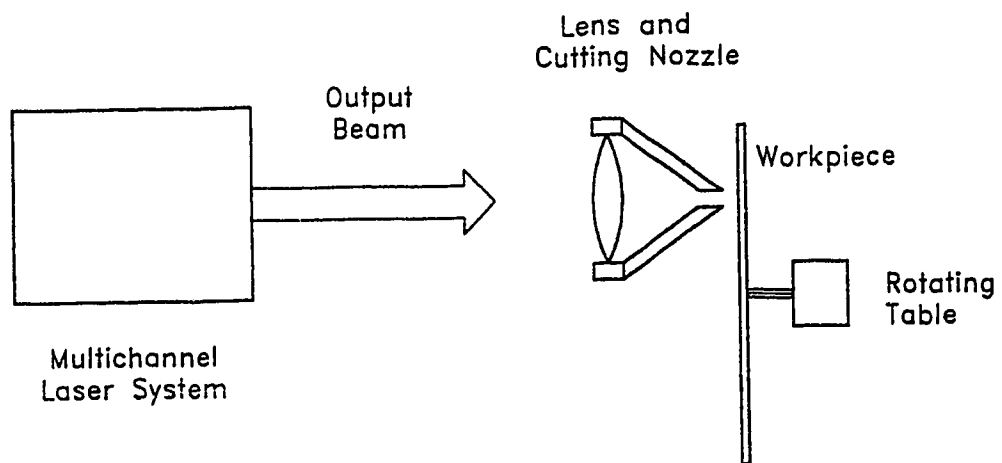


Figure 6.1 Block Diagram of the Laser Cutting Apparatus

found to be  $\approx 500 \mu\text{m}$  in both the x and y component directions. This lens was mounted to an adjustable optical holder to allow for proper positioning relative to the workpiece.

An adjustable cutting nozzle was also attached to the lens holder. This nozzle was tapered from the diameter of the lens down to an  $\approx 2 \text{ mm}$  hole, which allowed the now focused beam to exit. Provisions were made on this apparatus to permit the use of a cover gas assist during the cutting process. The use of high pressure cover gas serves a dual purpose. First, by a judicious choice of the cover gas composition, the overall cutting performance and quality may be enhanced through the creation of an exothermal reaction at the workpiece.<sup>9</sup> The second reason for the cutting nozzle/cover gas combination is to protect the delicate optical elements from any material backsplatter that may occur during the process interaction. For all of the cutting experiments performed herein, an oxygen cover gas was employed at a pressure of 345 kPa.

The workpiece was mounted onto a rotating turntable arrangement that was subsequently attached to an optical rail. This rotating table was driven by a variable speed motor which therefore allowed cutting to be performed over a range of process speeds. The workpiece itself was chosen to be mild steel of various thicknesses. The only preparation that was done to each workpiece was a light sandblasting to reduce the material's surface reflectivity.

### 6.3 Cutting Performance and Discussion

Mild steel cutting was performed for a range of material thicknesses at a fixed laser output power level of 200 W. In general, it was found that the cut quality was very good. The majority of the cuts were of the Class III type, according to Arata's<sup>8</sup> classification scheme. This class of cut is characterized by relatively parallel and smooth side walls, which are also essentially dross free. The typical kerf width formed during these cuts was  $\approx 600 \mu\text{m}$ , and the heat affected zone on each side of the kerf ranged from  $\approx 320 - 450 \mu\text{m}$ . The width of this zone was estimated by observing the discoloration of the material surface.

Figure 6.2 shows a graph of the maximum cutting speed achieved for various material thicknesses. The maximum speed was defined to be that which still produced a Class III cut. Cutting was still possible at speeds above those shown here however, the cuts were sporadic and had rougher edges with considerably more dross clinging to the workpiece. At speeds significantly lower than those shown, the cut had a much wider kerf width which was on the order of 2 - 3 mm. This was indicative of a Class I type of cut, which was typically the result of too slow of a processing speed that allowed for material self-burning.<sup>8</sup>

The results presented in Figure 6.2 are in good agreement with those of other investigators.<sup>9,53</sup> As a specific example, Yatsiv *et al.*<sup>255</sup> have reported a maximum cutting speed of 200 cm/min for 0.8 mm mild steel with 200 W of laser power.

One final aspect of the cutting capability of the multichannel laser structure was explored. This property was the cutting speed in various directions. As mentioned in the introductory section of this chapter, materials processing with lasers can be highly directionally dependent, a characteristic that is related to the polarization of the output beam. To examine this, cuts were made in several directions by having the focused beam positioned at different points on the rotating workpiece. It was found that, irrespective of the cutting direction or the material thickness, the maximum speed was the same in all cases. This result was undoubtedly caused by the polarization state of the toric resonator's output beam, which has been shown to be the superposition of the individual channel polarizations. This trait is a very beneficial aspect of the multichannel laser system with respect to materials processing applications.

The results of this chapter have successfully demonstrated the use of a multichannel, extended-area electrode, carbon dioxide laser array for sheet metal cutting applications. Specifically, this unoptimized structure was found to exhibit multi-directional cutting ability at the same processing speed, in addition to performance levels comparable to existing commercial laser systems. This compact and lightweight structure, which contains no moving parts, could easily be mounted onto a robot arm for even greater materials processing flexibility. Moreover, the use of an optical resonator system that produced a phase-locked

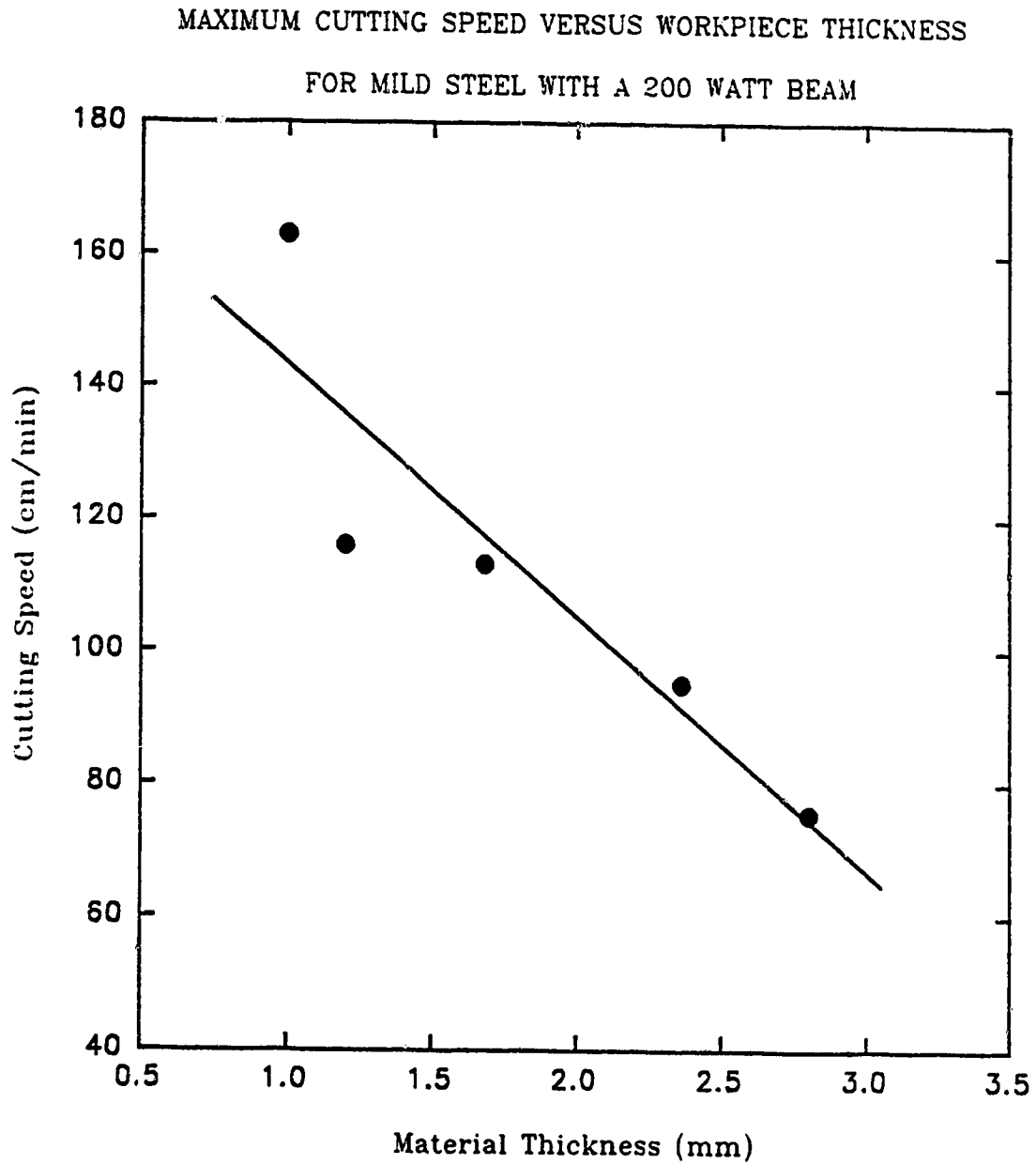


Figure 6.2 Variation in the Maximum Cutting Speed for Different Thicknesses of Mild Steel

output beam, plus the increased cutting speed and quality that could be achieved with a lower  $f/\#$  optical system, further indicate the attractiveness of this type of laser device to the industrial laser community.

## CHAPTER 7

### CONCLUSIONS AND PROPOSALS FOR FUTURE RESEARCH

#### 7.1 Summary of this Investigation

Results presented in this thesis have demonstrated the viability of the extended-area electrode, multichannel, radial array, carbon dioxide laser concept.

The initial experiments performed in the multichannel discharge structure illustrated that a stable,  $\alpha$ -type gas discharge could be simultaneously maintained in each of the inter-electrode volumes. It was found that a wide variety of gas mixtures and pressures could be employed in the system at specific power loading levels as high as  $10 \text{ W/cm}^2$ .

Subsequent gain and saturation intensity parameter measurements indicated that this discharge structure had the potential for laser operation. The gain was confirmed to be comparable in all of the system channels, and had a value that corresponded well with other devices of similar construction. Furthermore, a significant amount of gain was detected in the central inter-electrode region of the discharge structure. This gain was the manifestation of vibrationally excited  $\text{CO}_2$  molecules diffusing into that zone. It was subsequently shown that the gain available in this area profoundly influenced the phase-locking ability of the laser array. Saturation intensity measurements were also encouraging and found to vary in proportion to the square of the total gas pressure, as had been indicated by previous theoretical and experimental investigations.

The nature of the optical output radiation was also characterized. Several different optical resonators were fitted to the multichannel laser array and a comparison made of their individual properties. Included in these studies was a conventional unstable resonator design and a unique toric unstable optical resonator configuration.

Results indicated that any of the resonators examined herein performed adequately however, each of the resonators possessed some unique attributes that proved to be advantageous under certain circumstances. For example, the toric resonators produced an

output beam that emerged near the centerline of the discharge structure, whereas the conventional resonators yielded output radiation from the outer edge of the mirrors. It was determined that the output coupling aperture size in the convex mirror of the toric resonators greatly modified the nature of the output from these resonators. By a judicious choice of aperture size, the output beam could be made to emerge as a single spot, a uniform annulus, or as eight distinct beamlets. In general it was found that the toric resonator designs produced higher output power levels than did the corresponding conventional unstable configurations, as well as being less sensitive to misalignments in the optical system itself.

The far-field properties of the various resonators were also investigated and it was shown that the conventional resonators produced the smallest focal spot sizes. Measurements of the output beam polarization indicated that the toric systems exhibited linear polarization when the beamlets were separate and distinct, but showed a superposition of the constituent beam polarizations in all other output radiation profiles. Conversely, the conventional unstable resonators displayed random polarization properties, unless the central inter-electrode region was blocked off, in which case the polarization then reverted to a linear state within each slot.

Independent lasing ability was also witnessed from the central inter-electrode region. This lasing was later found to have a profound influence on the phase-locking ability of the individual channels of the structure.

In an effort to assess the suitability of the multichannel laser array for phase-locking, several experiments were performed to demonstrate this property. Initial studies using a low power injected beam as a seeding source indicated that coherent operation of the individual slots was indeed possible, and phase-locking as high as 91 % was observed between various channels. Further analysis, with the injection beam removed, revealed that a certain degree of self-phase-locking was occurring within the device. This locking ranged from 22 to 62 %. The mechanism responsible for this locking was identified to be the optical coupling of the channels within the central inter-electrode region. In an unstable resonator, this region acts as the core-oscillator which then feeds the outer amplification regions of the resonator with a

fundamental optical mode. Elimination of this zone was found to remove all indications of phase-locking from the system.

Finally, mild steel cutting was performed as a demonstration of the multichannel laser array's ability to perform materials processing tasks. Performance comparable to that of presently available commercial systems was achieved, with the additional capability of having the process speed uniform in all directions. This last aspect was attributed to the unique output beam polarization produced by the toric unstable resonator.

## 7.2 Proposals for Future Research

There are several interesting aspects of this research project which may warrant further detailed investigation. This section briefly outlines some of these recommended areas.

A study should be undertaken to conclusively identify the mechanism responsible for self-phase-locking. As was discussed in Chapter 5, there were two processes that were likely candidates to establish phase-locking: the converging wave phenomenon of unstable resonator beam propagation, and the independent lasing of the central inter-electrode region. Other investigators have identified a few techniques by which the converging wave may be partially, or entirely, suppressed; some of which include: <sup>239,256-257</sup> graded reflectivity mirrors, soft-edged resonators, and serrated edged mirrors. Once the converging wave has been removed, any indication of phase-locking would have to be caused by the central region lasing independently.

Conversely, if phase-locking was not observed, or it was reduced, then the converging wave has been established as one of the fundamental factors involved. If this is the case, there are methods that have been proposed to enhance the intensity of the reverse travelling wave. For instance, it was shown that by placing an additional reflective surface, either internal to or external to the resonator, the converging wave intensity could be increased. <sup>240,258-259</sup> Once the mechanism that provides the phase-locking is better understood, the optimization of this aspect of the system may be carried out.



In a related investigation, enhancement of the gain in the central inter-electrode region may also increase the amount of phase-locking within the entire system. This is based on the fact that this region was found to possess only  $\approx 25\%$  of the gain found in the electrode gap volumes, yet self-phase-locking still occurred. Two modifications are possible to the electrode assembly that may accomplish this goal. First, the tips of the electrodes could be made sharp rather than rounded-off, as they were in this study. This would increase the fringing electric field strength at the ends of the electrodes closest to the central region, and in turn, more upper laser level excitation may thus occur in that area. A second method would be to make larger aspect ratio electrodes so that the distance between the tips of opposite electrodes was almost as small as the inter-electrode gap. This would increase the gain observed in the central region because the vibrationally excited  $\text{CO}_2$  molecules would have a significantly reduced volume into which they would diffuse; therefore the density of excited species would be much nearer to that in the active discharge regions.

There are also several other optical resonator systems that would be of interest to examine with this multichannel laser structure. Among them is a toric resonator that has different radii of curvature in both directions of the electrode slot region.<sup>260</sup> With this type of a design, the magnification and the other resonator properties could be independently varied in each dimension to achieve the optimal performance from the device.

Another interesting optical structure is one that employs a conical mirror as part of the resonator itself. Recent studies have indicated that such a design has the potential to double the optical energy extraction from a laser system through a pseudo-phase conjugation technique.<sup>261</sup> Other investigations have also suggested the possibility of achieving phase-locking through the optical cross-coupling experienced within a conical resonator.<sup>262</sup>

Finally, a whole range of experiments could be performed to optimize the discharge conditions themselves. It is known that there is an optimum frequency, gap size, gas mixture and pressure, etc. for any given discharge structure. A systematic exploration of these and other discharge parameters would result in the attainment of an optimum discharge device for  $\text{CO}_2$  laser excitation.

In conclusion, the extended-area, multichannel laser array concept has been shown to be a viable approach for carbon dioxide laser development. Through the judicious choice of an unstable optical resonator, up to 62 % self-phase-locking between the individual channels of the array was demonstrated. Although nonoptimized, the system performed admirably during laser materials processing applications. A similar system, based on the concepts developed herein, could conceivably yield a multikilowatt carbon dioxide laser in a very small and lightweight physical package, thus ushering in a new generation of compact and high power laser devices.

## REFERENCES

1. C.K.N. Patel, *Interpretation of CO<sub>2</sub> optical maser experiments*, Phys. Rev. Lett., 21, 5b8, (1964).
2. C.K.N. Patel, *Selective excitation through vibrational energy transfer and optical maser action in N<sub>2</sub>-CO<sub>2</sub>*, Phys. Rev. Lett., 13, 617, (1964).
3. W.J. Witteman, *The CO<sub>2</sub> Laser*, Springer Series in Optical Sciences 53, (Springer-Verlag, Berlin, 1987).
4. M.W. Patchan, *Medical applications call for selectivity in laser performance*, Laser Focus World, 27, 85, (1991).
5. D.A. Belforte, *Industrial lasers move up the power curve*, Laser Focus World, 27, 69, (1991).
6. G.A. Baranov and V.V. Khukharev, *Soviet CO<sub>2</sub> laser separates carbon isotopes*, Laser Focus World, 27, 127, (1991).
7. R. Walker, *Applying multikilowatt CO<sub>2</sub> lasers in industry*, Lasers and Applications, 61, (1984).
8. Y. Arata, *Plasma, Electron and Laser Beam Technology*, (American Society of Metals, Metals Park, Ohio, 1986).
9. M. Bass, editor *Laser Materials Processing*, (North-Holland, Amsterdam, 1983).
10. V.E. Merchant, *Development of a new 20 kW CO<sub>2</sub> laser*, Laser Focus, 21, (1985).
11. *The Laser's Edge*, United Technologies Industrial Lasers Newsletter, March, (1992).
12. L. Garifo and A. Sona, *The state of the art and the trends in high power CO<sub>2</sub> lasers for materials processing*, High Power Lasers and Their Industrial Applications, D. Schuocker, editor, Proc. SPIE 650, 47, (1986).
13. A.P. Schwarzenbach and U.W. Hunziker, *Industrial CO<sub>2</sub> laser with high overall efficiency*, High Power CO<sub>2</sub> Lasers Systems and Applications, A. Quenzer, editor, Proc. SPIE 1020, 43, (1989).

14. R.P. Main, *RF-excited industrial carbon dioxide lasers: the user's viewpoint*, Seventh International Symposium on Gas Flow and Chemical Lasers, D. Schuocker, editor, Proc. SPIE 1031, 68, (1989).
15. G. Herziger and E.W. Kreutz, *Trends in materials processing with laser radiation*, Beam Diagnostics and Beam Handling Systems, A. Sona, editor, Proc. SPIE 1024, 2, (1989).
16. P. Laakmann, *Laser arrays boost output powers*, Laser Focus World, 27, 123, (1991).
17. D.R. Hall and H.J. Baker, *Area scaling boost CO<sub>2</sub>-laser performance*, Laser Focus World, 25, 77, (1989).
18. A.W. Mitchell, *A radio frequency carbon dioxide slab laser*, MSc Thesis, University of Alberta, (1990).
19. A.J. DeMaria, *Review of cw high-power CO<sub>2</sub> lasers*, Proc. IEEE, 61, 731, (1973).
20. G. Moeller and J.D. Rigden, *High-power laser action in CO<sub>2</sub>-He mixtures*, Appl. Phys. Lett., 7, 274, (1965).
21. C.K.N. Patel, P.K. Tien and J.H. McFee, *CW high-power CO<sub>2</sub>-N<sub>2</sub>-He laser*, Appl. Phys. Lett., 7, 290, (1965).
22. T.J. Bridges and C.K.N. Patel, *High-power Brewster window for 10.6 microns*, Appl. Phys. Lett., 7, 244, (1965).
23. M.W. Sasnett, *Comparing industrial CO<sub>2</sub> lasers*, Lasers and Applications, 85, (1984).
24. P.A. Miles and J.W. Lotus, *A high-power CO<sub>2</sub> laser radar transmitter*, IEEE J. Quantum Electron., QE-4, 811, (1968).
25. P.K. Cheo, *Effects of gas flow on gain of 10.6 micron CO<sub>2</sub> laser amplifiers*, IEEE J. Quantum Electron., QE-3, 683, (1967).
26. W.B. Tiffany, R. Tang and J.D. Foster, *Kilowatt CO<sub>2</sub> gas transport laser*, Appl. Phys. Lett., 15, 91, (1969).
27. T.F. Deutsch, F.A. Harrigan and R.I. Rudko, *CW operation of high pressure flowing CO<sub>2</sub> lasers*, Appl. Phys. Lett., 15, 88, (1969).
28. S.L. Ream, *Present and future acceptance of high power CO<sub>2</sub> lasers*, Laser Focus, 18, (1982).

29. J.T. Verdeyen, *Laser Electronics*, (Prentice-Hall, New Jersey, 1981).
30. B.E. Cherrington, *Gaseous Electronics and Gas Lasers*, (Pergamon Press, Oxford, 1979).
31. H.J.J. Seguin and J. Tulip, *Photoinitiated and photosustained laser*, Appl. Phys. Lett., 21, 414, (1972).
32. O.P. Judd, *An efficient electric CO<sub>2</sub> laser using preionization by UV radiation*, Appl. Phys. Lett., 22, 95, (1973).
33. M. Richardson, A.J. Alcock, K. Leopold and P. Burtyn, *A 300-J multigigawatt CO<sub>2</sub> laser*, IEEE J. Quantum Electron., QE-9, 236, (1973).
34. H.J.J. Seguin, K.H. Nam and J. Tulip, *The photoinitiated impulse-enhanced electrically excited (PIE) discharge for high-power cw laser applications*, Appl. Phys. Lett., 32, 418, (1978).
35. K.H. Nam, H.J.J. Seguin and J. Tulip, *Operational characteristics of a PIE CO<sub>2</sub> laser*, IEEE J. Quantum Electron., QE-15, 44, (1979).
36. A. Crocker and M.S. Wills, *Carbon-dioxide laser with high power per unit length*, Electron. Lett., 5, 63, (1969).
37. O.B. Nichols and W.M. Brandenburg, *Radio-frequency preionization in a supersonic transverse electrical discharge laser*, IEEE J. Quantum Electron., QE-8, 718, (1972).
38. C.O. Brown and J.W. Davis, *Closed-cycle performance of a high-power electric-discharge laser*, Appl. Phys. Lett., 21, 480, (1972).
39. P. Hoffmann, *Discharge behaviour of a RF excited high power CO<sub>2</sub> laser at different excitation frequencies*, High Power Lasers and Their Industrial Applications, D. Schuocker, editor, Proc. SPIE 650, 23, (1986).
40. R.A. Hart, L.A. Newman, A.J. Cantor and J.T. Kennedy, *Staggered hollow-bore CO<sub>2</sub> waveguide laser array*, Appl. Phys. Lett., 51, 1057, (1987).
41. A. Sona, *RF and DC excited high power CO<sub>2</sub> lasers*, High Power Lasers: Sources, Laser-Material Interactions, High Excitations, and Fast Dynamics in Laser Processing and Industrial Applications, E.W. Kreutz, A. Quenzer, D. Schuocker, editors, Proc. SPIE 801, 23, (1987).
42. H. Hugel, *RF excited CO<sub>2</sub> flow lasers*, Gas Flow and Chemical Lasers, 1984, Proc. of the Fifth International Symposium, B. Walter, D. Schuocker, editors, (Adam Hilger, Bristol,

England, 1984).

43. W. Schock, A. Giesen, Th. Hall, W. Wittwer, H. Hugel, *Transverse radio frequency discharge: a promising excitation technique for high power CO<sub>2</sub> lasers*, Laser Processing: Fundamentals, Applications, and Systems Engineering, W.W. Duley, R. Weeks, editors, Proc. SPIE 668, 246, (1986).
44. S. Yatsiv, *Conductively cooled capacitively coupled RF excited CO<sub>2</sub> lasers*, Gas Flow and Chemical Lasers, 1986, Proc. of the Sixth International Symposium, B. Walter, D. Schuocker, editors, (Adam Hilger, Bristol, England, 1986), p. 252.
45. S.M.A. Durrani, *Optimization of RF discharges for excitation of CO<sub>2</sub> lasers*, PhD thesis, Heriot-Watt University, (1988).
46. H.J. Baker and I. Laidler, *Electrical characterisation of pulsed and cw fast axial flow RF excited CO<sub>2</sub> lasers*, High-Power Gas Lasers, P.V. Avizonis, C. Freed, J.J. Kim, F.K. Tittel, editors, Proc. SPIE 1225, 349, (1990).
47. W. Schock, Th. Hall, E. Wildermuth, K. Wessel, E. Gehringer, P. Schnee, F. Hadinger, *Compact transverse flow CO<sub>2</sub> laser with RF excitation*, Seventh International Symposium on Gas Flow and Chemical Lasers, D. Schuocker, editor, Proc. SPIE 1031, 76, (1989).
48. B. Walter, M. Bohrer, D. Schuocker, *RF-excited-CO<sub>2</sub>-laser with improved electrode geometry*, High Power Lasers and Laser Machining Technology, M.L. Gaillard, A. Quenzer, editors, Proc. SPIE 1132, 14, (1989).
49. L.A. Newman and R.A. Hart, *Technology trends in low- to medium-power CO<sub>2</sub> lasers*, New Developments and Applications in Gas Lasers, L.R. Carlson, editor, Proc. SPIE 737, 36, (1987).
50. C.J. Walsh, *An rf excited circular waveguide CO<sub>2</sub> laser*, Rev. Sci. Instrum., 61, 2309, (1990).
51. B. Walter, *A new concept of an rf-excited CO<sub>2</sub>-laser with solid state generators*, Seventh International Symposium on Gas Flow and Chemical Lasers, D. Schuocker, editor, Proc. SPIE 1031, 82, (1989).
52. W. Schock, B. Walz, K. Wessel, E. Wildermuth, *Characteristics of a compact rf excited 12 kW CO<sub>2</sub>-laser*, CO<sub>2</sub> Lasers and Applications II, H. Opower, editor, Proc. SPIE 1276, 41, (1990).
53. R. Nowack, H. Opower, U. Schaefer, K. Wessel, Th. Hall, H. Kruger, H. Weber, *High power CO<sub>2</sub> waveguide laser of the 1 kW category*, CO<sub>2</sub> Lasers and Applications II, H. Opower, editor, Proc. SPIE 1276, 18, (1990).

54. V.A. Svich, V.M. Tkachenko and A.N. Topkov, *Waveguide coaxial rf-excited CO<sub>2</sub> laser*, Sov. J. Quantum Electron., 20, 612, (1990).
55. J.G. Xin, P. Yan and G.H. Wei, *rf-excited all-metal waveguide CO<sub>2</sub> laser*, Appl. Phys. Lett., 59, 3363, (1991).
56. A.G. Gerasimchuk, S.T. Kornilov, E.D. Protsenko, S.I. Tymper, *Waveguide CO laser with high-frequency excitation*, Sov. J. Quantum Electron., 15, 1181, (1985).
57. M. Surenda, D.B. Graves, I.J. Morey, *Electron heating in low-pressure rf glow discharges*, Appl. Phys. Lett., 56, 1022, (1990).
58. T. Ledig and B. Schroder, *Electron energy distribution functions and power transfer data for radio-frequency discharges in CO<sub>2</sub> laser gas mixtures*, J. Phys. D: Appl. Phys., 23, 1624, (1990).
59. K. Schroder, *Theoretical treatment of rf discharges in CO<sub>2</sub> waveguide lasers*, J. Appl. Phys., 68, 5528, (1990).
60. Ph. Belenguer and J.P. Boeuf, *Transition between different regimes of rf glow discharges*, Phys. Rev. A, 41, 4447, (1990).
61. R. Wester, S. Seiwert and R. Wagner, *Theoretical and experimental investigations of the filamentation of high-frequency excited CO<sub>2</sub> laser discharges*, J. Phys. D: Appl. Phys., 24, 1796, (1991).
62. T.J. Sommerer and M.J. Kushner, *Numerical investigation of the kinetics and chemistry of rf glow discharge plasmas sustained in He, N<sub>2</sub>, O<sub>2</sub>, He/N<sub>2</sub>/O<sub>2</sub>, He/CF<sub>4</sub>/O<sub>2</sub> and SiH<sub>4</sub>/NH<sub>3</sub> using a Monte-Carlo-fluid hybrid model*, J. Appl. Phys., 71, 1654, (1992).
63. R. Wester and S. Seiwert, *Numerical modelling of RF excited CO<sub>2</sub> laser discharges*, J. Phys. D: Appl. Phys., 24, 1371, (1991).
64. A. Garscadden, M.J. Kushner and J.G. Eden, *Plasma physics issues in gas discharge laser development*, IEEE Trans. on Plasma Sci., 19, 1013, (1991).
65. K. Schroder, *Theoretical modelling of RF-excited laser plasmas*, Seventh International Symposium on Gas Flow and Chemical Lasers, D. Schuocker, editor, Proc. SPIE 1031, 90, (1989).
66. D. He, C.J. Baker and D.R. Hall, *Discharge striations in rf excited waveguide lasers*, J. Appl. Phys., 55, 4120, (1984).

67. D.R. Hall and C.A. Hill, *Radio frequency-discharge-excited CO<sub>2</sub> lasers*, Handbook of Molecular Lasers, P.K. Cheo, editor, (Marcel Dekker, New York, 1987).
68. H.E. Hugel, *RF excitation of high power CO<sub>2</sub> lasers*, High Power Lasers and Their Industrial Applications (1986), D. Schuocker, editor, Proc. SPIE 650, 2, (1986).
69. W.L. Wiegand, *Causes of thermal instability in externally sustained molecular discharges*, Phys. Rev. A, 15, 1701, (1977).
70. S.M. Levitskii, *An investigation of the breakdown potential of a high frequency plasma in the frequency and pressure transition regions*, Sov. Phys. Tech. Phys., 2, 887, (1957).
71. P. Vidaud, S.M.A. Durrani and D.R. Hall, *Alpha and gamma RF capacitive discharges in N<sub>2</sub> at intermediate pressures*, J. Phys. D: Appl. Phys., 21, 57, (1988).
72. D. He and D.R. Hall, *Frequency dependence in RF discharge excited waveguide CO<sub>2</sub> lasers*, IEEE J. Quantum Electron., QE-20, 509, (1984).
73. A. Gabai, R. Hartzberg and S. Yatsiv, *Radio-frequency excited stripline CO and CO<sub>2</sub> lasers*, Conference on Lasers and Electro-Optics, paper TUB4, (1984).
74. D.R. Hall and H.J. Baker, *RF excitation of diffusion cooled and fast axial flow lasers*, Seventh International Symposium on Gas Flow and Chemical Lasers, D. Schuocker, editor, Proc. SPIE 1031, 60, (1989).
75. X.S. Zhang, H.J. Baker and D.R. Hall, *Large area discharge rf excited CO<sub>2</sub> laser*, Conference on Lasers and Electro-Optics, paper THG2, (1989).
76. K.M. Abramski, A.D. Colley, H.J. Baker and D.R. Hall, *Power scaling of large-area transverse radio frequency discharge CO<sub>2</sub> lasers*, Appl. Phys. Lett., 54, 1833, (1989).
77. P.E. Jackson, H.J. Baker and D.R. Hall, *CO<sub>2</sub> large-area discharge laser using an unstable-waveguide hybrid resonator*, Appl. Phys. Lett., 54, 1950, (1989).
78. H. Zhao, H.J. Baker and D.R. Hall, *Area scaling in slab rf excited carbon monoxide lasers*, Appl. Phys. Lett., 59, 1281, (1991).
79. C.J. Shackleton, H.J. Baker and D.R. Hall, *One-dimensional unstable resonators for waveguide slab lasers*, Conference on Lasers and Electro-Optics, paper CWG13, (1992).
80. K.M. Abramski, H.J. Baker, A.D. Colley and D.R. Hall, *Operation of slab waveguide lasers with a single high order waveguide stabilized by the Talbot effect*, Conference on Lasers and Electro-Optics, paper CFF2, (1992).



81. A.D. Colley, P.P. Vitruk, H.J. Baker and D.R. Hall, *Compact sealed slab waveguide CO<sub>2</sub> lasers at 1 kW*, Conference on Lasers and Electro-Optics, paper CCF 3, (1992).
82. G.A. Kerr, *Coherent addition of laser oscillators for use in gravitational wave antennas*, Appl. Phys. B, 49, 491, (1989).
83. J.S. Fender, *Phased array optical systems*, Infrared, Adaptive, and Synthetic Aperture Optical Systems, R.B. Johnson, W.L. Wolfe, J.S. Fender, editors, Proc. SPIE 643, 122, (1986).
84. J.P. Crancon and B. Lavarini, French Patents # 2092912, (1970), # 2108912, (1972).
85. G.I. Kozlov, V.A. Kuznetsov and V.A. Masyukov, *High-power multibeam cw CO<sub>2</sub> laser*, Sov. Tech. Phys. Lett., 3, 53, (1978).
86. V.V. Antyukhov, A.F. Glova, O.R. Karchurin and F.V. Lebedev, *Multibeam waveguide CO<sub>2</sub> laser excited by an alternating-current discharge*, Sov. J. Quantum Electron., 10, 240, (1980).
87. V.V. Antyukhov, A.I. Bondarenko, A.F. Glova, V.S. Golubev, O.R. Karchurin, L.L. Kolesov, E.A. Lebedev, F.V. Lebedev, Yu.F. Suslov, V.A. Timofeev, *High-power multibeam CO<sub>2</sub> laser excited by an ac discharge*, Sov. J. Quantum Electron., 11, 1363, (1981).
88. G.A. Abil'sitov, E.P. Velikhov, V.S. Golubev and F.V. Lebedev, *Promising systems and methods for pumping high-power technological CO<sub>2</sub> lasers (review)*, Sov. J. Quantum Electron., 11, 1535, (1981).
89. G.I. Kozlov and V.A. Kuznetsov, *Multibeam cw gas-discharge CO<sub>2</sub> laser Iglan-3*, Sov. J. Quantum Electron., 15, 362, (1985).
90. G.I. Kozlov and V.A. Kuznetsov, *Degradation of the active mixture and the feasibility of regenerating it in an Iglan-3 multibeam 5-kW gas-discharge CO<sub>2</sub> laser*, Sov. J. Quantum Electron., 18, 427, (1988).
91. G.I. Kozlov and V.A. Kuznetsov, *Multibeam industrial cw CO<sub>2</sub> laser with an output power of 10 kW*, Sov. J. Quantum Electron. 19, 878, (1989).
92. A. Glova, O. Karchurin, F. Lebedev, A. Napartovich, V. Pis'mennyi, *Modern multibeam CO<sub>2</sub> lasers and perspectives of their development*, High-Power Gas Lasers, P.V. Avizonis, C. Freed, J.J. Kim, F.K. Tittel, editors, Proc. SPIE 1225, 366, (1990).
93. S.Yu. Denisov, E.V. Zelenov, A.N. Safonov, V.M. Tarnsenko, D.Yu. Filimonov, E.A. Shcherbakova, *Characteristics of the formation of a radiation structure by focusing a*

- multichannel laser beam*, Sov. J. Quantum Electron., 21, 590, (1991).
94. L.A. Newman, R.A. Hart, J.T. Kennedy, A.J. Cantor and A.J. DeMaria, *High power coupled CO<sub>2</sub> waveguide laser array*, Appl. Phys. Lett., 48, 1701, (1986).
  95. C.G. Parazzoli and K. Chien, *Numerical analysis of a cw RF pumped CO<sub>2</sub> waveguide laser*, IEEE J. Quantum Electron., QE-22, 479, (1986).
  96. O.R. Karchurin, F.V. Lebedev and A.P. Napartovich, *Properties of an array of phase-locked CO<sub>2</sub> lasers*, Sov. J. Quantum Electron., 18, 1128, (1988).
  97. M. Sargent III, M.O. Scully and W.E. Lamb, Jr., *Laser Physics*, (Addison-Wesley, Reading, Mass, 1974).
  98. N.G. Basov, E.M. Belenov and V.S. Letokhov, *Diffraction synchronization of lasers*, Sov. Phys. Tech. Phys., 10, 845, (1965).
  99. C.L. Tang and H. Statz, *Phase-locking of laser oscillators by injected signal*, J. Appl. Phys., 38, 323, (1967).
  100. S.S. Townsend, *Modeling of supermodes in coupled unstable resonators*, Modeling and Simulation of Optoelectronic Systems, J.D. O'Keefe, editor, Proc. SPIE 624, 51, (1986).
  101. A.A. Golubentsev, V.V. Likhanski and A.P. Napartovich, *Theory of phase locking of an array of lasers*, Sov. Phys. JETP, 66, 676, (1987).
  102. M.B. Spencer and W.E. Lamb, Jr., *Theory of two coupled lasers*, Phys. Rev. A, 5, 893, (1972).
  103. H.L. Stover and W.H. Steier, *Locking of laser oscillators by light injection*, Appl. Phys. Lett., 8, 91, (1966).
  104. V.V. Likhanskii and A.P. Napartovich, *Radiation emitted by optically coupled lasers*, Sov. Phys. Usp., 33, 228, (1990).
  105. W.P. Latham, M.E. Rogers and G.E. Palma, *A review of laser device coupling techniques*, Optical Resonators, D.A. Holmes, editor, Proc. SPIE 1224, 184, (1990).
  106. W.R. Leeb, H.K. Philipp, A.L. Scholtz and E. Bonek, *Frequency synchronization and phase locking of CO<sub>2</sub> lasers*, Appl. Phys. Lett., 41, 592, (1982).
  107. C.P. Wang and P.L. Smith, *Phase control of HF chemical laser for coherent optical*

- recombination*, Appl. Opt., **18**, 1322, (1979).
108. C.P. Wang, *Master and slave oscillator array system for very large multiline lasers*, Appl. Opt., **17**, 83, (1978).
109. R. Protz, *Active optics for high power lasers*, Beam Diagnostics and Beam Handling Systems, A. Sona, editor, Proc. SPIE 1024, 138, (1989).
110. S.M. Rinaldi and J.H. Erkkila, *Semiclassical modeling and analysis of injected lasers*, Modeling and Simulation of Laser Systems, D.L. Bullock, editor, Proc. SPIE 1045, 104, (1989).
111. L.R. Brewer, *Highly coherent injection-locked laser diode arrays*, Appl. Opt., **30**, 317, (1991).
112. V.V. Burmistrov, A.F. Glova, V.V. Dylev and F.V. Lebedev, *High-power waveguide CO<sub>2</sub> amplifier with injection locking*, Sov. J. Quantum Electron., **21**, 19, (1991).
113. G.L. Bourdet, R.A. Muller, G.M. Mullot and J.Y. Vinet, *Performance and efficiency of an injection phase locked cw CO<sub>2</sub> waveguide laser*, New Developments and Applications in Gas Lasers, L.R. Carlson, editor, Proc. SPIE 737, 47, (1987).
114. J.M. Bernard, R.A. Chodzko and J.G. Coffey, *Master oscillator with power amplifiers: performance of a two-element cw HF phased laser array*, Appl. Opt., **28**, 4543, (1989).
115. R.A. Chodzko, J.M. Bernard and H. Mirels, *Coherent combination of multiline lasers*, Optical Resonators, D.A. Holmes, editor, Proc. SPIE 1224, 239, (1990).
116. Yu.A. Anan'ev, N.I. Grishmanova, L.V. Koval'chuk, N.A. Svetsitskaya, V.E. Sherstobitov, *Possibilities of control of radiation emitted by lasers with telescopic resonators*, Sov. J. Quantum Electron., **2**, 157, (1972).
117. G.L. Bourdet, R.A. Muller, G.M. Mullot and J.Y. Vinet, *CW injection phase locking in homogeneously broadened media II. Phase locking and tunability of CO<sub>2</sub> waveguide lasers*, Appl. Phys. B, **43**, 273, (1987).
118. J. Kendri and D. Treves, *Injection-locking optimization in unstable resonators*, Appl. Opt., **20**, 2108, (1981).
119. I.J. Bigio and M. Slatkine, *Injection-locking unstable resonator excimer lasers*, IEEE J. Quantum Electron., QE-19, 1426, (1983).
120. S.M. Rinaldi, *Semiclassical theory of injected lasers with arbitrary stable and unstable*

- resonators*, PhD thesis, Air Force Institute of Technology, Wright-Patterson AFB, (1987).
121. C.J. Buczek, R.J. Freiberg and M.L. Skolnick, *Laser injection locking*, Proc. IEEE, **61**, 1411, (1973).
  122. C.J. Buczek and R.J. Freiberg, *Hybrid injection locking of higher power CO<sub>2</sub> lasers*, IEEE J. Quantum Electron., QE-8, 641, (1972).
  123. I.J. Bigio and M. Slatkine, *Attainment of the theoretical minimum input power for injection locking of an unstable resonator KrF laser*, Opt. Lett., **6**, 336, (1981).
  124. A. Chandonnet and M. Piche, *Single-mode pulses from a high pressure CO<sub>2</sub> laser operated below emission threshold*, IEEE J. Quantum Electron., QE-27, 2226, (1991).
  125. W.W. Chow, *Phase locking of lasers by an injected signal*, Opt. Lett., **7**, 417, (1982).
  126. A.F. Glova, Yu.A. Dreizen, O.R. Karchurin, F.V. Lebedev and V.D. Pis'mennyi, *Phase locking of a two-dimensional array of CO<sub>2</sub> waveguide lasers*, Sov. Tech. Phys. Lett., **11**, 102, (1985).
  127. O.R. Karchurin, F.V. Lebedev, A.P. Napartovich, *Properties of an array of phase-locked CO<sub>2</sub> lasers*, Sov. J. Quantum Electron., **18**, 1128, (1988).
  128. A.A. Golubentsev and V.V. Likhanskii, *Characteristics of phase-locking an array of optically coupled lasers with a random scatter of eigenfrequencies*, Sov. J. Quantum Electron., **20**, 522, (1990).
  129. A.B. Vasil'ev, P.V. Korolenko and V.N. Tikhomirov, *Spatial mode locking under multibeam lasing conditions*, Sov. J. Quantum Electron., **20**, 1378, (1990).
  130. A.A. Golubentsev, O.R. Karchurin, F.V. Lebedev and A.P. Napartovich, *Use of a spatial filter for phase locking of a laser array*, Sov. J. Quantum Electron., **20**, 934, (1990).
  131. A.G. Aleksandrov, A.A. Angeluts, V.V. Vasil'tsov, E.V. Zelenov and E.A. Kurushin, *Phase locking of radiators in a multichannel laser by spatial filter*, Sov. J. Quantum Electron., **20**, 1370, (1990).
  132. F.X. D'Amato, E.T. Siebert, C. Roychoudhri, *Coherent operation of an array of diode lasers using a spatial filter in a Talbot cavity*, Appl. Phys. Lett., **55**, 816, (1989).
  133. W.B. Veldkamp, J.R. Leger and G.J. Swanson, *Coherent summation of laser beams using*

- binary phase gratings*, Opt. Lett., **11**, 303, (1986).
134. V.V. Antyukhov, A.F. Glova, O.R. Karchurin, F.V. Lebedev, V.V. Likhanski, A.P. Napartovich, V.D. Pis'mennyi, *Effective phase locking of an array of lasers*, JETP Lett., **44**, 78, (1986).
135. W.P. Brown, C.J. Gaeta, R.C. Lind and C.R. Giuliano, *Coherent coupling of cw laser oscillators using intercavity four-wave mixing*, IEEE J. Quantum Electron., QE-25, 607, (1989).
136. A.V. Bondarenko, A.F. Glova, F.V. Lebedev, V.V. Likhanski, A.P. Napartovich, V.D. Pis'mennyi, V.P. Yartsev, *Phase locking of waveguide CO<sub>2</sub> lasers as a result of a four-wave interaction of light beams in an absorbing liquid*, Sov. J. Quantum Electron., **18**, 563, (1988).
137. P.D. Hillman and M. Marciniak, *Phase locking laser diodes using photorefractive coupling*, J. Appl. Phys., **66**, 5731, (1989).
138. J. Feinberg and G.D. Bacher, *Phase-locking lasers with phase conjugation*, Appl. Phys. Lett., **48**, 570, (1986).
139. S. Sternklar, S. Weiss, M. Segrev and Fischer, *Beam coupling and locking of laser using photorefractive four-wave mixing*, Opt. Lett., **11**, 528, (1981).
140. A.A. Golubentsev, V.V. Likhanski, A.P. Napartovich, *Nonlinear tuning of a set of lasers*, Sov. J. Quantum Electron., **19**, 477, (1989).
141. H. Souma and C. Horie, *Theory of lasers with intracavity optical mixing*, J. Appl. Phys., **68**, 3114, (1990).
142. I.M. Bel'dyugin, D.D. Alimin and M.V. Zolotarev, *Phase locking of a laser array in the case of different types of multibeam intracavity interaction in nonlinear media*, Sov. J. Quantum Electron., **21**, 293, (1991).
143. V.Yu. Baranov, A.P. Dyad'kin, V.V. Likhanski, A.P. Napartovich, A.G. Sukharev and O.V. Shpilyun, *Frequency locking of two TEA CO<sub>2</sub> lasers utilizing a four-wave interaction in SF<sub>6</sub>*, Sov. J. Quantum Electron., **18**, 1462, (1988).
144. D.A. Rockwell and C.R. Giuliano, *Coherent coupling of laser gain media using phase conjugation*, Opt. Lett., **11**, 147, (1986).
145. K.M. Abramski, A.D. Colley, H.J. Baker and D.R. Hall, *Phase-locked CO<sub>2</sub> laser array using diagonal coupling of waveguide channels*, Appl. Phys. Lett., **60**, 530, (1992).

146. K.M. Abramski, A.D. Colley, H.J. Baker and D.R. Hall, *Offset frequency stabilization of RF excited waveguide CO<sub>2</sub> laser arrays*, IEEE J. Quantum Electron., **QE-26**, 711, (1990).
147. D.G. Youmans, *Phase locking of adjacent channel leaky waveguide CO<sub>2</sub> lasers*, Appl. Phys. Lett., **44**, 365, (1984).
148. A.D. Colley, K.M. Abramski, H.J. Baker and D.R. Hall, *Power and frequency balance in large waveguide CO<sub>2</sub> laser arrays*, Conference on Lasers and Electro-Optics, paper CTUB7, (1990).
149. G.E. Palma and W.J. Fader, *Coupled resonator beam combining*, Synthetic Aperture Systems, J.S. Fender, editor, Proc. SPIE 440, 153, (1984).
150. V.V. Lyubimov and L.V. Nosova, *Estimate of the influence of the difference between individual lasers on phase locking of a laser array*, Sov. J. Quantum Electron., **21**, 731, (1991).
151. W.W. Chow, *Frequency locking in weakly coupled lasers*, Opt. Lett., **10**, 442, (1985).
152. J.M. Bernard, R.A. Chodzko and H. Mirels, *Mutal coherence of two coupled multiline continuous-wave HF lasers*, Opt. Lett., **12**, 897, (1987).
153. J.M. Bernard, R.A. Chodzko and H. Mirels, *Coupled multiline cw HF lasers: experimental performance*, AIAA Journal, **26**, 1369, (1988).
154. V.V. Antyukhov, E.V. Dan'shchikov, N.N. Elkin, V.A. Korotkov, F.V. Lebedev, V.V. Likhanski, A.P. Napartovich, V.D. Pis'mennyi, V.E. Troshchiev, *Conditions for stable coherent operation of two CO<sub>2</sub> lasers with unstable resonators*, Sov. J. Quantum Electron., **19**, 1582, (1989).
155. M.P. Jelonek and W.B. Roh, *The effect of coupling strength on phase locking of Ar-ion lasers*, Optical Resonators, D.A. Holmes, editor, Proc. SPIE 1224, 226, (1990).
156. M.P. Jelonek and W.B. Roh, *Coupling strength dependence of phase locking of Ar-ion lasers*, Appl. Opt., **29**, 3160, (1990).
157. D.M. Walsh, *Longitudinal supermode analysis of two coupled CO<sub>2</sub> lasers*, Modeling and Simulation of Optoelectronic Systems, J.D. O'Keefe, editor, Proc. SPIE 642, 84, (1986).
158. J.A. Benda, W.J. Fader and G.E. Palma, *The influence of coupled resonator configurations on supermode discrimination*, Modeling and Simulation of Optoelectronic Systems, J.D. O'Keefe, editor, Proc. SPIE 642, 42, (1986).

159. H. Mirels, *Performance of two coupled lasers*, Appl. Opt., **25**, 2130, (1986).
160. N.N. Elkin, V.A. Korotkov, V.V. Likhanski, A.P. Napartovich and V.E. Troshchiev, *Stability of phase-locked lasing in a two coupled resonator system*, Seventh International Symposium on Gas Flow and Chemical Lasers, D. Schuocker, editor, Proc. SPIE 1031, 229, (1989).
161. G.E. Palma, J.A. Benda, S.S. Townsend, P.R. Cunningham and J. Forgham, *Coupled unstable resonators*, Optical Resonators, D.A. Holmes, editor, Proc. SPIE 1224, 202, (1990).
162. J.A. Benda, G.E. Palma and E.A. Sziklas, *Theory of ring lasers coupled using reverse waves*, Modeling and Simulation of Laser Systems, D.L. Bullock, editor, Proc. SPIE 1045, 116, (1989).
163. D.L. Bullock and J.S. Yun, *Fundamental beam quality considerations for modes of adjoint-coupled lasers*, Modeling and Simulation of Laser Systems, D.L. Bullock, editor, Proc. SPIE 1045, 129, (1989).
164. J.H. Erkkila, S. Shakir and V.A. Hedin, *Diffraction analysis of adjoint coupled unstable resonators*, Optical Resonators, D.A. Holmes, editor, Proc. SPIE 1224, 210, (1990).
165. E.F. Yelden, H.J.J. Seguin, C.E. Capjack and S.K. Nikumb, *Multichannel slab discharge for CO<sub>2</sub> laser excitation*, Appl. Phys. Lett., **58**, 693, (1991).
166. R. Malz and U. Haubenreisser, *Use of Zeolites for the stabilization of CO<sub>2</sub> partial pressure in sealed-off CO<sub>2</sub> waveguide lasers*, J. Phys. D: Appl. Phys., **24**, 1060, (1991).
167. W.J. Wiegand and W.L. Nighan, *Plasma chemistry of CO<sub>2</sub>-N<sub>2</sub>-He discharges*, Appl. Phys. Lett., **22**, 583, (1973).
168. W.L. Nighan and W.J. Wiegand, *Influence of negative-ion processes on steady-state properties and striations in molecular gas discharges*, Phys. Rev. A, **10**, 922, (1974).
169. S.R. Byron and H. Apter, *Model of gas composition and plasma properties in sealed cw CO<sub>2</sub> lasers*, J. Appl. Phys., **71**, 1976, (1992).
170. R.J. Carbone, *Long-term operation of a sealed CO<sub>2</sub> laser*, IEEE J. Quantum Electron., QE-3, 373, (1967).
171. P. Bletzinger, D.A. LaBorde, W.F. Bailey, W.H. Long, Jr., P.D. Tannen and A. Garscadden, *Influence of the contaminants on the CO<sub>2</sub> electric-discharge laser*, IEEE J. Quantum Electron., QE-11, 317, (1975).

172. A.L.S. Smith, H. Schields and A.E. Webb, *Cathode materials for sealed CO<sub>2</sub> waveguide lasers*, IEEE J. Quantum Electron., QE-19, 815, (1983).
173. R.L. Sinclair and J. Tulip, *Parameters affecting the performance of a rf excited CO<sub>2</sub> waveguide laser*, J. Appl. Phys., 56, 2497, (1984).
174. D. He and D.R. Hall, *Longitudinal voltage distribution in transverse rf discharge waveguide lasers*, J. Appl. Phys., 54, 4367, (1983).
175. G.A. Griffith, *Improved discharge uniformity for transverse radio frequency waveguide CO<sub>2</sub> lasers*, Advanced Laser Technology and Applications, L. Esterowitz, editor, Proc. SPIE 335, 69, (1982).
176. Y.M. Kim, C.E. Youn, J.W. Ra and Y.S. Kim, *Method for reducing the longitudinal voltage variation in transverse radio-frequency discharge waveguide lasers*, J. Appl. Phys., 67, 1127, (1990).
177. D.J. Griffiths, *Introduction to Electrodynamics*, (Prentice-Hall, Englewood Cliffs, New Jersey, 1981).
178. W.W. Rigrod, *Homogeneously broadened cw lasers with uniform distributed loss*, IEEE J. Quantum Electron., QE-14, 377, (1978).
179. D.C. Smith and J.H. McCoy, *Effects of diffusion on the saturation intensity of a CO<sub>2</sub> laser*, Appl. Phys. Lett., 15, 282, (1969).
180. R.L. Abrams and W.B. Bridges, *Characteristics of sealed-off waveguide CO<sub>2</sub> lasers*, IEEE J. Quantum Electron., QE-9, 940, (1973).
181. R.H. Bullis, W.L. Nighan, M.C. Fowler and W.J. Wiegand, *Physics of CO<sub>2</sub> electric discharge lasers*, AIAA Journal, 10, 407, (1972).
182. J. Tulip and H. Seguin, *Gain saturation measurements in the carbon dioxide laser using a Fresnel loss-plate technique*, Can. J. Phys., 48, 1086, (1970).
183. D. Fa, Z. Zhaoxin and H. Shunhua, *A new method of detecting small signal gain of CO<sub>2</sub> lasers*, Chinese Physics-Lasers, 14, 448, (1987).
184. B.S. Patel, *Determination of gain, saturation intensity, and internal losses of a laser using an intracavity rotatable reflector*, IEEE J. Quantum Electron., QE-9, 1150, (1973).
185. T. Kurosawa, *Estimation of small signal gain and saturation intensity in a waveguide CO<sub>2</sub> laser by a curve-fitting technique*, Jap. J. Appl. Phys., 26, 306, (1987).



186. V.A. Seguin, H.J.J. Seguin, C.E. Capjack and S.K. Nikumb, *Gain characteristics of a MAGPIE coaxial CO<sub>2</sub> laser system*, IEEE J. Quantum Electron., QE-23, 600, (1987).
187. S.K. Nikumb, H.J.J. Seguin, V.A. Seguin and H. Reshef, *Gain and saturation parameters of a multikilowatt PIE CO<sub>2</sub> laser*, J. Phys. E: Sci. Instrum., 20, 911, (1987).
188. R.L. Abrams, *Broadening coefficients for the P(20) CO<sub>2</sub> laser transition*, Appl. Phys. Lett., 10, 609, (1974).
189. A. Yariv, *Quantum Electronics*, 3rd edition, (John-Wiley and Sons, New York, 1989).
190. C.F. Hansen, *Combined Stark and Doppler line broadening*, J. Opt. Soc. Am., 54, 1198, (1964).
191. K.T.K. Cheng and L.W. Casperson, *Properties of a coaxial cw CO<sub>2</sub> laser*, Appl. Opt., 18, 2130, (1979).
192. J. Tulip, *Gain saturation of the carbon dioxide laser*, IEEE J. Quantum Electron., QE-6, 206, (1970).
193. V.A. Seguin, *A MAGPIE coaxial CO<sub>2</sub> laser system*, PhD thesis, University of Alberta, (1986).
194. M. Born and E. Wolf, *Principles of Optics*, 4th edition, (Pergamon, London, 1970).
195. P.E. Jackson, D.R. Hall, R.M. Jenkins and J.M. Vaughan, *Simultaneous measurements of gain and spontaneous emission noise in RF excited CO<sub>2</sub> amplifying media*, Active Infrared Systems and Technology, V.G. Roper, editor, Proc. SPIE 806, 46, (1987).
196. J.J. Lowke, A.V. Phelps and B.W. Irwin, *Predicted electron transport coefficients and operating characteristics of CO<sub>2</sub>-N<sub>2</sub>-He laser mixtures*, J. Appl. Phys., 44, 4664, (1973).
197. Y. Nachshon and U.P. Oppenheim, *Gain saturation in the CO<sub>2</sub> laser*, Appl. Opt., 12, 1934, (1973).
198. A.E. Siegman, *Unstable optical resonators for laser applications*, Proc. IEEE, 53, 277, (1965).
199. A.E. Siegman, *Unstable optical resonators*, Appl. Opt., 13, 353, (1974).
200. W.F. Krupke and W.R. Sooy, *Properties of an unstable confocal resonator CO<sub>2</sub> laser system*, IEEE J. Quantum Electron., QE-5, 575, (1969).

201. R.J. Freiberg, P.P. Chenausky and C.J. Buczek, *An experimental study of unstable confocal CO<sub>2</sub> resonators*, IEEE J. Quantum Electron., QE-8, 882, (1972).
202. S.R. Barone, *Optical resonators in the unstable region*, Appl. Opt., 6, 861, (1967).
203. M.A. Gorriz, *Wave propagation program - a necessary tool for unstable resonator design*, High Power CO<sub>2</sub> Laser Systems and Applications, A. Quenzer, editor, Proc. SPIE 1020, 49, (1989).
204. A.E. Siegman and H.Y. Miller, *Unstable optical resonator loss calculations using the Prony method*, Appl. Opt., 9, 2729, (1970).
205. D.B. Rensch and A.N. Chester, *Iterative diffraction calculation of transverse mode distribution in confocal unstable laser resonators*, Appl. Opt., 12, 997, (1973).
206. A.E. Bulyshev, G.A. Vedernikov and N.G. Preobrazhenskii, *Calculation of laser resonator characteristics*, Sov. J. Quantum Electron., 10, 623, (1980).
207. A.E. Siegman, *A canonical formulation for analyzing multielement unstable resonators*, IEEE J. Quantum Electron., QE-12, 35, (1976).
208. A.E. Siegman, *Stabilizing output with unstable resonators*, Laser Focus, 7, 42, (1971).
209. A.E. Siegman, *New developments in laser resonators*, Optical Resonators, D.A. Holmes, editor, Proc. SPIE 1224, 2, (1990).
210. E.A. Phillips, J.P. Reilly and D.B. Northam, *Off-axis unstable laser resonator: operation*, Appl. Opt., 15, 2159, (1976).
211. Yu.A. Anan'ev, *Unstable resonators and their applications (review)*, Sov. J. Quantum Electron., 1, 565, (1972).
212. Yu.A. Anan'ev, *Selection of the resonator type*, Sov. J. Quantum Electron., 19, 1357, (1989).
213. P.R. Cunningham and S.S. Townsend, *Mode properties and characteristics of negative-branch unstable ring resonators*, Opt. Eng., 30, 1553, (1991).
214. R.J. Tansey, V. Gamiz, R. Mickish, D.A. Holmes, D. Kohler, J. Martin and E. Pape, *Higher order azimuthal mode unstable resonator (HAMUR)*, Optical Resonators, D.A. Holmes, editor, Proc. SPIE 1224, 371, (1990).

215. A.G. Fox and T. Li, *Resonant modes in a maser interferometer*, Bell Syst. Tech. J., **40**, 453, (1961).
216. K.E. Oughstun, *Unstable resonator modes*, Progress in Optics Vol. XXIV, E. Wolf, editor, (Elsevier Science Publ., Amsterdam, 1987).
217. A.E. Siegman, *Lasers*, (University Science Books, Mill Valley, USA, 1986).
218. D.P. Chernin, *Optical extraction efficiency in lasers with high Fresnel number confocal unstable resonators*, Appl. Opt., **18**, 3562, (1979).
219. A.K. Nath, H.J.J. Seguin and V.A. Seguin, *Optimization studies of a multikilowatt PIE CO<sub>2</sub> laser*, IEEE J. Quantum Electron., QE-22, 268, (1986).
220. Z. Cheng, H.J.J Seguin, S.K. Nikumb, V.A. Seguin and H. Reshef, *Annular-coupled concave-convex stable resonator for large-volume high-quality energy extraction*, Appl. Opt., **27**, 836, (1988).
221. G.A. Heckman and M. Piche, *Reshaping of annular laser beams with conical reflectors*, Beam Diagnostics and Beam Handling Systems, A. Sona, editor, Proc. SPIE 1024, 159, (1989).
222. I.J. Spalding, A.C. Selden, M. Hill, J.H.P.C. Megaw and B.A. Ward, *High power CO<sub>2</sub> lasers*, Culham Laboratory Internal Report, CLM-P847, (1988).
223. J.P. Reilly, *Unstable Optical Resonators*, United States Patent #3,873,942, (1975).
224. S.W. Townsend and J.P. Reilly, *Unobscured unstable resonator designs for large bore lasers*, Mirrors and Windows for High Power/High Energy Laser Systems, C.A. Klein, editor, Proc. SPIE 1047, 184, (1989).
225. T.R. Ferguson and M.E. Smithers, *Toric unstable resonators*, Appl. Opt., **23**, 2122, (1984).
226. L. Levi, *Applied Optics*, (Wiley, New York, 1968).
227. The specification sheet supplied with the lens from Laser Power Optics states the absorption as  $\leq 0.25\%$ .
228. C.V. Sellathamby, H.J.J. Seguin and S.K. Nikumb, *Performance characteristics of a high power CO<sub>2</sub> laser with computer vision and power control*, Appl. Opt., **29**, 4499, (1990).

229. C.V. Sellathamby, H.J.J. Seguin and S.K. Nikumb, *Mode stabilization of a high power laser via computer vision*, Opt. Comm., 78, 47, (1990).
230. G.C. Lim and W.M. Steen, *Measurement of the temporal and spatial power distribution of a high-power CO<sub>2</sub> laser beam*, Opt. Laser Technol., 14, 149, (1982).
231. G.C. Lim and W.M. Steen, *Instrument for instantaneous in situ analysis of the mode structure of a high-power laser beam*, J. Phys. E: Sci. Instrum., 17, 999, (1984).
232. M. Welch, *Concepts of polarization physics*, Lasers and Appl., 5, 67, (1986).
233. V.M. Weerasinghe, J. Gabzdyl and R.D. Hibberd, *Properties of a laser beam generated from an axicon resonator*, Opt. Laser Technol., 21, 389, (1989).
234. E. Stuart and H.N. Rutt, *Selection criteria for polarizing mirrors for use in high-power CO<sub>2</sub> lasers*, J. Phys. D: Appl. Phys., 22, 901, (1989).
235. P.W. Milonni and J.H. Eberly, *Lasers*, (Wiley, New York, 1988).
236. Y.J. Kaufman and U.P. Oppenheim, *State equations of high gain lasers and determination of laser parameters*, Appl. Opt., 18, 1071, (1979).
237. A. Hongo, M. Miyagi, Y. Watanabe and S. Nishida, *Thin film-coated waveguide CO<sub>2</sub> laser*, IEEE J. Quantum Electron., QE-22, 1604, (1986).
238. E. Hecht and A. Zajac, *Optics*, (Addison-Wesley, Reading, MA, USA, 1979).
239. Yu.A. Anan'ev and V.E. Sherstobitov, *Influence of the edge effects on the properties of unstable resonators*, Sov. J. Quantum Electron., 1, 263, (1971).
240. N. Hodgson and H. Weber, *Unstable resonators with excited converging wave*, IEEE J. Quantum Electron., QE-26, 731, (1990).
241. G.J. Dezenberg, *Stable lasers in dynamic environments*, Laser Radar II, R.J. Becherer, R.C. Harney, editors, Proc. SPIE 783, 2, (1987).
242. G.L. Herrit and H.E. Reedy, *Advanced figure of merit evaluation for CO<sub>2</sub> laser optics using finite element analysis*, Mirrors and Windows for High Power/High Energy Laser Systems, C.A. Klein, editor, Proc. SPIE 1047, 33, (1989).
243. H.E. Hagemeyer and S.R. Robinson, *Field properties of multiple coherently combined lasers*, Appl. Opt., 18, 270, (1979).

244. J.G. Coffey, J.M. Bernard, R.A. Chodzko, E.B. Turner, R.W.F. Gross and W.R. Warren, *Experiments with active phase matching of parallel-amplified multiline HF laser beams by a phase-locked Mach-Zehnder interferometer*, Appl. Opt., **22**, 142, (1983).
245. M. Francon, *Optical Interferometry*, (Academic Press, New York, 1966).
246. X.X. Shan, R. Fedosejevs, B. Harwood, C. Yamanaka, D.C. Thompson and A.A. Offenberger, *Injection locking of a KrF laser using a frequency-doubled argon-ion laser pulse*, IEEE J. Quantum Electron., QE-26, 169, (1990).
247. K.C. Sun, *Geometrical analysis of reverse mode in decentered annular ring resonators (DARR)*, Optical Resonators, D.A. Holmes, editor, Proc. SPIE 1224, 338, (1990).
248. R.A. Chodzko and A.N. Chester, *Optical aspects of chemical lasers*, Handbook of Chemical Lasers, R.W.F. Gross and J.F. Bott, editors, (Wiley, New York, 1976).
249. D.S. Gnanamuthu, *Laser surface treatment*, Source Book on Applications of the Laser in Metalworking, (American Society of Metals, Metals Park, Ohio, USA, 1981).
250. A. Sona, *Industrial applications of lasers overview*, Applied Laser Tooling, O.D.D. Soares and M. Perez-Amor, editors, (Martinus Nijhoff, Dordrecht, Netherlands, 1987).
251. R.C. Crater and P.J. Oakley, *Process and physical aspects of continuous wave laser processing*, Applied Laser Tooling, O.D.D. Soares and M. Perez-Amor, editors, (Martinus Nijhoff, Dordrecht, Netherlands, 1987).
252. W.M. Steen, *Surface engineering with lasers*, Applied Laser Tooling, O.D.D. Soares and M. Perez-Amor, editors, (Martinus Nijhoff, Dordrecht, Netherlands, 1987).
253. E.F. Yelden, H.J.J. Seguin, C.E. Capjack and S.K. Nikumb, *A multi-channel slot discharge CO<sub>2</sub> laser employing a toric unstable resonator*, Opt. Comm., **82**, 503, (1991).
254. E.F. Yelden, H.J.J. Seguin, C.E. Capjack, S.K. Nikumb and H. Reshef, *Toric unstable CO<sub>2</sub> laser resonator - an experimental study*, Appl. Opt., **31**, 1965, (1992).
255. S. Yatsiv, A. Gabay and M. Brestel, *A CO<sub>2</sub> laser mounted on a robot for dynamic cutting manipulations*, CO<sub>2</sub> Lasers and Applications II, H. Opower, editor, Proc. SPIE 1276, 142, (1990).
256. Yu.A. Anan'ev, G.N. Vinkurov, L.V. Koval'chuk, N.A. Svetsitskaya and V.E. Sherstobitov, *Telescopic-resonator lasers*, Sov. Phys. JETP, **31**, 420, (1970).
257. Yu.A. Anan'ev, N.I. Grishmanova, I.M. Petrova and N.A. Svetsitskaya, *Internal*

- reflecting surfaces in unstable resonators*, Sov. J. Quantum Electron., 5, 1060, (1976).
258. Yu.A. Anan'ev, D.A. Goryachkin, N.A. Svetsitskaya and I.M. Petrova, *Investigation of the properties of a laser with an unstable resonator and additional feedback*, Sov. J. Quantum Electron., 9, 1043, (1979).
259. P.B. Corkum and H.A. Baldis, *Extra-cavity feedback into unstable resonators*, Appl. Opt., 18, 1346, (1979).
260. A. Fogelman, O. Pade and Y. Nachshon, *A new type of unstable resonator*, Optical Resonators, D.A. Holmes, editor, Proc. SPIE 1224, 289, (1990).
261. S.K. Nikumb, personal communication.
262. R.J. Freiberg, D.W. Fradin and P.P. Chenausky, *Split-mode unstable resonator*, Appl. Opt., 16, 1192, (1977).